UCLA
UCLA Electronic Theses and Dissertations

Title
Microfluidic Platforms for Digitalized Biological Sample Processing

Permalink
https://escholarship.org/uc/item/59t8f6pn

Author
Wang, Yilian

Publication Date
2021

Peer reviewed|Thesis/dissertation

eScholarship.org Powered by the California Digital Library
University of California

UNIVERSITY OF CALIFORNIA

Los Angeles

Microfluidic Platforms for Digitalized Biological Sample Processing

A dissertation submitted in partial satisfaction of the

requirements for the degree Doctor of Philosophy in

Bioengineering

by

Yilian Wang

2021

© Copyright by

Yilian Wang

2021

ABSTRACT OF THE DISSERTATION

Microfluidic Platforms for Digitalized Biological Sample Processing

by

Yilian Wang

Doctor of Philosophy in Bioengineering

University of California, Los Angeles, 2021

Professor Dino Di Carlo, Chair

Analysis of biomarkers, biomolecular indicators of medical conditions, is fundamental to the diagnosis and the medicinal research of various diseases and other human physiological conditions. These biomarkers are usually found in complex biological samples and almost always require multi-step sample processing before the key information of the relevant biomarkers could be extracted for analysis. The sample processing procedures are associated with the performance metrics of the assay, such as the sensitivity and accuracy of the result, and therefore is critical to the reliability of diagnosis result or the goal of the research missions. Furthermore, such sample processing procedures often start with a limited volume available from subject and involve a series of technical steps tailored towards the target biomarkers resulting in process complexity.

The application of microfluidic platform technologies to biological sample processing and corresponding assays demonstrated great potential in advancing biomarker analysis, both in simplifying assay processes by means such as miniaturization, automation, and cost reduction; and in improving assay performance on metrics such as sensitivity, assay time, throughput, etc.

This work explores microfluidic solutions to improving sample processing procedures, especially by means of process automation; and enhancing the sensitivity metrics of assay performances, targeting the analysis of single entities. The first two chapters covers the development of digitalized affinity assays for single molecule detection, where we achieved counting of single enzyme reactions using a novel lab-on-a-particle assay mechanism. We demonstrated digital counting of β-galactosidase enzyme at a femtomolar detection limit with a dynamic range of 3 orders of magnitude using standard benchtop equipment and experiment techniques. The third chapter presents an innovative ferrobot platform to address process automation for sample processing. This electromagnetic platform is capable of performing massively parallelized and sequential fluidic operations cross-collaboratively to complete pipelined bioassays with high efficiency and flexibility. In the fourth and final chapter we established a multiferroic system deployed for time-lapse single-cell functional profiling, featuring both single entity analysis capacity and an automation potential.

The dissertation of Yilian Wang is approved.

Manish J. Butte

Robert N. Candler

Sam Emaminejad

Dino Di Carlo, Committee Chair

University of California, Los Angeles

2021

DEDICATION

To my parents who told me the world is big, the numerous books that showed me exactly how, and my friends who navigated this world with me.

TABLE OF CONTENTS

LIST OF FIGURES

ACKNOWLEDGEMENTS

Chapter 1 is adapted from a manuscript in progress "Digital ELISA: Technical Platforms and Strategies". Y.W., V.S., and D.D. drafted the manuscript.

Chapter 2 is adapted from a manuscript in review "Counting of Enzymatically Amplified Affinity Reactions in Hydrogel Particle-Templated Drops", Lab on a Chip (2021). Y.W., V.S., and D.D. conceived the idea and contributed to the design of experiments. Y.W., V.S., A.L., E.P., and B.C. performed the experiments and contributed to data analysis. Y.W., V.S., and D.D. drafted the manuscript, and all the authors provided feedback. We acknowledge the UCLA Nanofabrication Laboratory for access to microfabrication facilities and the UCLA Eli and Edythe Broad Center of Regenerative Medicine and Stem Cell Research.

Chapter 3 is adapted from "A ferrobotic system for automated microfluidic logistics", Science Robotics (2020), doi: 10.1126/scirobotics.aba4411. S.E., D.D., W.Y., H.L., and Y.W. conceived the general ferrobot idea and contributed to the design of experiments. W.Y., H.L., X.H., N.C., K.S., and J.T. conducted the device fabrication and characterization. Y.W. designed and validated the quantitative assay framework. W.Y., H.L., and N.C. designed the PCB circuit. W.Y., H.L., Y.W., and D.L. performed bioassays and fluorescent imaging. Y.W. developed the imaging algorithm. W.Y., H.L., Y.W., X.H., N.C., K.S., D.L., and B.C. contributed to analytical tools and data analysis. S.E., D.D., W.Y., H.L., Y.W., and C.Y. drafted the manuscript, and all the authors provided feedback. We thank the UCLA Nanoelectronics Research Facility (NRF) for providing access to device fabrication equipment and J. Shao at UCLA Department of Radiological Science for supplying ferumoxytol materials.

Chapter 4 is adapted from "Single-Domain Multiferroic Array-Addressable Terfenol-D (SMArT) Micromagnets for Programmable Single-Cell Capture and Release", Advanced Materials (2021), doi: 10.1002/adma.202006651. M.K.P and Z.X. fabricated the multiferroic components. Z.X., M.G., and R.V.C. performed characterizations of the multiferroic components. R.K. devised the microfluidic setup and performed characterizations, and M.B. developed the imaging analysis framework. Y.W. developed the time-dependent single cell assay. R.K., M.X., M.K.P., Y.W., R.C., and D.D. drafted the manuscript, and all the authors provided feedback. We acknowledge the use of fabrication facility at the Integrated Systems Nanofabrication Cleanroom at the California Nanosystems Institute, the UCLA/CFAR Virology Core Laboratory for providing human blood, and R. Dimatteo for separating human primary T cells from whole blood.

This work was supported by the National Science Foundation Engineering Research Center for Translational Applications of Nanoscale Multiferroic Systems (TANMS) and Precise Advanced Technologies and Health Systems for Underserved Populations (PATHS-UP).

Throughout the completion of my PhD I have received a great deal of support and assistance. A great many thanks go to my supervisor, Professor Dino Di Carlo, whose expertise was invaluable in the formulating of project designs and methodology. Additional thanks go to my collaborators at NSF-ERC TANMS and Dr. Emaminejad lab at UCLA. I would also like acknowledge my colleagues in Di Carlo lab for their support, advice and friendship throughout my PhD.

VITA

EDUCATION

B.S. in Pharmaceutical Sciences (2016), Peking University, Beijing, China

B.S. in Psychology (2016), Peking University, Beijing, China

RESEARCH APPOINTMENTS

Graduate Student Researcher (2017-2021), University of California, Los Angeles

Professor Dino Di Carlo, Department of Bioengineering

Undergraduate Research Intern (2015-2016), Chinese Academy of Science

Professor Xingyu Jiang, National Center for Nanoscience and Technology

Undergraduate Researcher (2015), University of Toronto

Professor Shirley X.Y. Wu, Leslie Dan Faculty of Pharmacy

Undergraduate Research Assistant (2014-2016), Peking University

Professor Xinru Li, Department of Pharmaceutics

PUBLICATIONS

- *(In Progress)* Wang, Y., Shah, V., Di Carlo, D., 2021. Digital ELISA: Technical Platforms and Strategies
- *(In Review)* Wang, Y.*, Shah, V.*, Lu, A., Pachler, E., Cheng, B., Di Carlo, D., 2021. Counting of Enzymatically Amplified Affinity Reactions in Hydrogel Particle-Templated Drops. *Lab on a Chip.*

- Yu, W.*, Lin, H.*, Wang, Y.*, He, X., Chen, N., Sun, K., Lo, D., Cheng, B., Yeung, C., Tan, J. and Di Carlo, D., 2020. A ferrobotic system for automated microfluidic logistics. *Science Robotics*, 5(39).
- Khojah, R., Xiao, Z., Panduranga, M.K., Bogumil, M., Wang, Y., Goiriena-Goikoetxea, M., Chopdekar, R.V., Bokor, J., Carman, G.P., Candler, R.N. and Di Carlo, D., 2021. Single-Domain Multiferroic Array-Addressable Terfenol-D (SMArT) Micromagnets for Programmable Single-Cell Capture and Release. *Advanced Materials,* p.2006651.
- Xiao, Z., Khojah, R., Chooljian, M., Conte, R.L., Schneider, J.D., Fitzell, K., Chopdekar, R.V., Wang, Y., Scholl, A., Chang, J. and Carman, G.P., 2018. Cytocompatible magnetostrictive microstructures for nano-and microparticle manipulation on linear strain response piezoelectrics. *Multifunctional Materials*, 1(1), p.014004.
- Zhang, L., Sun, J., Wang, Y., Wang, J., Shi, X. and Hu, G., 2016. Nonspecific Organelle-Targeting Strategy with Core-Shell Nanoparticles of Varied Lipid Components/Ratios. *Analytical chemistry*, 88(14), pp.7344-7351.

Introduction

Analysis of biomarkers, biomolecular indicators of medical conditions, is fundamental to the diagnosis and the medicinal research of various diseases and other human physiological conditions. These biomarkers are frequently found in complex biological samples and almost always require multi-step sample processing before the key information on relevant biomarkers could be extracted for analysis.[1] The sample processing procedures are directly associated with the performance metrics of the assay, such as the sensitivity and accuracy of the result,[2-4] and therefore is critical to the reliability of diagnosis result or the goal of the research missions. Furthermore, such sample processing procedures often start with a limited volume available from subject and involve a series of technical steps tailored towards the target biomarkers resulting in process complexity.

Microfluidic technologies demonstrated great potential in advancing biomarker analysis, both in simplifying assay processes by means such as miniaturization[5,6], automation[7,8], and cost reduction[9-12]; and in improving assay performance on metrics such as sensitivity[13-15], assay time[16,17], throughput[18-21], etc. This work explores microfluidic solutions to improving sample processing procedures, especially by means of process automation; and enhancing the sensitivity metrics of assay performances, targeting the analysis of single entities.

-

Digital bioassays, in contrast to conventional analogue bioassays that are commonly performed in a single reactor, partition a reaction into a large number of microreactors, allowing a binary loading

of most compartments with 0 or 1 target molecule, reaching the ultimate sensitivity of single molecuels[22] and femtomolar to attomolar[23,24] limit of detection for protein biomarkers. While the enrichment effect of the compartmentalization of the reaction solution is immediate and general for all types of bioassays, digital bioassays are compatible with existing classical techniques widely used in normal biological, chemical, or clinical laboratories. Specifically, digital enzyme linked immunosorbent assays (ELISA) allow measurement of individual protein biomarkers, leveraging sub-nanoliter compartmentalization and signal amplification.[25] However, these technologies require tailored and often expensive microwell devices or microfluidic droplet generators for compartmentalization, and custom optical analysis systems to characterize low levels of fluorescence. The need for specialized and relatively costly equipment (e.g. Quanterix Simoa system[26]) has impeded the adoption of digital ELISA technologies for biomarker discovery or clinical diagnosis.

The first two chapters here covers the development of digitalized affinity assays for single molecule detection, where we achieved counting of single enzyme reactions using a novel lab-on-a-particle assay mechanism. Counting of numerous compartmentalized enzymatic reactions underlies quantitative and high sensitivity immunodiagnostic assays. However, digital enzyme-linked immunosorbent assays (ELISA) require specialized instruments which have slowed adoption in research and clinical labs. We present a lab-on-a-particle solution to digital counting of thousands of single enzymatic reactions. Hydrogel particles are used to bind enzymes and template the formation of droplets that compartmentalize reactions with simple pipetting steps. These hydrogel particles can be made at a high throughput, stored, and used during the assay to create ~500,000 compartments within 2 minutes. These particles can also be dried and rehydrated

with sample, amplifying the sensitivity of the assay by driving affinity interactions on the hydrogel surface. We demonstrate digital counting of β-galactosidase enzyme at a femtomolar detection limit with a dynamic range of 3 orders of magnitude using standard benchtop equipment and experiment techniques. This approach can faciliate the development of digital ELISAs with reduced need for specialized microfluidic devices, instruments, or imaging systems.

-

Digital microfluidic platforms have demonstrated great advantages in biological assay automation[27], facilitating versatile and multi-step bioanalytical operations suitable for various applications such as point-of-care diagnosis. Previously demonstrated digital microfluidic platforms have mostly relied on electrowetting-on-dielectric (EWOD) techniques. However, EWOD approaches require complex device fabrication, high excitation voltage (~20-200 V), and can suffer from electrode contamination and limited durability, which altogether restrict EWOD from achieving the envisioned applications[28]. Alternatively, magnetic droplet actuation techniques have been demonstrated using (1) motorized/manually-controlled magnets[29], which is not scalable, or (2) electromagnetic (EM) induction[30], which inherently renders weak actuation forces, limiting the ability to control small ferrofluid drops.

The third chapter presents an innovative ferrobot platform to address process automation for sample processing. Automated technologies that can perform massively parallelized and sequential fluidic operations at small length scales can resolve major bottlenecks encountered in various fields, including medical diagnostics, -omics, drug development, and chemical/material synthesis. Inspired by the transformational impact of automated guided vehicle systems on

manufacturing, warehousing, and distribution industries, we devised a ferrobotic system that uses a network of individually addressable robots, each performing designated micro-/nanofluid manipulation-based tasks in cooperation with other robots toward a shared objective. The underlying robotic mechanism facilitating fluidic operations was realized by addressable electromagnetic actuation of miniature mobile magnets that exert localized magnetic body forces on aqueous droplets filled with biocompatible magnetic nanoparticles. The contactless and high-strength nature of the actuation mechanism inherently renders it rapid (~10 centimeters/second), repeatable (>10,000 cycles), and robust (>24 hours). The robustness and individual addressability of ferrobots provide a foundation for the deployment of a network of ferrobots to carry out cross-collaborative logistics efficiently. These traits, together with the reconfigurability of the system, were exploited to devise and integrate passive/active advanced functional components (e.g., droplet dispensing, generation, filtering, and merging), enabling versatile system-level functionalities. By applying this ferrobotic system within the framework of a microfluidic architecture, the ferrobots were tasked to work cross-collaboratively toward the quantification of active matrix metallopeptidases (a biomarker for cancer malignancy and inflammation) in human plasma, where various functionalities converged to achieve a fully automated assay.

-

Sorting engineered cells with unique properties or functions from a larger population represents the future for personalized individual cell therapies[31,32]. Antibody functionalized paramagnetic particles can specifically bind to cells that present matching membrane protein[33]. This enables selection of desired subpopulations of cells based on surface biomarkers in therapy production[34].

However, the expression of surface biomarkers does not always represent the phenotypic properties important to cell therapies. There are a wide range of medically relevant phenotypic properties of cells, such the kinetics of cell receptor expression[35], cytokine secretion[36], cell-cell interactions[37] and phosphorylation state of signaling pathways[38], and effective ways to characterize them on a single-cell level is in demand. One potential solution is to create precise and programmable micromagnetic fields scaled to the size of single cells (10-20 μm) for localized magnetic cell manipulation and selection based on complex phenotypes.

In the fourth and final chapter we established a multiferroic system deployed for time-lapse single-cell functional profiling, featuring both single entity analysis capacity and an automation potential. We investigate polycrystalline Ni and FeGa magnetostrictive microstructures on pre-poled (011)-cut single crystal $[Pb(Mg_{1/3}Nb_{2/3})O_3]_{1-x}$-$[PbTiO_3]_x$ (PMN-PT, $x \approx 0.31$) with linear strain profile versus applied electric field. With an applied electric field, the magnetic domains are actuated, inducing the motion of the coupled particles with sub-micrometer precision. On this platform we demonstrated the cytocompatibility of the platform for live cell sorting applications and carried out time-dependent measurement of cytokine secretion from magnetically captured single human primary T-cells, showing the promise of using energy-efficient electric-field-controlled magnetostrictive micro- and nanostructures for single cell manipulation.

References

1. Sonker, Mukul, Vishal Sahore, and Adam T. Woolley. "Recent advances in microfluidic sample preparation and separation techniques for molecular biomarker analysis: A critical review." *Analytica chimica acta* 986 (2017): 1-11.
2. US Department of Health and Human Services. "Bioanalytical method validation, guidance for industry." *http://www. fda. gov./cder/guidance/4252fnl. htm* (2001).
3. Wenzel, Katrin, et al. "Performance and in-house validation of a bioassay for the determination of beta1-autoantibodies found in patients with cardiomyopathy." *Heliyon* 3.7 (2017): e00362.
4. Grailer, Jamison, et al. "Considerations in Developing Reporter Gene Bioassays for Biologics." *Immuno-Oncology*. Humana, New York, NY, 2020. 131-156.
5. Ehrnström, Rolf. "Profile: Miniaturization and integration: challenges and breakthroughs in microfluidics." *Lab on a Chip* 2.2 (2002): 26N-30N.
6. Vyawahare, Saurabh, Andrew D. Griffiths, and Christoph A. Merten. "Miniaturization and parallelization of biological and chemical assays in microfluidic devices." *Chemistry & biology* 17.10 (2010): 1052-1065.
7. Melin, Jessica, and Stephen R. Quake. "Microfluidic large-scale integration: the evolution of design rules for biological automation." *Annu. Rev. Biophys. Biomol. Struct.* 36 (2007): 213-231.
8. Su, Fei, Krishnendu Chakrabarty, and Richard B. Fair. "Microfluidics-based biochips: technology issues, implementation platforms, and design-automation challenges." *IEEE transactions on computer-aided design of integrated circuits and systems* 25.2 (2006): 211-223.

9. Tsao, Chia-Wen. "Polymer microfluidics: Simple, low-cost fabrication process bridging academic lab research to commercialized production." *Micromachines* 7.12 (2016): 225.
10. Tomazelli Coltro, Wendell Karlos, et al. "Recent advances in low‐cost microfluidic platforms for diagnostic applications." *Electrophoresis* 35.16 (2014): 2309-2324.
11. Abdelgawad, Mohamed, and Aaron R. Wheeler. "Low-cost, rapid-prototyping of digital microfluidics devices." *Microfluidics and nanofluidics* 4.4 (2008): 349-355.
12. Dungchai, Wijitar, Orawon Chailapakul, and Charles S. Henry. "A low-cost, simple, and rapid fabrication method for paper-based microfluidics using wax screen-printing." *Analyst* 136.1 (2011): 77-82.
13. Kaushik, Aniruddha M., Kuangwen Hsieh, and Tza‐Huei Wang. "Droplet microfluidics for high‐sensitivity and high‐throughput detection and screening of disease biomarkers." *Wiley Interdisciplinary Reviews: Nanomedicine and Nanobiotechnology* 10.6 (2018): e1522.
14. Sadeghi, Saman, et al. "On chip droplet characterization: a practical, high-sensitivity measurement of droplet impedance in digital microfluidics." *Analytical chemistry* 84.4 (2012): 1915-1923.
15. Zimmermann, Martin, et al. "Modeling and optimization of high-sensitivity, low-volume microfluidic-based surface immunoassays." *Biomedical microdevices* 7.2 (2005): 99-110.
16. Aroonnual, Amornrat, et al. "Microfluidics: innovative approaches for rapid diagnosis of antibiotic-resistant bacteria." *Essays in biochemistry* 61.1 (2017): 91-101.
17. Burklund, Alison, et al. "Advances in diagnostic microfluidics." *Advances in clinical chemistry* 95 (2020): 1-72.

18. Abate, Adam R., et al. "High-throughput injection with microfluidics using picoinjectors." *Proceedings of the National Academy of Sciences* 107.45 (2010): 19163-19166.
19. Brouzes, Eric, et al. "Droplet microfluidic technology for single-cell high-throughput screening." *Proceedings of the National Academy of Sciences* 106.34 (2009): 14195-14200.
20. Guo, Mira T., et al. "Droplet microfluidics for high-throughput biological assays." *Lab on a Chip* 12.12 (2012): 2146-2155.
21. Chabert, Max, and Jean-Louis Viovy. "Microfluidic high-throughput encapsulation and hydrodynamic self-sorting of single cells." *Proceedings of the National Academy of Sciences* 105.9 (2008): 3191-3196.
22. Basu, Amar S. "Digital assays part I: partitioning statistics and digital PCR." *SLAS TECHNOLOGY: Translating Life Sciences Innovation* 22.4 (2017): 369-386.
23. Kan, Cheuk W., et al. "Digital enzyme-linked immunosorbent assays with sub-attomolar detection limits based on low numbers of capture beads combined with high efficiency bead analysis." *Lab on a Chip* 20.12 (2020): 2122-2135.
24. Ono, Takao, Takanori Ichiki, and Hiroyuki Noji. "Digital enzyme assay using attoliter droplet array." *Analyst* 143.20 (2018): 4923-4929.
25. Zhang, Yi, and Hiroyuki Noji. "Digital bioassays: theory, applications, and perspectives." *Analytical chemistry* 89.1 (2017): 92-101.
26. Wilson, David H., et al. "The Simoa HD-1 analyzer: a novel fully automated digital immunoassay analyzer with single-molecule sensitivity and multiplexing." *Journal of laboratory automation* 21.4 (2016): 533-547.

27. Samiei, Ehsan, Maryam Tabrizian, and Mina Hoorfar. "A review of digital microfluidics as portable platforms for lab-on a-chip applications." *Lab on a Chip* 16.13 (2016): 2376-2396.

28. Zhang, Yi, and Nam-Trung Nguyen. "Magnetic digital microfluidics–a review." *Lab on a Chip* 17.6 (2017): 994-1008.

29. Pipper, Juergen, et al. "Clockwork PCR including sample preparation." *Angewandte Chemie* 120.21 (2008): 3964-3968.

30. Lehmann, Ulrike, et al. "Droplet-based DNA purification in a magnetic lab-on-a-chip." *Angewandte Chemie International Edition* 45.19 (2006): 3062-3067.

31. Fischbach, Michael A., Jeffrey A. Bluestone, and Wendell A. Lim. "Cell-based therapeutics: the next pillar of medicine." *Science translational medicine* 5, no. 179 (2013): 179ps7-179ps7.

32. Fesnak, Andrew D., Carl H. June, and Bruce L. Levine. "Engineered T cells: the promise and challenges of cancer immunotherapy." *Nature Reviews Cancer* 16, no. 9 (2016): 566.

33. Miltenyi, S., Müller, W., Weichel, W., & Radbruch, A. (1990). High gradient magnetic cell separation with MACS. *Cytometry: The Journal of the International Society for Analytical Cytology,* 11(2), 231-238.

34. Talasaz, A.H., Powell, A.A., Huber, D.E., Berbee, J.G., Roh, K.H., Yu, W., Xiao, W., Davis, M.M., Pease, R.F., Mindrinos, M.N. and Jeffrey, S.S., 2009. Isolating highly enriched populations of circulating epithelial cells and other rare cells from blood using a magnetic sweeper device. *Proceedings of the National Academy of Sciences*, pp.pnas-0813188106.

35. Poudineh, Mahla, Peter M. Aldridge, Sharif Ahmed, Brenda J. Green, Leyla Kermanshah, Vivian Nguyen, Carmen Tu et al. "Tracking the dynamics of circulating tumour cell phenotypes using nanoparticle-mediated magnetic ranking." *Nature nanotechnology* 12, no. 3 (2017): 274.

36. Mosmann, Tim R., and Robert L. Coffman. "Heterogeneity of cytokine secretion patterns and functions of helper T cells." *Advances in immunology*, vol. 46, pp. 111-147. Academic Press, 1989.

37. Fischbach, Michael A., Jeffrey A. Bluestone, and Wendell A. Lim. "Cell-based therapeutics: the next pillar of medicine." *Science translational medicine 5,* no. 179 (2013): 179ps7-179ps7.

38. Chang, ZeNan L., Pamela A. Silver, and Yvonne Y. Chen. "Identification and selective expansion of functionally superior T cells expressing chimeric antigen receptors." *Journal of translational medicine* 13, no. 1 (2015): 161.

Chapter 1 . Overview: Technical Platforms and Strategies for Digital ELISA

1.1 Introduction

The measurement of protein analytes down to the ultimate sensitivity of single molecules has been achieved by digital ELISA (enzyme-linked immunosorbent assay) technologies. As a branch of digital bioassays[1,2] developed from the maturation of microfluidic biotechnologies, digital ELISA platforms are designed to (1) partition a protein detection reaction into a large number of microcompartments, so that each partition contains a discrete number (0, 1, 2, 3, …) of target proteins; (2) contain an amplified reaction inside each partition, so that partitions containing one or more target proteins (positive partitions) exhibit distinctively higher signals from those containing none (negative partitions); (3) determine the concentration of the target protein by enumerating the positive partitions and analyzing with Poisson statistics.

This first proof-of-concept demonstration of a digital counting of β-galactosidase enzyme in droplets was reported in 1968[3], where single β-gal enzyme was partitioned with its fluorogenic substrate into microdroplets sprayed over silicone oil. Demonstrations of digital ELISA assays containing complete sandwiched ELISA have to wait until microwell based compartmentalization techniques became available.

Compared to some other digital bioassays such as digital PCR, digital ELISA underwent slower technical development and commercial adoption, mainly because of two challenges. First, at the partition step, a solid surface is required for digital ELISA platforms to accommodate the repeated binding and washing steps in building antigen-antibody sandwiches, in contrast to the one-pot reaction mix commonly involved in nucleic amplification. Second, the signal amplification for

ELISA assay relies on the reporter enzyme turning over fluorogenic substrates, a linear process over time compared to the exponential amplification in PCR reactions.

The following discussion covers the two technical challenges mentioned above: partition strategies and signal amplification systems. For partition strategies, we extracted the technical designs and trends emerged in various digital ELISA platforms in the past 15 years, and their respective pros and cons. We also summarized the available signal amplification systems for the high-sensitive detection of signal protein signals, and the challenges and opportunities in their implementation. The third step in building a digital ELISA platform, the analytical basis involving Poisson statistics, has been discussed in depth in several other works[1,4,5].

1.2 Partition Strategies

Designing the partition method is the most important in building digital ELISA. To ensure the functioning of the ELISA assay, the partition system need to (1) be able to compartmentalize a sample into homogenously sized volumes so that the target protein is distributed in a 0 or 1 fashion (translating into Poisson statistics, less then <1% of the partitions containing 2 or more target proteins); (2) be coating with a capturing agent, usually antibodies specific to the target protein, so that the target protein from the partitioned sample can be immobilized; (3) accommodated the repeated incubation and washing steps in common ELISA assay protocols to support the building of antigen-antibody sandwiches, eventually leading to every captured target protein be labeled by reporter enzymes.

The partition strategies also cast their impact beyond the building of the immuno-sandwiches. For one thing, the volume of each partition affects the reaction time. The larger the partitions are, the

longer it takes to collect detectable signals from positive partitions. For another, the total number of the partitions available per process determines the size of the reaction chip, the burden of data processed, and ultimately the limit of detection.

1.2.1 Microchamber arrays

In the earliest demonstrations of homogenously compartmentalized digital enzyme counting, samples containing enzymes were directly partitioned into an array of micron-diameter reaction chambers. These reaction chambers were formed by PDMS stamping[9,10](Figure 1-1a) or etching into a bundle of optical fibers[11–13](Figure 1-1b). By chemically modifying the surface of the microchambers, biotinylating being a common method, these microchambers provide both a solid support to capture the target molecule, and containment for the partitioned reaction volumes.

Despite the appealing simplicity of using microchambers as both partition containment and protein capturing surfaces, a fundamental limitation exists that it takes too long for a molecule to freely diffuse and bind to the surface, even when confined in a micron-diameter reaction chamber, as dictated by Langmuir adsorption kinetics. Theoretical modeling indicated indicate that a 10 fM solution would take three years to equilibrate with a 1 cm^2 surface.[14,15]

Such was the demonstrated need for a strategy to separate compartmentalization and protein binding, where transport and binding of protein molecules to surfaces can be facilitated by fluid mixing rather than depending on the equilibrium of diffusion.

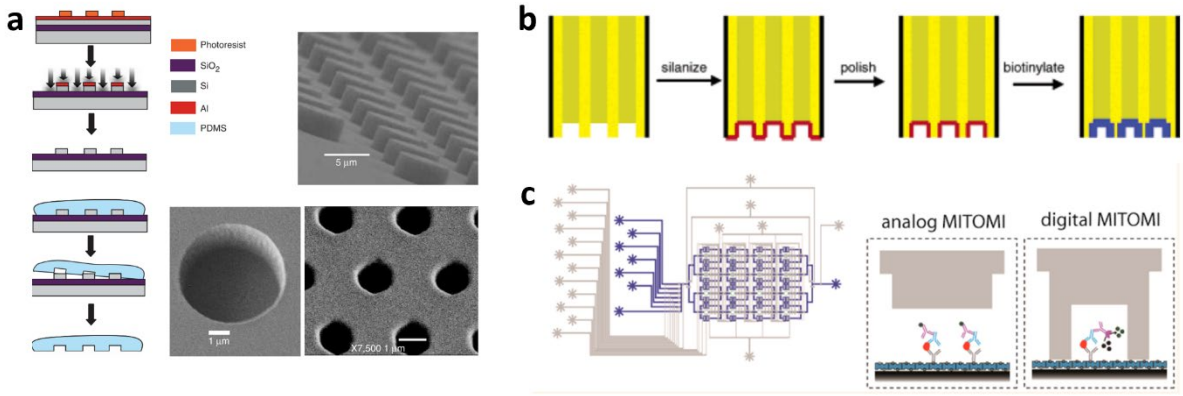

Figure 1-1 Microchamber arrays fabrication for digital ELISA via **(a)** PDMS stamping[10], **(b)** etching into optical fibers[12], and **(c)** deflective PDMS microwells[16].

In one approach designed by Piraino et al.[16], an array of deflective PDMS microwells (Figure 1-1c) could be selectively actuated by hydraulic pressure to digitally compartmentalize a larger reaction chamber that would otherwise remain connected for analog readout, and the protein binding process was facilitated by convection in continuous microfluidics. The majority of the other digital ELISA platforms have particles integrated in their assay workflows.

1.2.2 Particles in microwells

The method of filling barcoded microparticles into microwell arrays first demonstrated by Walt and coworkers[17] addressed the reagent binding issue in microfluidic settings by "bringing the surface to the analyte rather than trying to bring the analyte to the surface"[18]. The first demonstrations of complete ELISA assays in digital bioassay format[19,20] used microparticles to support the immuno-sandwiches, the workflow involving active mixing and centrifuging greatly facilitates molecule interactions, and subsequently fill these particles into microwells of matching sizes.

At a practical level, some of the technical challenges in microwell handling persists. The first challenge a user might encounter is the loading and sealing of microwell arrays, requiring both efficiency and speed due to the fast evaporation of liquid contained in microwells. One strategy to facilitate bead loading is to fabricate microwells with hydrophilic-in-hydrophobic material patterning, where the microwells were assembled to have hydrophilic bottoms (usually SiO_2 as substrate) inside each well, confined by hydrophobic side walls (*e.g.* Teflon-AF[21,22], OSTE[23,24], CYTOP[6,25]) (Figure 1-2a-c).

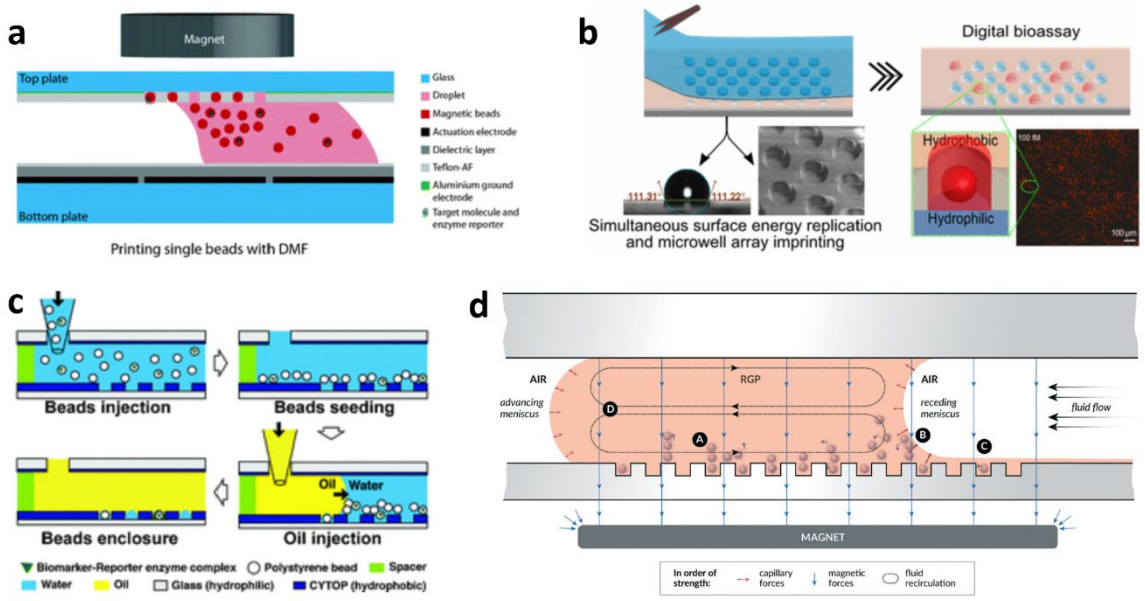

Figure 1-2 Strategies for loading particles into microwells. **(a)** Lammertyn and colleagues developed digital microfluidic (DMF) printing of single superparamagnetic beads into microwells selectively patterned with Terflon-AF.[21] **(b)** Lammertyn and colleagues imprinting of arrays with hydrophilic-in-hydrophobic microwells with self-assembly OSTE+ formulation.[23] **(c)** Noji and colleagues performed vacuum-assisted loading of particles into CYTOP patterned hydrophilic-in-hydrophobic microwells.[25] **(d)** Duffy and colleagues developed magnetic-meniscus sweeping (MMS) method for improving bead loading in arrays of microwells.[7]

Other external forces have also been integrated to further facilitate bread loading, such as (1) leveraging an external magnetic field to pull magnetic particles into microwells (Figure 1-2a,d)[7,21], (2) using use of digital microfluidics to deliver the beads to the microwell array (Figure 1-2a)[21], (3) vacuum-assisted microwell filling (Figure 1-2c)[25], and (4) improved particle loading leveraging capillary forces (Figure 1-2d)[7].

Another problem shared by microwell-based platforms, and to some degree all other digital ELISA platforms, is non-specific binding in the process of building antigen-antibody complexes.[18] Non-target proteins and sometimes the reporter enzymes can stick to surfaces and cause false positive signals. The microwell platforms are also limited in their scalability towards changing sample volumes, as the area of the wells are fixed at the time of fabrication.

1.2.3 Particles in droplets

Droplet microfluidics present interesting solutions to some of the technical problems faced by microwell-based systems. Using various droplet microfluidic designs such as T- or Y-shaped junctions or step emulsifiers, large numbers of water-in-oil droplets can dynamically generated, encapsulating particles pre-incubated to form antigen-antibody complexes. The partition process scales spontaneously with sample volume, and users do not encounter technical challenges resembling particle loading or microwell sealing.

The most prominent challenge for one aspiring to develop a droplet-based digital ELISA platform is to create uniformly-size droplets that are small enough. While microwell-based platforms generally partition reactions into wells <10 μm in all dimensions, droplet generators with <10 μm diameter nozzles will end up generating droplets 20-30 μm in diameter. Larger partitions will in

turn require longer assay time for signals to break out of the noise floor. Abell and colleagues[26] were able to create 5-50 fL volume droplets by operating a flow focusing device at the dripping regime, while Issadore and collegues[8] performed digital ELISA in 22.5 pL droplets with an amplification assay of a high turn-over rate (Figure 1-3a).

Opposed to the relative ease in partition generation, droplet-based digital ELISA platforms pose a unique challenge in term of reading signals from water-in-oil droplets. Unlike microwell arrays fabricated with fixed relative locations, droplets tend to shift around as they float in oil. One common solution is to contain the droplets in a reservoir for imaging (Figure 1-3b)[26], sometimes placing them further into microwell structures for fixed locations[27]. This solution tends to cause low percentage of the total droplets being read. An alternative solution is to capture the signals from droplets as they flow through, which requires a more advanced imaging algorithm capable of reading droplets from several parallel flow lines at high flow rate (Figure 1-3c)[8].

Unique to droplet platforms in the problem of surfactant mediated crosstalk. It is well reported in the droplet microfluidic community that fluorescence signals from positive droplets leak out, and over time stain negative droplets with signals.[28,29] The underlying mechanism of these crosstalk events was considered to be the formation of micellar bodies out of extra surfactant in the environment.[30,31] Since surfactant is indispensable in maintaining the stability of water-in-oil emulsion, unlike the physically defined containment in microwells, it is inevitable to encounter surfactant mediated crosstalk. However, recent studies also suggest such crosstalk also exists in surfactant free interface of aqueous solutions and fluorinated oil.[32]

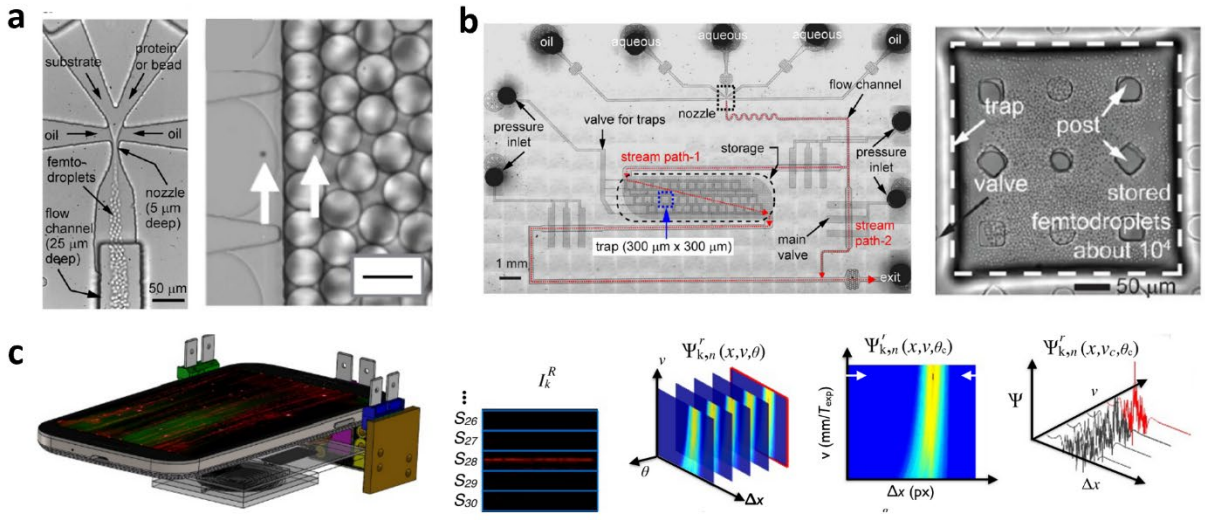

Figure 1-3 Droplet based digital ELISA platforms. **(a)** Droplet generation via flow focusing[26] (left) and step emulsification[8] (right). Scale bar = 50 µm. **(b)** Droplet imaging at fixed locations in an imaging reservoir.[26] **(c)** Imaging analysis of droplets as they pass by in high flow rate.[8]

1.2.4 Uncontained particles

Suzuki and colleagues[33] developed a novel way is to immobilize the amplified signals from signal enzyme molecules back onto their original particles, eliminating the need for oil-based compartmentalization entirely (Figure 1-4a). Tyramide signal amplification (TSA), an immunostaining technical common in immunohistochemistry, was used to deposit signals from HRP reporters back to tyrosine residues present in protein molecules in the vicinity.

This TSA based method demonstrate multiplex capability[34], and more importantly allowed for signal analysis being handled by flow cytometers, largely improving the throughput, capacity, and adoptability of the method. However, it is also risky of crosstalk between positive and negative particles, and the density of particles in a reaction volume needed to be carefully calibrated. Walt and colleagues[35] improved the scheme by fixing the TSA particles in fibrin hydrogel to contain signal crosstalk (Figure 1-4b), although the cytometer compatibility was traded off.

1.2.5 Droplets without solid content

Although conventional ELISA is based on antigen-antibody interaction, several successful attempts were reported adapting nucleic acid amplifications for antigen detection. Kim et al.[36] designed an entropy-driven amplification cycle activated by the proximity of antibodies tagged with catalytic sequences (Figure 1-4c). Byrnes et al.[37] reported containing proximity ligation assays in droplets which converted antigen detection to digital PCR downstream (Figure 1-4d). The platform also features an algorithm to compensate for polydisperse droplet sizes to further streamline sample preparation.[38,39] Abasıyanık et al.[40] also reported digital quantification of low-abundance cytokine biomarkers with droplet based proximity ligation assays (Figure 1-4e).

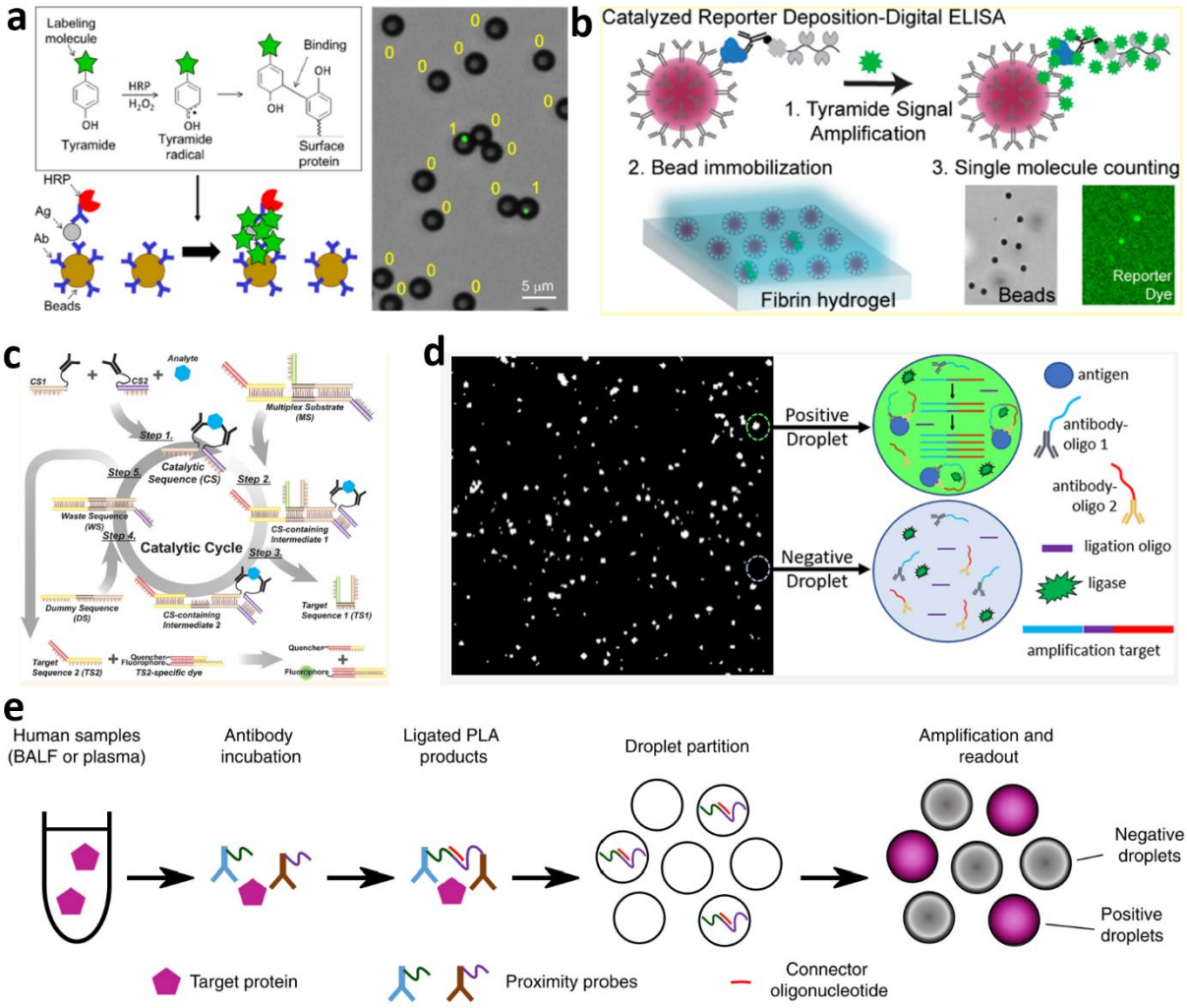

Figure 1-4 Other digital ELISA platforms. **(a)** Suzuki and colleagues[33] developed a TSA-on-particle platform for digital ELISA. **(b)** Walt and colleagues[35] contained TSA particles in fibrin hydrogel. **(c)** Kim et al.[36] designed an entropy-driven amplification cycle where nucleic acid amplification was activated by the proximity of antibodies tagged with catalytic sequences. **(d)** Byrnes et al.[37] reported containing proximity ligation assays in droplets which converted antigen detection to digital PCR downstream. **(e)** Abasıyanık et al.[40] also reported digital quantification of low-abundance cytokine biomarkers with droplet based proximity ligation assays.

1.3 Signal Amplification

The signal amplification system in digital ELISA aims to indicate the existence of single analyte by rapidly generating signaling molecules. The conventional ELISA assay format replies on a reporter enzyme to catalyze substrate molecules turning-over, resulting in fluorescent signals. There is as of today a limited pool for fluorogenic enzyme-substrate pairs, governed by three common enzymes: β-galactosidase (β-gal), horseradish peroxidase (HRP), and alkaline phosphatase (AP). The common substrate-enzyme pairs are presented in Table 1.1.

A larger variety of labeling and signaling molecules will be crucial both to more optimized signal amplification schemes, and to diversify signal amplification strategies for multiplex. Noji and colleagues[32] reported a library of novel fluorogenic substrates for AP reporter enzyme that also exhibit preferable properties in term of resisting dye leakage into fluorinated oil.

It is to be noted that the enzymatic catalytic systems are fundamentally limited in their efficiencies: the linear enzymatic production of signaling molecule is incomparably slow against the exponential amplification of PCR. To this end, the nucleic acid based amplifications discussed in section 1.2.5, particularly digitalized protein detection via proximity ligation assays[37,40], have shown great potential in bridging the gap.

1.4 Performance Metrics

The analytical performance metrics of digital ELISA sheds lights into the room for further technical development. Although many of the metrics, such as sensitivity or limit of detection (LOD), have their correspondence when used on conventional analogue assays, their definition is slightly more complicated when the assay shifts toward digitalization.

Table 1-1 common substrate-enzyme pairs for digital ELISA

Enzyme	Size (kDa)	Substrate	Signals	EX/EM (nm)
β-galactosidase (β-gal)	44	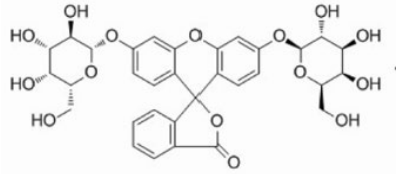 Fluorescein di(β-D-galactopyranoside) (**FDG**)	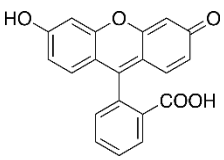 **Fluorescein**	**494/512**
		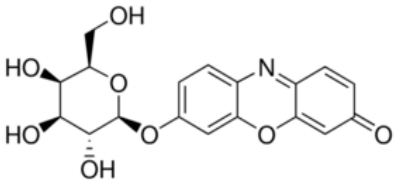 Resorufin di(β-D-galactopyranoside) **(RDG)**	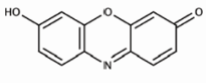 **Resorufin**	**563/587**
horseradish peroxidase (HRP)	464	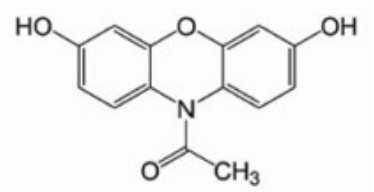 10-Acetyl-3,7-dihydroxyphenoxazine (**ADHP**)		
alkaline phosphatase (AP)	140	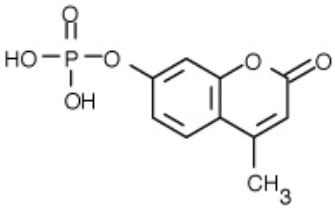 4-Methylumbelliferyl phosphate (**4-MUP**)	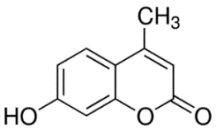 4-Methyl-umbelliferone (**4-MU**)	**372/445**

1.4.1 Sensitivity

Sensitivity is officially defined as the change in signal relative to concentration and is most closely associated with the slope of the calibration curves, which determines the ability to discriminate among similar concentrations of the analyte.[5] Although interchangeable with LOD in analog assays, for the following discussion, we define sensitivity as the capability of an assay to distinguish the existence of single target protein biomarker (positive) from none (negative).

In the signal analysis of digital assays, a positive signal is often defined as greater than 3 standard deviations away from the noise floor (average signal level of all partitions from the negative control group), i.e. the signal to noise ratio.

Provided the noise floor is relatively stable once the imaging set up is determined, the sensitivity of the assay can be improved by (1) deploying an assay of higher turn-over rate; (2) improving the sensitivity of the optical readers, either by upgrading hardware or expanding imaging algorithms; (3) reducing the volume of each partition so that the signals accumulate to a higher effect within the same time frame.

There is, however, several factor that might raise the noise floor, particularly due to persistent false positive signals from negative control experiments. The false positive reading can come from (1) unstable fluorogenic substrate self-supplying false signals, (2) non-specific binding of protein and enzyme reporters, or (3) contaminants in the environment catalyzing substrate turn-over. Particularly, reducing the size of partitions might contribute to elevated non-specific binding due to increased surface-to-volume aspect ratio.

1.4.2 LOD

Although also defined as > 3 standard deviations above negative control, LOD is defined by:

$$\text{mean [percentage positive]}_{neg} + 3\ \text{SD [percentage positive]}_{neg}$$

Netted within this equation, a positive event is defined by:

$$\text{mean [signal]}_{neg} + 3\ \text{SD [signal]}_{neg}$$

What this entails for real-life digital ELISA experiments is that: (1) If abnormal high reads in false negative conditions exhibit enough signal to be counted positive, i.e. $[\text{percentage positive}]_{neg}$ increases away from zero, the LOD of the assay will be hugely affected; (2) At the boundary of the LOD, i.e. low concentrations of target molecuels, where there are only a few (<10) positive partitions to be counted, the discreet chance encounter of positive partitions will cause a large coefficient of variation (CV).

Therefore, the LOD of a digital ELISA platform is dictated first by how clean the amplification is, but more importantly by the number of partitions included in signal analysis. When the number of positive microchambers that could be counted is so limited that its boundary with negative control is ambiguous, there stands the LOD of the assay.

From a technical perspective, scaling up the imaging analysis capacity can be challenging for both microwell and droplet-based platforms. Microwells have a defined number of wells fabricated within the fixed area, and the particle loading efficiency is still being improved.[7] Droplet imaging can be even less flexible due to the location shift of droplets and their limited tolerance towards physical pressure and shearing, although high-throughput reading with cytometers or sorters might

be present future opportunities. In addition, Muñoz et al.[41] developed a hierarchical Bayesian model with bootstrapping performance boundary curves to enhance the LOD via machine-learning based imaging analysis algorithms.

1.4.3 Dynamic rage

In addition to sensitivity and LOD, dynamic range (the range between the minimum and maximum number/concentration of molecules in a sample that can be measured quantitatively) is another important performance metric, although less discussed in the digital bioassays due to the emphasis on the lower detection boundary. Larger number of partitions will hold larger number of molecules in compartments, thus increasing the higher detection boundary. However, there is a physical limitation in partition numbers, limited by either the physical capacity of the platform (especially for microwells) or the available volume of the sample.

Some other strategies to expand the dynamic range include (1) incorporating a capacity for on demand dilution in the assay workflow, (2) distinguishing the difference of summed-up signals from 1-3 molecules instead of analyzing single compartmentalization,[7] and (3) design the platform to be compatible with both digital and analog assays.[16]

References

1. A.S. Basu, *SLAS Technol. Transl. Life Sci. Innov.* **22**, 369 (2017).
2. A.S. Basu, *SLAS Technol. Transl. Life Sci. Innov*. **22**, 387 (2017).
3. B. Rotman, *Proc. Natl. Acad. Sci. United States* **47**, 1981 (1961).
4. D.M. Rissin, D.H. Wilson, and D.C. Duffy, in *Immunoass. Handb.* (Elsevier Ltd, 2013), pp. 223–242.
5. Y. Zhang and H. Noji, *Anal. Chem.* **89**, 92 (2017).
6. T. Ono, T. Ichiki, and H. Noji, *Analyst* **143**, 4923 (2018).
7. C.W. Kan, C.I. Tobos, D.M. Rissin, A.D. Wiener, R.E. Meyer, D.M. Svancara, A. Comperchio, C. Warwick, R. Millington, N. Collier, and D.C. Duffy, *Lab Chip* **20**, 2122 (2020).
8. V. Yelleswarapu, J.R. Buser, M. Haber, J. Baron, E. Inapuri, and D. Issadore, *Proc. Natl. Acad. Sci. U. S. A*. **116**, 4489 (2019).
9. R.J. Jackman, D.C. Duffy, E. Ostuni, N.D. Willmore, and G.M. Whitesides, *Anal. Chem.* **70**, 2280 (1998).
10. Y. Rondelez, G. Tresset, K. V. Tabata, H. Arata, H. Fujita, S. Takeuchi, and H. Noji, *Nat. Biotechnol.* **23**, 361 (2005).
11. P. Pantano and D.R. Walt, *Chem. Mater.* **8**, 2832 (1996).
12. D.M. Rissin and D.R. Walt, *J. Am. Chem. Soc.* **128**, 6286 (2006).
13. D.M.R. and, D.R. Walt*, D.M. Rissin, and D.R. Walt, *Nano Lett*. **6**, 520 (2006).
14. H.J. Lee, A.W. Wark, and R.M. Corn, *Langmuir* **22**, 5241 (2006).
15. T.M. Squires, R.J. Messinger, and S.R. Manalis, *Nat. Biotechnol.* **26**, 417 (2008).
16. F. Piraino, F. Volpetti, C. Watson, and S.J. Maerkl, *ACS Nano* **10**, 1699 (2016).

17. K.L. Michael, L.C. Taylor, S.L. Schultz, and D.R. Walt, *Anal. Chem.* **70**, 1242 (1998).

18. D.R. Walt, *Lab Chip* **14**, 3195 (2014).

19. D.M. Rissin, C.W. Kan, T.G. Campbell, S.C. Howes, D.R. Fournier, L. Song, T. Piech, P.P. Patel, L. Chang, A.J. Rivnak, E.P. Ferrell, J.D. Randall, G.K. Provuncher, D.R. Walt, and D.C. Duffy, *Nat. Biotechnol.* **28**, 595 (2010).

20. R. Iino, S. Araki, S.H. Kim, S. Sakakihara, and H. Noji, in (*15TH Conference on Miniaturized Systems for Chemistry and Life Sciences. Seattle, USA*., 2011).

21. D. Witters, K. Knez, F. Ceyssens, R. Puers, and J. Lammertyn, *Lab Chip* **13**, 2047 (2013).

22. E. Pérez-Ruiz, D. Decrop, K. Ven, L. Tripodi, K. Leirs, J. Rosseels, M. van de Wouwer, N. Geukens, A. De Vos, E. Vanmechelen, J. Winderickx, J. Lammertyn, and D. Spasic, *Anal. Chim. Acta* **1015**, 74 (2018).

23. D. Decrop, G. Pardon, L. Brancato, D. Kil, R. Zandi Shafagh, T. Kokalj, T. Haraldsson, R. Puers, W. Van Der Wijngaart, and J. Lammertyn, *ACS Appl. Mater. Interfaces* **9**, 10418 (2017).

24. R. Zandi Shafagh, D. Decrop, K. Ven, A. Vanderbeke, R. Hanusa, J. Breukers, G. Pardon, T. Haraldsson, J. Lammertyn, and W. van der Wijngaart, *Microsystems Nanoeng*. **5**, 1 (2019).

25. S.H. Kim, S. Iwai, S. Araki, S. Sakakihara, R. Iino, and H. Noji, *Lab Chip* **12**, 4986 (2012).

26. J.U. Shim, R.T. Ranasinghe, C.A. Smith, S.M. Ibrahim, F. Hollfelder, W.T.S. Huck, D. Klenerman, and C. Abell, *ACS Nano* **7**, 5955 (2013).

27. Z. Guan, Y. Zou, M. Zhang, J. Lv, H. Shen, P. Yang, H. Zhang, Z. Zhu, and C.J. Yang, *Biomicrofluidics* **8**, (2014).

28. Y. Chen, A. Wijaya Gani, and S.K.Y. Tang, *Lab Chip* **12**, 5093 (2012).

29. G. Etienne, A. Vian, M. Biočanin, B. Deplancke, and E. Amstad, *Lab Chip* **18**, 3903 (2018).
30. Y. Skhiri, P. Gruner, B. Semin, Q. Brosseau, D. Pekin, L. Mazutis, V. Goust, F. Kleinschmidt, A. El Harrak, J.B. Hutchison, E. Mayot, J.F. Bartolo, A.D. Griffiths, V. Taly, and J.C. Baret, *Soft Matter* **8**, 10618 (2012).
31. P. Gruner, B. Riechers, B. Semin, J. Lim, A. Johnston, K. Short, and J.-C.C. Baret, *Nat. Commun.* **7**, 10392 (2016).
32. S. Sakamoto, T. Komatsu, R. Watanabe, Y. Zhang, T. Inoue, M. Kawaguchi, H. Nakagawa, T. Ueno, T. Okusaka, K. Honda, H. Noji, and Y. Urano, *Sci. Adv.* **6**, eaay0888 (2020).
33. K. Akama, K. Shirai, and S. Suzuki, *Anal. Chem*. **88**, 7123 (2016).
34. K. Akama, K. Shirai, and S. Suzuki, *Electron. Commun. Japan* **102**, 43 (2019).
35. A.M. Maley, P.M. Garden, and D.R. Walt, *ACS Sensors* **5**, 3037 (2020).
36. D. Kim, O.B. Garner, A. Ozcan, and D. Di Carlo, *ACS Nano* **10**, 7467 (2016).
37. S.A. Byrnes, T. Huynh, T.C. Chang, C.E. Anderson, J.J. McDermott, C.I. Oncina, B.H. Weigl, and K.P. Nichols*, Anal. Chem*. **92**, 3535 (2020).
38. S.A. Byrnes, E.A. Phillips, T. Huynh, B.H. Weigl, and K.P. Nichols, *Analyst* **143**, 2828 (2018).
39. T. Huynh, S.A. Byrnes, T.C. Chang, B.H. Weigl, and K.P. Nichols, *Analyst* **144**, 7209 (2019).
40. M.F. Abasıyanık, K. Wolfe, H. Van Phan, J. Lin, B. Laxman, S.R. White, P.A. Verhoef, G.M. Mutlu, B. Patel, and S. Tay, *Nat. Commun.* **11**, 1 (2020).
41. H.E. Muñoz, C.T. Riche, J.E. Kong, M. Van Zee, O.B. Garner, A. Ozcan, and D. Di Carlo, *ACS Sensors* **5**, 385 (2020).

Chapter 2 . Single Molecule Detection: Counting of Enzymatically Amplified Affinity Reactions in Hydrogel Particle-Templated Drops

2.2 Introduction

Digital enzyme-linked immunosorbent assays (ELISAs) allow for the measurement of protein biomarkers down to the ultimate sensitivity of single molecules. In contrast to conventional ELISAs performed in ~200 μL reaction volumes, in a digital ELISA workflow, a sample containing a target protein is partitioned into numerous sub-nanoliter microreactors such as microwells or emulsion droplets, such that each partition contains a quantized number of target molecules. If the volume of each partition is small enough, hence the total number of the partitions great enough, many of the microreactions will comprise either 0 or 1 target molecules with a distribution governed by Poisson statistics[1].

The differentiation of positive partitions (containing 1 or more target molecules) from negative partitions (containing 0 target molecules) requires a signal amplification mechanism associated with the presence of a target molecule inside a partition. Similar to well plate-based ELISA, reporter enzymes such as horseradish peroxidase (HRP), β-galactosidase (β-gal), or alkaline phosphatase (AP) are used to catalytically react with their fluorogenic substrates and linearly amplify signal. Since the signals generated by the reporter enzymes are contained within the original partition, the measurement of target protein concentration is reduced to counting the number of positive partitions containing signals above-background.

While detection of a single β-gal enzyme was achieved as early as 1961 by spraying a mixture of β-gal and its fluorogenic substrate over silicone oil[2], the reliable measurement of low-abundance protein biomarkers posts two to the partitioning strategy. First, the digital ELISA platform needs to produce and process a large number (~ 10^5-10^6)[3,4] of highly homogenously sized partitions. Monodisperse partition size ensures uniform reaction conditions among all partitions, and thus the signals from the partitions can be directly compared. Second, the partitions need to contain a solid surface to support the immobilized target protein molecules, subsequently formed enzyme-linked immunocomplexes, and sustain repeated washing required for ELISA workflows.

Since microfluidics enabled the fabrication or generation of large numbers of homogeneously sized microscale compartments, digital counting of β-gal enzymes was first demonstrated in microwell arrays[5] and optical fibers[6], and matured into full-scale digital ELISA assays in which microwells were loaded with particles[7,8] conjugated with immuno-complexes, leveraging the convenient mixing and washing of micro-particles to expediate the binding of target molecules to their surfaces.[9] Since the commercialization of microwell-based digital ELISA represented by Quanterix Simoa, new discoveries have been enabled in the diagnosis and mechanistic studies of various diseases[10] such as for Alzheimer's disease[11], cancers[12–14], cardiovascular diseases[15,16], cytokine inflammatory markers[17,18], and tuberculosis[19]. Similar well plate-based platforms include deflectable button microwells[20] and pre-equilibrium microarrays[21].

Another design of digital ELISA platforms encapsulates particles into microfluidically-generated and surfactant-stabilized droplets[22,23]. Compared to microwell approaches where the number of microwells are fixed per wafer design and scaling up complicates device handling[24], the droplet

approach scales more freely, since droplets can be produced at up to ~10^6/s[22,23] and as many or few can be utilized as the downstream analysis approach allows. However, using random binding and encapsulation to realize conditions of a single molecule per particle and single particle per droplet, results in <~1% of all droplets containing a single molecule on a single particle, following Poisson statistics. On microwell-based platforms the particle loading efficiency is increased by sizing well cavities for a single particle and infusing an overwhelming supply of particles, however, the majority of them are washed out and uninterrogated[25].

Another problem shared by microwell and droplet platforms is the cost or operational complexity for end users without microfluidic skills or infrastructure. Both microwells and droplet generators require specialized microfluidic skills to operate or rely on commercial solutions that are specialized and not widely available. Efforts to simplify the partitioning hardware include (1) entirely removing partitioning by depositing signals onto particles in-situ with tyramide signal amplification[26,27] although spacing strategies are required to prevent signal crosstalk amongst particles[28]; and (2) relaxing the monodispersity requirement by statistically compensating for volume polydispersity[29], adapted to a one-pot reaction[30].

We present a lab-on-a-particle assay mechanism as a further democratized solution for digital enzyme reaction counting. Hydrogel particles are utilized here both as a solid support to immobilize protein molecules, and as a template for emulsification around the hydrogel matrix. Previously, we and others have shown that spherical particles[31,32] or particles with tailored surface chemistry[33,34] can be used to template drop formation to perform measurements of DNA and protein biomarkers. In this work, we performed digital counting of β-gal enzyme on spherical

polyethylene glycol (PEG) hydrogel particles templating drops of ~20 pL volume and achieved femtomolar detection limit. The assay workflow is performed solely with standard bench-top equipment and techniques. We envision this lab-on-a-particle mechanism for single enzymatic reaction counting to lay a foundation for democratizing digital ELISA technologies.

2.2 Materials and Methods

2.2.1 Device fabrication

Step emulsifiers

Step emulsifier microfluidic droplet generators were fabricated using soft lithography. Master molds were fabricated on mechanical grade silicon wafers by a two-layer photolithography process with KMPR 1010 and 1050 (MicroChem Corp), the first and second layers defining the height of the nozzle channel and the reservoir region respectively. The nozzle channel measured 700 μm (L) × 20 μm (W) × 7.2 μm (H), and the droplet collection reservoir measured 4 cm (L) × 2 mm (W) × 80 μm (H) and were confirmed using a Veeco Dektak 150 Surface Profiler. Devices were molded from the masters using PDMS Sylgard 184 kit (Dow Corning). The base and crosslinker were mixed at a 10:1 mass ratio, poured over the mold, degassed, and cured at 65 °C overnight. PDMS devices and cleaned glass microscope slides (VWR) were then activated via air plasma (Plasma Cleaner, Harrick Plasma) to form permanent bonding. The bonded devices were then treated with Aquapel for 1 min and rinsed with Novec 7500 oil (3M) to render the channels fluorophilic. After surface treatment, devices were placed in an oven at 65 °C for 1 h to evaporate the residual oil in the channels.

Imaging reservoirs

To image dropicles and particles, imaging reservoirs sizing 5 cm (L) × 3 cm (W) × 50 μm (H) were fabricated using the same soft lithography techniques, allowing dropicles or particles to form a single layer when imaged.

2.2.2 Production of hydrogel particles

Hydrogel precursor solution containing 10 wt% 8-arm PEG-vinylsulfone (JenKeM Technologies), 0.5 mg/ml biotin-PEG-thiol (Nanocs), 4 ng/ml maleimide labeled with Alexa Fluor 568 or 488 (Life Technologies), and 2 wt% dithiothreitol (Sigma-Aldrich) crosslinker was buffered in a 0.15M triethanolamine (Sigma-Aldrich) solution at pH = 5, and injected as the dispersed phase into the step emulsifier at 300 μL/hr, along with a continuous phase composed of Novec 7500 fluorinated oil and 1 wt% PicoSurf (Sphere Fluidics) at 1500 μL/hr to generate a water in oil emulsion.

At the device outlet, a second continuous phase containing 3 vol% triethylamine (Sigma-Aldrich) in Novec 7500 was introduced in a PTFE tubing (Zeus) via a Y junction connection (IDEX Health & Science) to increase the pH of the gel precursor droplets to pH 8 and initiate hydrogel crosslinking. Oil containing the organic base was injected using a Hamilton gastight syringe at 150 μL/hr. The residence time in the tubing between introduction of the organic base and the collection tube was around 4 min. All solutions were injected into the step emulsification device at defined flow rates using syringe pumps (Harvard Apparatus PHD 2000).

After incubating for 8 hr at room temperature, crosslinked particles were extracted from the emulsion by disrupting the emulsion with 20 wt% perfluoro-octanol (Sigma-Aldrich) in Novec 7500 oil at a 1:1 volume ratio. PBS was added immediately to swell and disperse the particles, followed by a few repeats of hexane (Sigma-Aldrich) extraction steps where the oil contents are extracted into a low-density hexane phase and pipetted out from the top. The particles were then filtered with Falcon 40 μm Cell Strainers (Corning) to remove oversized particle aggregates and debris and suspended in PBS supplemented with 0.1 wt% Pluronic F-127 (Sigma Aldrich). The density of the particle suspension was measured using standard cell counting techniques or a flow cytometer. The particles were stored at 4 °C for long term storage up to several months, and usually suspended at a density of 106 particles /mL for ease of use in assays.

2.2.3 Affinity binding on particles

Stored particle suspension was taken out of the fridge and homogenized by inversion. A calculated volume of suspension containing the desired number of particles was transferred to a protein LoBind microcentrifuge tube (Eppendorf) using Ultra Low Retention pipette tips (Corning) and spun down for 15 seconds using a benchtop centrifuge (Stellar Scientific). A translucent pellet of hydrogel particles could be seen at the bottom of the tube. The supernatant was discarded and replaced with 50 μl solutions of the target binding molecule at varying concentrations. The mixture was gently pipetted to dislodge and pellet and incubated on a rotating rack. After incubating for 1 hour, the particles were washed 4 times following similar centrifuge – solution exchange – mixing steps in PBS containing 0.1% Pluronic F-127.

2.2.4 Dropicle formation

The particles were suspended in PBS supplemented with 0.1% Pluronic F-127 and pelleted for use. For enzymatic amplification assays, the fluorogenic substrate was also diluted in PBS with 0.1% Pluronic F-127 to a concentration of 100 μM, 5 μl of this substrate solution was gently mixed with the particles. An oil phase of Novec 7500 with 1% PicoSurf was immediately added, and this mixture was pipetted for 2 minutes at an approximate rate of 120 pipette aspiration-dispensing cycles per minute to create an emulsion of uniform dropicles.

The volume ratio of the aqueous phase and the oil phase is important for the emulsion quality. For all the enzymatic assays in this work, a pellet of 500,000 particles was mixed with 5 μL substrate solution and emulsified in 80 μL oil. 0.1% Pluronic F-127 in the aqueous phase was also important for the emulsion quality.

2.2.5 Enzymatic affinity assays in particle templated droplets

β-gal amplification reaction

500,000 hydrogel particles were incubated with a 50 μl sample solution containing streptavidin-β-galactosidase (Sigma Aldrich) for 1 hour on a rotating rack set to 10 rotations per minute. Following incubation, particles were washed 4 times with PBS supplemented with 0.1% Pluronic F-127 and pelleted. 10 μL fluorescein-di-beta-galactopyranoside (FDG, Sigma Aldrich) solution at 100 μM in 0.1% Pluronic F-127 was mixed with the pellet. 80 μL of Novec 7500 with 0.5% PicoSurf was added to the pellet and immediately emulsified. The emulsion was incubated for 20 hours at room temperature covered in foil.

HRP amplification reaction

500,000 hydrogel particles were incubated with a sample solution containing Pierce High Sensitivity Streptavidin-HRP (Thermo Scientific) for 1 hour on a rotating rack set to 10 rotations per minute. Following incubation, particles were washed 4 times with PBS supplemented with 0.1% Pluronic F-127 and pelleted. Inside a dark room, 10 μL QuantaRed reaction solution (Thermo Scientific) mixed according to the manufacturer's protocol was added the pellet. 80 μL of Novec 7500 with 0.5% PicoSurf was mixed with the pellet and immediately emulsified. The emulsion was immediately transferred to an imaging reservoir for signal readouts.

2.2.6 Affinity binding facilitated by active absorption

500,000 hydrogel particles were pelleted and washed in 500 μL ethanol for 3 times. After removing the ethanol supernatant after the third wash, the microcentrifuge tube containing the particles was placed inside a desiccator with the cap of the tube left open and kept in vacuum for 30 minutes in room temperature. Completely dried particles should be found at the bottom of the tube. Enzyme solutions were added directly to the dried particles, and immediately mixed with the rehydrating particles by gentle pipetting. The following incubation and emulsification steps are the same as above.

2.2.7 Signal readout using fluorescence microscopy

An imaging reservoir was first filled with Novec 7500, followed by dropicles transferred by pipetting. The dropicles spread out into a single layer inside the reservoir since the height of the reservoir does not allow 2 particles stacked vertically. The reservoir containing the emulsion is

then placed on the imaging stage of a Nikon Eclipse Ti2 Series equipped with a Photometrics Prime cMOS camera and scanned for 40 consecutive fields of views.

For β-gal/FDG/fluorescein reactions, each field of view was imaged in the FITC channel with 500 ms exposure to measure enzymatic signal in droplets, followed by 100ms in the TRITC channel to identify particles labelled with Alexa Fluor 568. For HRP/ADHP/resorufin reactions, each field of view was imaged in the TRITC channel with 40 ms exposure to measure enzymatic signal in droplets, followed by the FITC channel with 40 ms exposure to identify particles labelled with Alexa Fluor 488.

Image analysis algorithms were constructed in MATLAB to analyze the fluorescence signal of each dropicle by averaging signals over the particle. A positive signal is determined by thresholding 2.5x standard deviations above the mean of the background signals. Occasional occurrences of dropicles containing multiple hydrogel particles (>2%) were excluded from signal analysis.

To calculate the limit of detection (LOD), we measured the number of false positives in replicate (N=3) negative control samples. The detection threshold was set at MEAN+2.5SD (the sum of the mean fraction of false positives with 2.5 standard deviations of the fraction false positives), and the LOD was calculated by the intersect of the regression with the detection threshold.

The theoretical average enzyme per particle (AEP_{theo}) was determined by Poisson distribution statistics where the average number of enzymes per particle $\lambda = AEP_{theo}$ and the discrete occurrences of enzyme bound on particles $X = x$ ($x = 0, 1, 2$, etc.) follows:

$$P(X = x) = \frac{\lambda^x e^{-\lambda}}{x!}$$

In the digital regime of the assay where the dropicles were either positive (x > 0) or negative (x = 0), the experimental average enzyme per particle (AEP_{exp}) was calculated from the fraction of positive particles (f_p) [53]:

$$AEP_{exp} = - \ln (1 - f_p)$$

2.3 Results

2.3.1 High throughput production of hydrogel particles

Hydrogel particles used in this work are monodisperse spherical PEG hydrogel particles, composed of 8-arm PEG-vinylsulfone as the main scaffold, crosslinked with DTT with 80% of the thiol crosslinking sites occupied by DTT, and functionalized with biotin-PEG-thiol to introduce biotin moieties and maleimide conjugated fluorophores to impart fluorescence to locate the particles for imaging analysis. Particle production follows our published pH-modulated step emulsification method35 (Figure 2-1a), yielding droplets with diameters of 25.3 ± 1.4 μm. This step emulsifier is operated at a frequency of 625 KHz, with potential to scale up. The quality of the emulsion remains consistent over a 10-hour production period as shown by the CV of the droplet sizes (Figure 2-2).

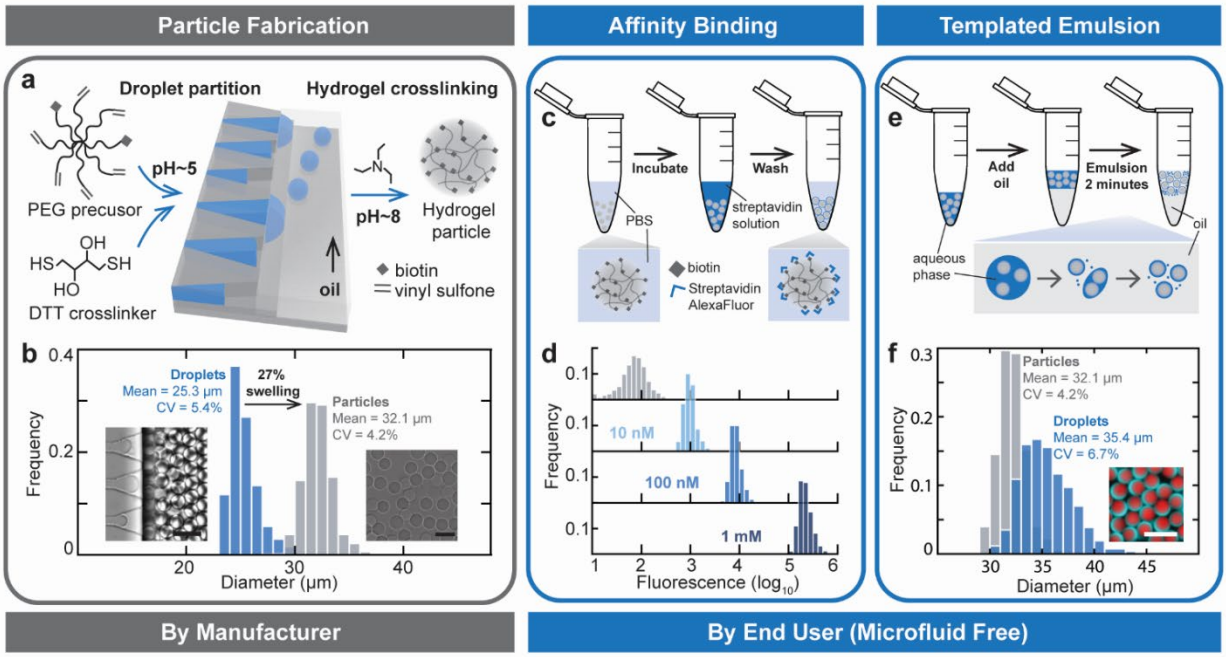

Figure 2-1 Workflow for enzymatic affinity assays in dropicles. **(a)** Hydrogel particles were produced using step emulsification of polymer precursor droplets at a low non-reactive pH. Droplets containing polymer precursors were crosslinked into hydrogel particles by an increase in pH from 5 to 8. **(b)** Hydrogel particles retrieved from the emulsion droplets (d = 25.3 ±1.4 µm, n = 1,428) swelled 27% in diameter, resulting in hydrogel particles 32.1 ±1.3 µm in diameter (n = 1,122). Bright field microscopy images of droplets and crosslinked hydrogel particles show a change in their refractive index. Scale bar = 50 µm. **(c)** Schematic of affinity binding of fluorescent streptavidin on biotin-modified hydrogel particles following incubation and washing step. **(d)** The fluorescence intensity of particles is correlated to the concentration of the streptavidin solution incubated with particles with a narrow distribution (n = 10,000). **(e)** Schematic of the formation of droplet templated emulsion (i.e. dropicles) created by vigorous pipetting. **(f)** Histograms of size of the dropicles (d = 35.4 ± 2.4 µm, n = 257) compared to the hydrogel particles (d = 32.1 ±1.3 µm, n = 1,122) are shown. Scale bar = 100 µm.

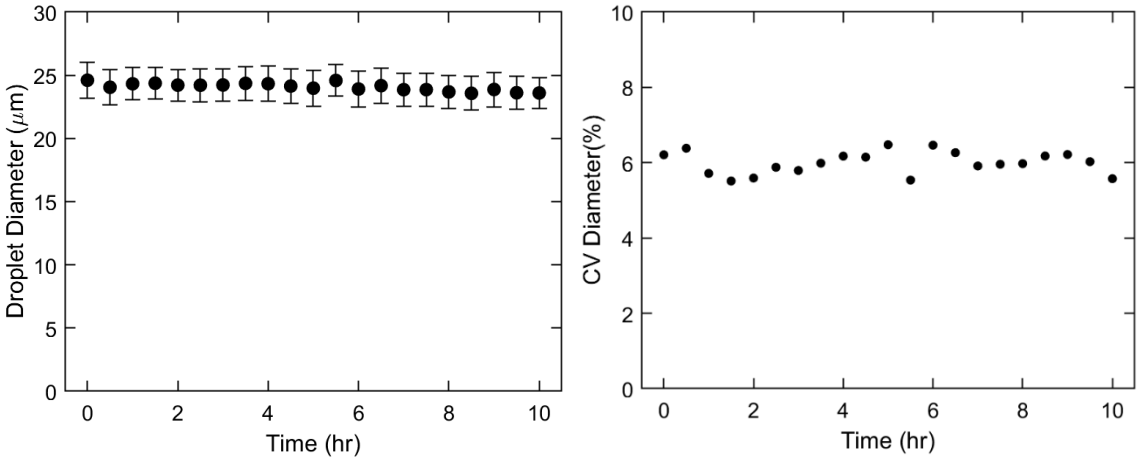

Figure 2-2 The mean diameter of droplets produced over a 10-hour period using the step emulsifier microfluidic device remains consistent, with CV values around 6%. (n = 150-300 for each 30-minute time point).

At the droplet collection site, an organic base was introduced in an additional oil phase to modulate the aqueous droplets to pH~8 and induce crosslinking via Michael addition reaction. Crosslinked hydrogel particles were retrieved by breaking the emulsion and washing with hexane and aqueous buffers; after washing the particles go through a 27% swelling in an aqueous suspension and are filtered through a 40 μm cell strainer to removed particles with malformed crosslinks. The resulting hydrogel particles had a mean diameter of 32.1 μm with a 4.2% CV (Figure 2-1b).

2.3.2 Affinity binding on hydrogel particles

Biotin functionalization of particles enables affinity binding to fluorescent streptavidin (Figure 2-1c) with a dose response spanning at least 3 orders of magnitude. After incubating 500,000 hydrogel particles with Alexa Fluor 488 tagged streptavidin, bright fluorescent rings were seen surrounding the particles, suggesting streptavidin bound to the biotin moieties on the particle surfaces. (Figure 2-3a) 10,000 particles from each incubation were analyzed for the homogeneity of the fluorescent signal, yielding CV values of 7.8%, 5.5% and 3.8% for 10nM, 100nM and 1mM streptavidin concentrations which indicate uniform affinity binding across the particles (Figure 2-1d). A linear correlation could be found between the fluorescence of the particles and the concentration of streptavidin, with a nanomolar limit of detection for unamplified direct binding on these particles (Figure 2-3b).

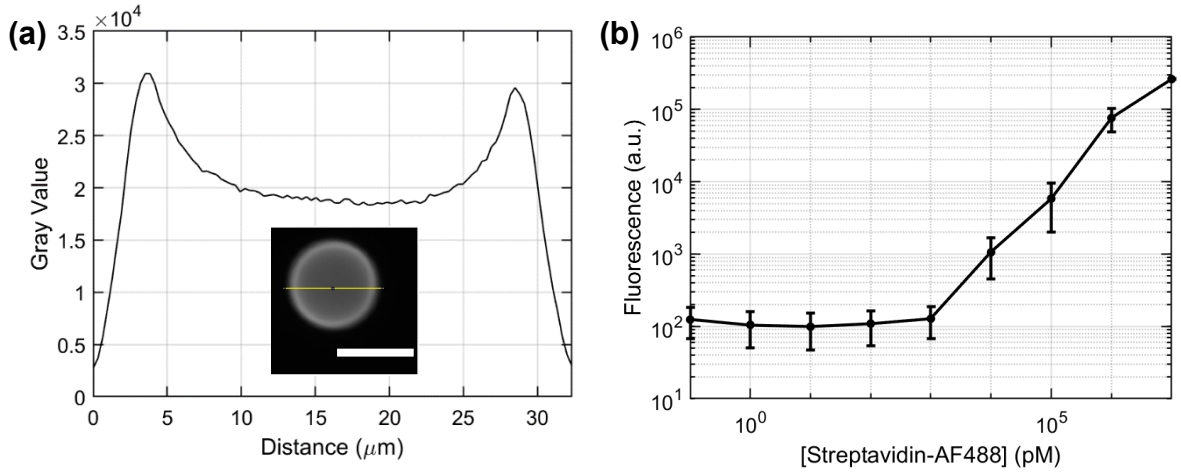

Figure 2-3 Streptavidin binding to biotinylated particles. **(a)** Fluorescence signal is localized to the outer surface of the hydrogel particle, forming a bright edge on the boundary of the particle in a 1D fluorescence intensity slice. **(b)** The integrated fluorescence signal from particles with bound streptavidin-Alexa Flour 488 after incubation are linearly correlated to the concentration of the streptavidin solution across 5 orders of magnitudes. The lowest resolvable signal was around 1 nM, representing the limit of detection for an unamplified affinity assay on the particles using our microscopy setup. (n = 10,000 for each streptavidin concentration.)

2.3.3 Particle-templated emulsions

Monodisperse droplets templated by hydrogel particles, which we refer to as dropicles, were formed by agitation with an oil and surfactant. When an aqueous suspension of hydrogel particles is mixed with a phase of fluorinated oil and agitated by vigorous pipetting, the shearing from pipetting breaks up the aqueous phase into consequently smaller volumes, until the aqueous layer surrounding a particle is too thin to be further broken up (Figure 2-1e, 2-4). With optimized surfactant constituents the dropicles exhibit a mean diameter of 35.4 μm with a CV of 6.7%, closely approximating the size of the hydrogel particle templates (Figure 2-1f). Thus, by simple agitation we were able to create uniform partitions of 20.6±5 pL volume, without the use of microfluidic components such as droplet generators or microwells in forming the compartments.

2.3.4 Performance of enzymatic affinity assays

We proceeded to perform enzymatic amplification assays on hydrogel particles, following the affinity binding and templated emulsion workflow described above. The particles were first incubated with an enzyme solution to capture the target enzyme molecules, washed, and then emulsified with a solution of a fluorogenic substrate specific to the enzyme (Figure 2-5a). When the fraction of the enzyme molecules introduced and bound to particles was below 0.1 of the total particle loading, enzymes were captured on particles in a quantized manner, and digitized fluorescent signals were observed within dropicles.

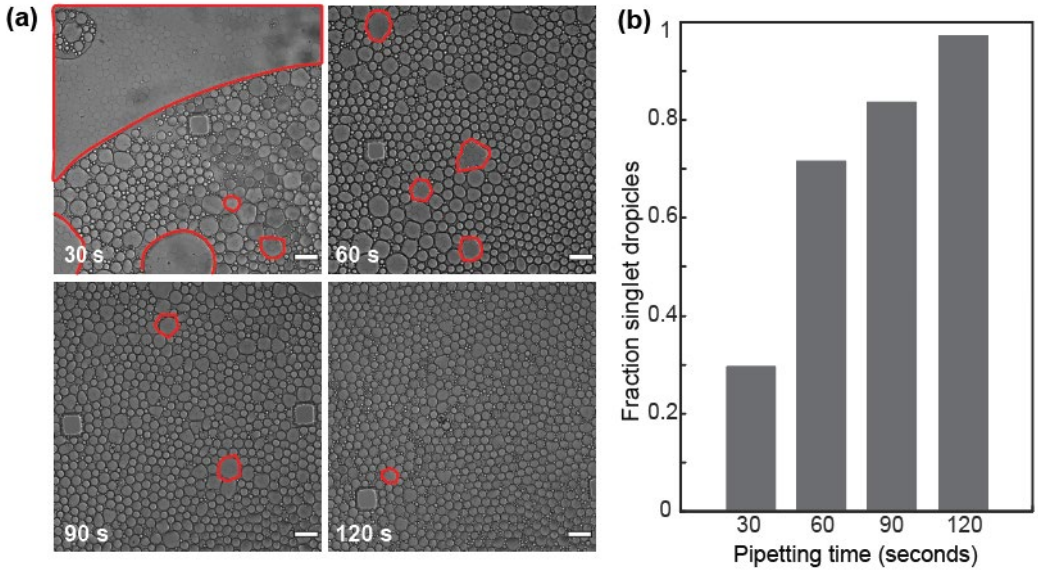

Figure 2-4 Optimizing the quality of dropicle formation with increased pipetting time. **(a)** Bright field images showing the formation of dropicles at 30 second intervals of vigorous pipetting. The number of droplets containing multiple hydrogel particles (highlight by red contour) decreased with increased pipetting time. Scale bar = 100 μm. **(b)** The fraction of singlet dropicles (droplets templated by only one particle) increased with time, approaching 100% after 120 seconds of pipetting.

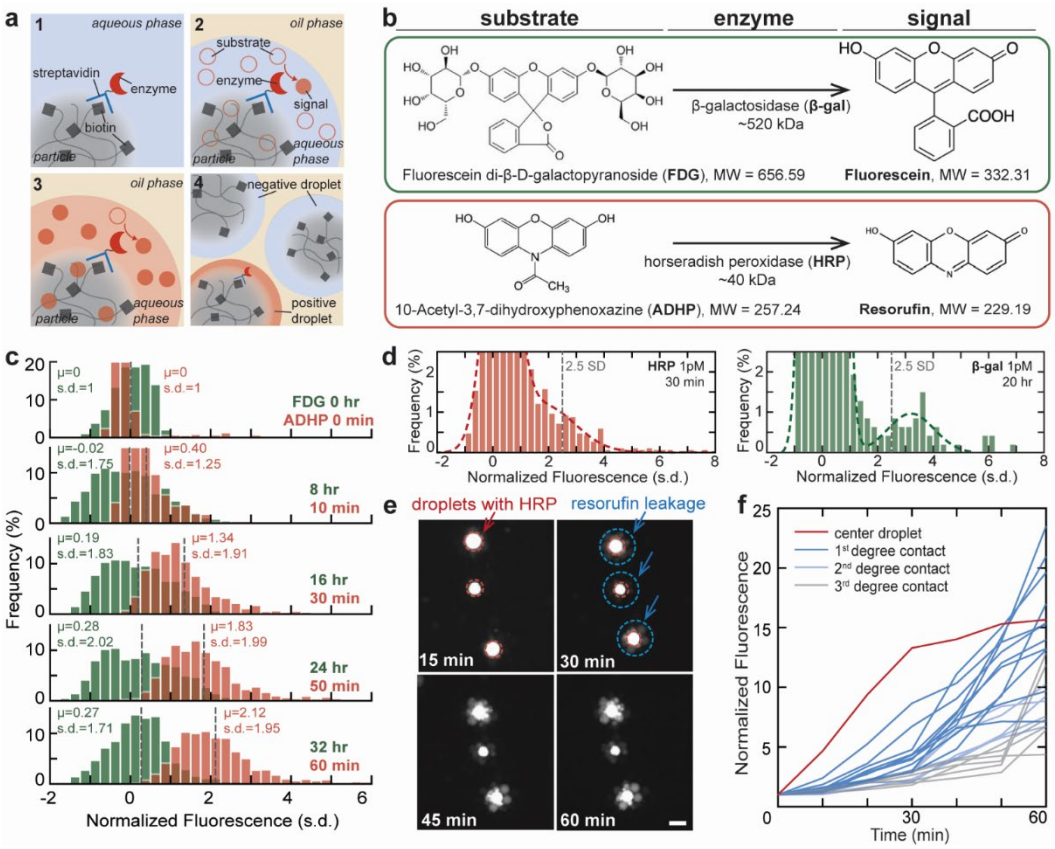

Figure 2-5 Comparison of enzymatic amplification systems in dropicles. **(a)** Workflow for digital enzymatic amplification assays performed on hydrogel particles. **(b)** Chemical mechanisms for the conversion of fluorogenic precursors to fluorescent molecules for the two enzymatic amplification systems examined on hydrogel particles. **(c)** Comparison of the stability of FDG and ADHP substrates within their respective assay time frame. Signals at later time points were normalized against their measurement at t=0. (nFDG ~3,000, nADHP ~1,200.) **(d)** Histogram for dropicles after reacting particles with 1 pM of either HRP or β-gal in their respective enzymatic amplification systems after 30 minutes and 24 hours respectively. Signals were normalized against measurement at t=0. A threshold for positive droplets was set to 2.5 standard deviations above the background mean signal. The histograms were fit with a double Gaussian distribution model indicating the resolution of a no signal population and distinct positive population. **(e)** Fluorescence images of resorufin leaking out of the original HRP-containing droplets (marked in red) into nearby droplets (marked in blue) over 60 minutes. Scale bar = 50 µm.Fluorescence signals over time for an HRP-containing droplet and nearby droplets over 60 minutes.

We compared the performance of two enzyme systems, evaluating substrate stability, turn-over rate, and signal containment within dropicles. Horseradish peroxidase (HRP) and β-galactosidase (β-gal) are the two most common reporter enzymes used in digital ELISA due to the commercial availability of their fluorogenic substrates (Figure 2-5b). HRP catalyzes the conversion of its substrate 10-acetyl-3,7-dihydroxyphenoxazine (ADHP) into resorufin exhibiting bright fluorescence in the 560– 610 nm range. β-gal catalyzes the hydrolysis of β-galactosides through the breaking of the glycosidic bond by a two-step hydrolysis process[36,37]. Multiple fluorogenic substrates of β-gal are commercially available, including those which produce resorufin and fluorescein (e.g. fluorescein-di-beta-galactopyranoside, FDG).

Turnover rate

The HRP/ADHP system has significantly higher turnover than the β-gal/FDG system. Resorufin signal generated by HRP can be distinguished within 10 minutes of initiating a reaction in dropicles and plateaus around 30 min (Figure 2-6), while sufficient fluorescein signal from the turnover of FDG by β-gal enzyme requires overnight reaction[38,39].

Substrate stability

We measured the chemical stability of FDG and ADHP substrates contained in particle-templated droplets in the absence of enzymes (i.e. negative control for enzymatic assays). Due to the difference in turnover rate, droplets containing FDG reaction mix were incubated overnight and imaged at 8-hour intervals, while droplets with ADHP reaction mix were imaged every 10 minutes. The signals from later time points were normalized against their initial readings at $t = 0$.

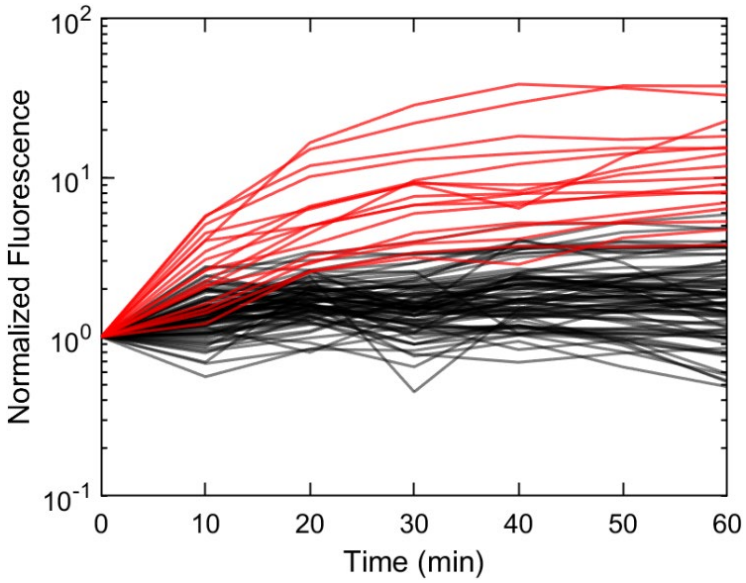

Figure 2-6 Signals of dropicles loaded with the HRP/ADHP/resorufin system analyzed at 10-minute intervals indicating the enzymatic amplification completed at around 30 minutes. The fluorescence signals of each dropicle were normalized against their starting fluorescence at t=0. Red lines refer to signals from positive dropicles (containing particles bound with at least 1 HRP enzyme), black lines correspond to negative dropicles. (n = 101)

While the baseline intensity distribution from the turnover of FDG without enzyme remained similar to their initial readings, spreading slightly in standard deviation (an increase of 0.27 ± 1.71 standard deviations over a 32-hour monitoring window), the intensity distribution from the ADHP reaction mix shifted 2.12 standard deviations higher in intensity on top of a wider (1.95 standard deviations) distribution (Figure 2-5c). This can be explained by the photooxidation of ADHP to resorufin[40] in a peroxidase environment, where the ADHP substrate self-decomposes into resorufin fluorophores unaided by HRP. This baseline level of turnover of the ADHP substrate resulted in a higher noise floor that requires higher levels of enzyme-produced signal to robustly distinguish enzyme containing drops (Figure 2-5d).

Signal containment

While fluorinated oils ubiquitous in droplet microfluidic assays have very low solubility for large or highly charged biomolecules, dye leakage has been widely reported and attributed to a surfactant mediated transport of small molecules such as fluorophores[41–43], with resorufin reported to be transported more readily than fluorescein[44,45]. This transport, coupled with the large heterogeneity in enzyme activity within a single population of enzymes, can prevent significant accumulation of fluorescent signals in droplets thereby precluding accurate digital molecular counting.

Since surfactant is necessary for the formation of dropicles, leakage of resorufin fluorophores was significant and could be observed from as early as 15 minutes following compartmentalization and initiation of reactions (Figure 2-5e). Fluorescent signals could be detected at even higher levels from satellite droplets surrounding a positive particle as more time passed, up to 60 minutes. Further analysis shows while the reaction in the center HRP-containing droplet plateaus after 30

minutes, signals from the neighboring droplets continue to increase, likely as a combined consequence of dye leakage and the baseline turnover of resorufin molecules.

To decouple enzymatic activity from fluorophore leakage, we observed the transport of fluorescein and resorufin dyes loaded in dropicles by emulsifying particles with fluorescein and resorufin solutions and tracking the signal changes over time. Normalized based on photobleaching, the loss of resorufin fluorophores was rapid with >80% loss of signal within the first 30 minutes of reaction, while the leakage of fluorescein reached e quilibrium after 20 minutes with the majority of the fluorophores remaining within the dropicle (Figure 2-7).

Weighing turnover rate, substrate stability, and signal containment, although the HRP/ADHP system had a higher turnover rate leading to a shorter incubation time, the high baseline turnover of ADHP substrate without enzyme and the transport of converted resorufin signaling molecules out of dropicles are both expected to reduce the accuracy of measurements. We therefore decided to use the β-gal/FDG enzyme system for single enzymatic reaction counting on hydrogel particles with an overnight incubation for the enzymatic amplification step.

2.3.5 Enzymatic affinity assay for digital molecule counting

We performed digital counting of β-galactosidase enzyme molecules. Hydrogel particles were incubated with streptavidin labeled β-gal at concentrations from 2.5 fM to 4 pM, washed, and then emulsified with FDG substrate mixture.

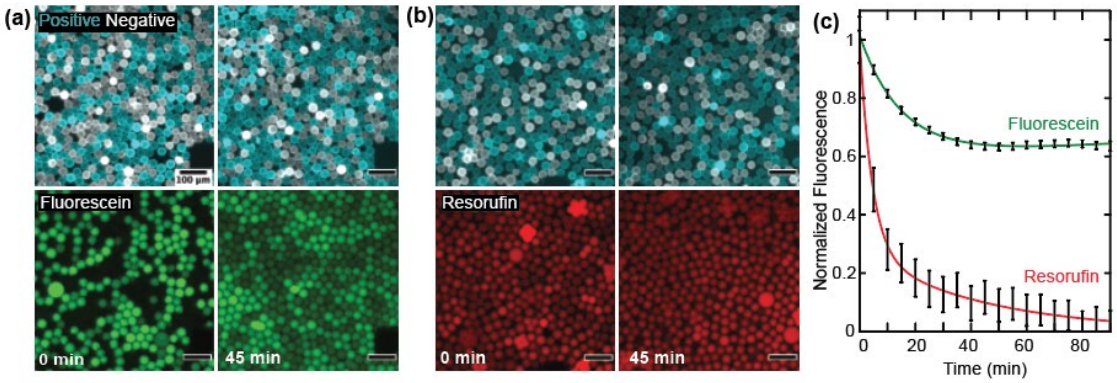

Figure 2-7 Transport of resorufin and fluorescein in dropicles. **(a)** Fluorescence signals from fluorescein containing dropicles, the location of which indicated by the cyan color filter on the top images, transported towards negative dropicles during a 45-minute incubation. Scale bar = 100 µm. **(b)** Fluorescence signals from resorufin containing dropicles transported towards negative dropicles during a 45-minute incubation. **(c)** Normalized fluorescence intensities over 90 minutes observation showing the transport of fluorescein is slower than resorufin, and ~65% of fluorescein signal was retained at equilibrium. Error bars indicate the standard deviation of all dropicles observed.

After a 20-hour incubation, dropicles were transferred to a reservoir for imaging and analysis. Droplets exhibiting fluorescent signals >2.5 standard deviations higher than the mean intensity of negative control droplets were counted as positive (i.e. containing 1 or more molecules of β-gal, Figure 2-8c). Around 50,000 dropicles were imaged from each reaction, and 3 repeats were performed for each β-gal concentration.

The fraction of positive droplets showed a linear correlation with the starting β-gal concentration over 3 orders of magnitudes ($r^2 = 0.998$). The limit of detection for β-gal enzyme counting was 2.5 fM (Figure 2-8a). By back calculating from the fraction of positive droplets per experiment to average number of enzymes per particle (AEP) following Poisson statistics, we observed a linear correlation between the experimental average enzyme per particle (AEP) and the theoretical AEP with $r^2 = 0.933$ (Figure 2-8b).

2.3.6 Enhancing binding using active absorption of sample

We take advantage of the absorption of fluid by the hydrogel particles once dried to facilitate binding of enzyme driven to the particle surface by the rehydrating flow (Figure 2-9a,b). Due to the high weight fraction (~90%) of water in the volume of our hydrogel particles they shrink in size significantly when undergoing a drying process and swell when rehydrated, drawing fluid into their interior. The diameter of hydrogel particles increased from 16.3 ± 1.6 μm to 30.3 ± 2.4 μm during rehydration (Figure 2-10). This rehydration process completes within ~2 seconds for each particle, resulting in a 6.4x volume increase (Figure 2-9c). This corresponds to a calculated convective flow to the surface of ~7 micrometers/sec.

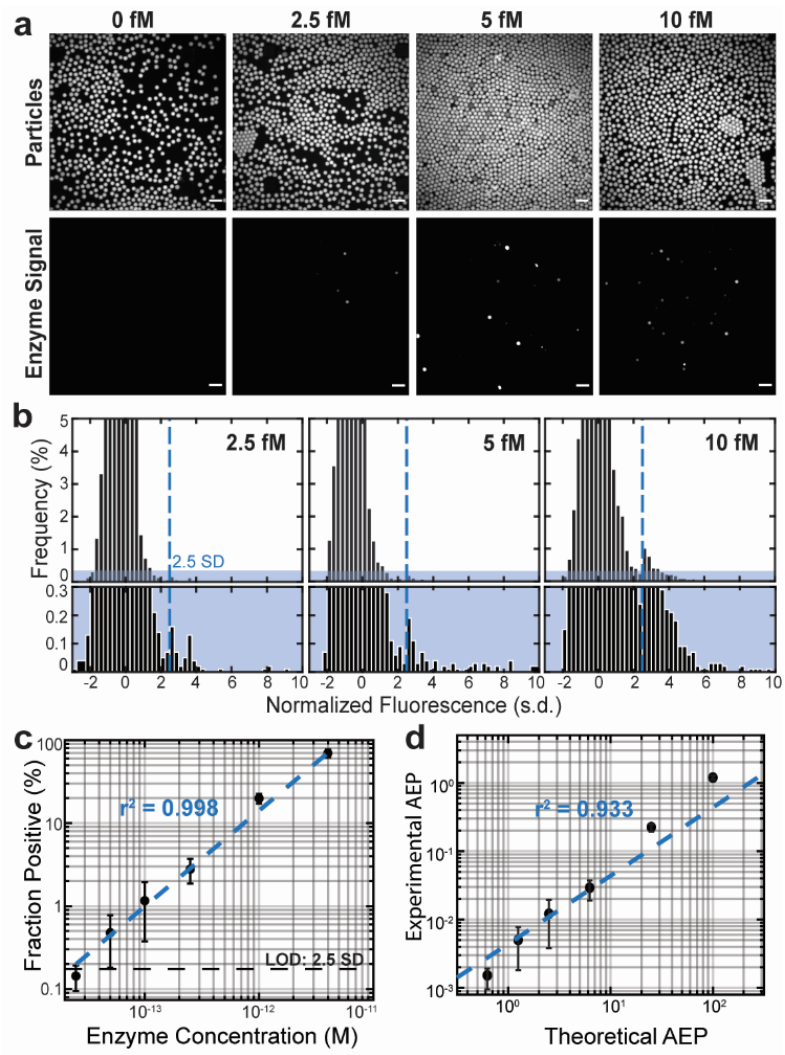

Figure 2-8 Digital counting of β-gal enzymes in dropicles. **(a)** Fluorescence microscopy images of particles (TRITC) incubated with β-gal enzyme at difference concentrations, and the digitalized fluorescein signals (FITC) from the dropicles indicating events of enzymatic amplification. Scale bar = 100 µm. **(b)** The fraction of positive dropicles (defined by FITC signals >2.5 SDs above the mean background fraction) correlates linearly to the concentration of β-gal enzyme loaded onto particles (r^2 = 0.998, n ~ 50,000, N = 3). We observe a 3-order of magnitude dynamic range with a limit of detection at 2.5 fM. **(c)** The experimental average enzyme per particle (AEP) correlates linearly with theoretical values across the range of the experimented β-gal concentrations (r^2 = 0.933, N = 3). **(d)** Distribution of fluorescence signals in dropicles from particles incubated with 2.5 fM, 5 fM and 10 fM β-gal solutions. Positive droplets (defined by signals >2.5 SDs above the mean background intensity) increased in frequency with higher β-gal concentrations.

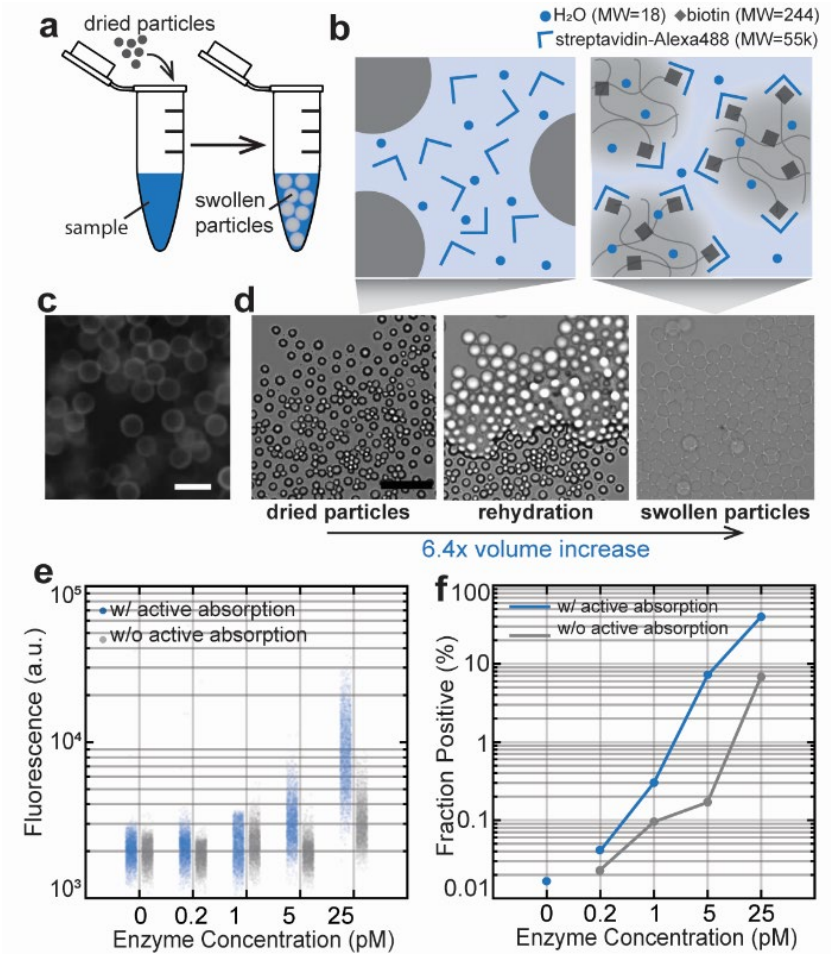

Figure 2-9 Enzymatic amplification assays facilitated by active absorption by hydrogel particles. **(a)** Schematic of the experimental operations for active absorption using dried hydrogel particles. **(b)** Schematic of the mechanism of active absorption during rehydration of hydrogel particles with sample solution. **(c)** Fluorescence microscopy images showing streptavidin-Alexa Fluor 647 binding to hydrogel particle surfaces following active absorption. Bright fluorescent rings around the particles shows streptavidin did not penetrate the hydrogel particle matrix due to the hydrogel's limited porosity. **(d)** Bright field microscopy images showing dried hydrogel particles swelling in volume during rehydration, resulting in a 6.4x volume increase. Scale bar = 50 µm. **(e)** The fluorescence signal at a given concentration of enzyme and **(f)** the percent positive dropicles increased with active absorption (n ~ 50,000).

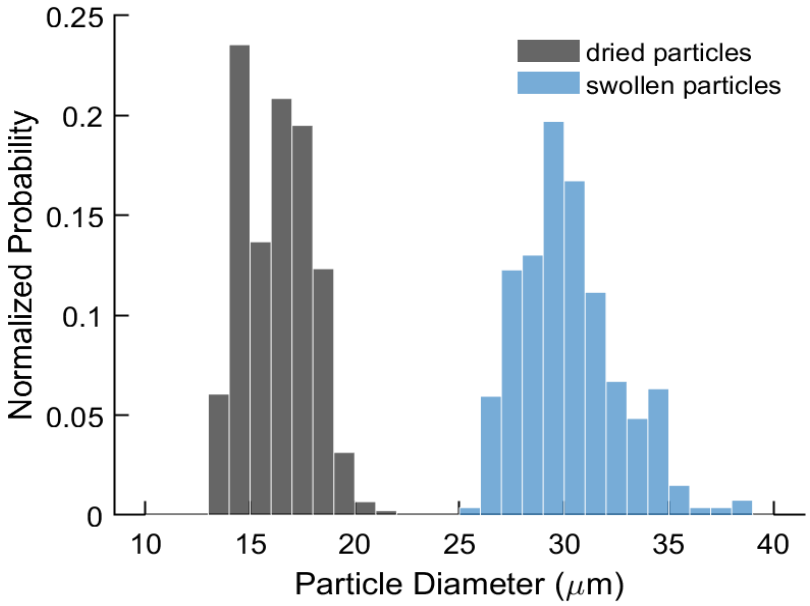

Figure 2-10 Change of particle size during the rehydration process of active absorption. Dried particles (d_1 = 16.3 ± 1.6 μm, n_1 = 446) swelled into hydrated particles (d_2 = 30.3 ± 2.4 μm, n_2 = 269), yielding a 6.4-fold in the total volume of the spherical hydrogel particles.

Swelling particles absorb water and other aqueous content into their hydrogel matrix, but the porosity of the hydrogel material prevents larger molecules and proteins from penetrating the matrix. This can be visualized on the hydrogel particles used in this work by the rapid formation of fluorescent rings when particles are incubated with fluorescent streptavidin (MW = 55kDa) (Figure 2-9d). This behavior contrasts with the homogenous fluorescence across the particles when filling with small dye molecules (MW = 244Da) not attached to proteins. As a result, during the rehydration process when the hydrogel particles absorb water and swell in size, larger molecules such as streptavidin and enzymes are driven onto their surface, achieving higher local concentrations and effectively facilitating binding to particles (Figure 2-9b).

We performed a side-by-side comparison of unfacilitated binding with binding facilitated by active absorption for digital counting of β-gal. Various concentrations of β-gal dilution were added to the same numbers of hydrated and dried hydrogel particles and incubated on a rotating rack for the same amount of time. The particles were then prepared for the standard FDG/fluorescein compartmentalization, signal generation, and imaging. We observe increased sensitivity for assays facilitated with active absorption binding, indicated by an increase in the fraction of positive droplets for the same concentration (Figure 2-9e). For concentrations beyond the digital counting regime, the increased binding yielded an increase in the fluorescence signals among all droplets in the same reaction. This indicates a potential to leverage the volume elasticity of hydrogel particles to effectively increase sample concentration, and lower limits of detection.

2.4 Discussion

2.4.1 The hydrogel particle-based workflow

In this work we demonstrated a lab-on-a-particle approach to digital counting of single enzyme molecules, leveraging the hydrophilicity of hydrogel particles to act as wick to drive flow to the particle surface, the solid particle surface as a support for immunocomplexes and a boundary for uniform droplet generation with random mixing. The combination of these features effectively reduces the need for microfluidic components for the creation of homogeneously sized partitions. Thus, the burden of microfluidics falls solely on the initial generator of hydrogel particles. Once supplied particles, the end user can perform digital affinity assays with standard benchtop techniques like pipetting and centrifugation.

Besides a streamlined workflow, the hydrogel particle approach also overcomes the limit of double Poisson loading, since the process of templated emulsion is not governed by Poisson statistics. In fact, leaving as little aqueous solution as possible to the particle suspension before emulsification is preferred for better emulsion results. We have also found the reliability of the emulsion results depends on the intensity and length of agitation, the volume ratio of the aqueous and oil phases, and the surfactant constituents in aqueous and oil phases. Additionally, this approach to batch emulsification and processing is highly scalable, where to increase the number of desired droplets, the user only needs to increase the number of template particles.

The hydrogel materials of these particles allow the physical and chemical properties of the particles to be customized for the specific need of the assays. The biotin conjugation moieties in this work could be swapped into other common functional groups such as succinimides, aptamers, nucleic

acids, and antibodies. Multiplex labeling and barcoding could be integrated into the particle matrix. The porosity and rigidity of the particles could also be controlled by the selection of hydrogel matrix.

2.4.2 Digital enzyme counting on particles

When demonstrating digital counting of β-gal enzymes with enzymatic signal amplification in particle templated emulsions, we noticed a reduced experimental compared to theoretical AEP. Similar observations were reported in other studies on digital protein counting[7,26,46]. Since a linear correlation was observed between the experimental and theoretical AEPs regardless of the shift, we hypothesize that this shift reflects either a loss of molecules when streptavidin-β-gal was incubated with particles for binding, or amid the agitation process during emulsification. The increase in sensitivity achieved by using active absorption supports this interpretation that loss of target molecules occurs during the incubation step.

Besides loss of target molecules, another factor limiting the sensitivity of particle-based enzyme counting is the capacity of imaging analysis. Although 500,000 dropicles were formed, only ~50,000 ended up imaged with the current microscopic set up. Limits of detection and quantitative accuracy could be improved if the emulsified particles are analyzed with high-throughput flow cytometers capable of processing 500,000 or more dropicles, as this will help decrease the Poisson noise from false positive counting[8,9,47]. These cytometers are often equipped with more sensitive detectors like photomultiplier tubes that will also help further distinguish positive and negative signals. While others have analyzed double emulsions in flow cytometers[48,49] since dropicles are supported by a hydrogel particle core they may be more likely to sustain fluid shear stresses in a

flow cytometer that can operate with an oil continuous phase, for example the On-Chip Sort[50]. Ultimately, we envision the hydrogel particles can be produced at centralized sites and conveniently distributed to enable highly sensitive immunoassays for various biomarkers. No significant changes in the physical and chemical properties of the particles were observed when stored for up to 3 months at 4°C in a buffered aqueous solution. We have also explored alternative storage conditions such as ethanol and lyophilized. Together these capabilities lay the groundwork for a minimally instrumented and accessible "lab-on-a-particle" solution to the analysis of molecules[51] and cells[52] at the ultimate limits of biology.

2.5 References

1. A. S. Basu, SLAS Technol. Transl. Life Sci. Innov., 2017, 22, 369–386.
2. B. Rotman, *Proc. Natl. Acad. Sci.*, 1961, 47, 1981–1991.
3. D. H. Wilson, D. M. Rissin, C. W. Kan, D. R. Fournier, T. Piech, T. G. Campbell, R. E. Meyer, M. W. Fishburn, C. Cabrera, P. P. Patel, E. Frew, Y. Chen, L. Chang, E. P. Ferrell, V. von Einem, W. McGuigan, M. Reinhardt, H. Sayer, C. Vielsack and D. C. Duffy, *J. Lab. Autom.*, 2016, 21, 533–547.
4. T. Ono, T. Ichiki and H. Noji, *Analyst,* 2018, 143, 4923–4929.
5. Y. Rondelez, G. Tresset, K. V. Tabata, H. Arata, H. Fujita, S. Takeuchi and H. Noji, *Nat. Biotechnol.*, 2005, 23, 361–365.
6. D. M. Rissin and D. R. Walt, *J. Am. Chem. Soc.*, 2006, 128, 6286–6287.
7. D. M. Rissin, C. W. Kan, T. G. Campbell, S. C. Howes, D. R. Fournier, L. Song, T. Piech, P. P. Patel, L. Chang, A. J. Rivnak, E. P. Ferrell, J. D. Randall, G. K. Provuncher, D. R. Walt and D. C. Duffy, *Nat. Biotechnol.*, 2010, 28, 595–599.
8. S. H. Kim, S. Iwai, S. Araki, S. Sakakihara, R. Iino and H. Noji, *Lab Chip*, 2012, 12, 4986–4991.
9. D. R. Walt, *Lab Chip*, 2014, 14, 3195–3200.
10. C. Wu, A. M. Maley and D. R. Walt, *Crit. Rev. Clin. Lab. Sci*., 2020, 57, 270–290.
11. S. S. Hwang, H. Chan, M. Sorci, J. Van Deventer, D. Wittrup, G. Belfort and D. Walt, *Anal. Biochem.,* 2019, 566, 40–45.
12. A. Darlix, C. Hirtz, S. Thezenas, A. Maceski, A. Gabelle, E. Lopez-Crapez, H. De Forges, N. Firmin, S. Guiu, W. Jacot and S. Lehmann, *BMC Cancer*, 2019, 19, 110.

13. A. Bera, M. Subramanian, J. Karaian, M. Eklund, S. Radhakrishnan, N. Gana, S. Rothwell, H. Pollard, H. Hu, C. D. Shriver and M. Srivastava, *PLoS One,* 2020, 15, e0242141.

14. A. Vignoli, E. Muraro, G. Miolo, L. Tenori, P. Turano, E. Di Gregorio, A. Steffan, C. Luchinat and G. Corona, *Cancers* 2020, Vol. 12, Page 314, 2020, 12, 314.

15. P. Jarolim, P. P. Patel, M. J. Conrad, L. Chang, V. Melenovsky and D. H. Wilson, *Clin. Chem.*, 2015, 61, 1283–1291.

16. J. Yang, K. Savvatis, J. S. Kang, P. Fan, H. Zhong, K. Schwartz, V. Barry, A. Mikels-Vigdal, S. Karpinski, D. Kornyeyev, J. Adamkewicz, X. Feng, Q. Zhou, C. Shang, P. Kumar, D. Phan, M. Kasner, B. López, J. Diez, K. C. Wright, R. L. Kovacs, P. S. Chen, T. Quertermous, V. Smith, L. Yao, C. Tschöpe and C. P. Chang, *Nat. Commun.,* 2016, 7, 1–15.

17. A. J. Rivnak, D. M. Rissin, C. W. Kan, L. Song, M. W. Fishburn, T. Piech, T. G. Campbell, D. R. DuPont, M. Gardel, S. Sullivan, B. A. Pink, C. G. Cabrera, D. R. Fournier and D. C. Duffy, *J. Immunol. Methods*, 2015, 424, 20–27.

18. L. Song, D. W. Hanlon, L. Chang, G. K. Provuncher, C. W. Kan, T. G. Campbell, D. R. Fournier, E. P. Ferrell, A. J. Rivnak, B. A. Pink, K. A. Minnehan, P. P. Patel, D. H. Wilson, M. A. Till, W. A. Faubion and D. C. Duffy, *J. Immunol. Methods,* 2011, 372, 177–186.

19. R. Ahmad, L. Xie, M. Pyle, M. F. Suarez, T. Broger, D. Steinberg, S. M. Ame, M. G. Lucero, M. J. Szucs, M. MacMullan, F. S. Berven, A. Dutta, D. M. Sanvictores, V. L. Tallo, R. Bencher, D. P. Eisinger, U. Dhingra, S. Deb, S. M. Ali, S. Mehta, W. W. Fawzi, I. D. Riley, S. Sazawal, Z. Premji, R. Black, C. J. L. Murray, B. Rodriguez, S. A. Carr, D. R. Walt and M. A. Gillette, *Sci. Transl. Med*., 2019, 11, 8287.

20. F. Piraino, F. Volpetti, C. Watson and S. J. Maerkl, ACS Nano, 2016, 10, 1699–1710.

21. Y. Song, Y. Ye, S. H. Su, A. Stephens, T. Cai, M. T. Chung, M. K. Han, M. W. Newstead, L. Yessayan, D. Frame, H. D. Humes, B. H. Singer and K. Kurabayashi, *Lab Chip,* 2021, 21, 331–343.

22. J. U. Shim, R. T. Ranasinghe, C. A. Smith, S. M. Ibrahim, F. Hollfelder, W. T. S. Huck, D. Klenerman and C. Abell, *ACS Nano*, 2013, 7, 5955–5964.

23. V. Yelleswarapu, J. R. Buser, M. Haber, J. Baron, E. Inapuri and D. Issadore, *Proc. Natl. Acad. Sci. U. S. A.*, 2019, 116, 4489–4495.

24. Y. Zhang and H. Noji, *Anal. Chem.*, 2017, 89, 92–101.

25. C. Vielsack, R. E. Meyer, C. Cabrera, D. M. Rissin, T. G. Campbell, L. Chang, M. Reinhardt, D. R. Fournier, W. McGuigan, P. P. Patel, D. H. Wilson, V. von Einem, M. W. Fishburn, E. P. Ferrell, E. Frew, T. Piech, H. Sayer, D. C. Duffy, Y. Chen and C. W. Kan, *J. Lab. Autom.,* 2015, 21, 533–547.

26. K. Akama, K. Shirai and S. Suzuki, *Anal. Chem*., 2016, 88, 7123–7129.

27. A. M. Maley, P. M. Garden and D. R. Walt, *ACS Sensors*, 2020, 5, 3037–3042.

28. K. Akama, K. Shirai and S. Suzuki, E*lectron. Commun. Japan*, 2019, 102, 43–47.

29. T. Huynh, S. A. Byrnes, T. C. Chang, B. H. Weigl and K. P. Nichols, *Analyst,* 2019, 144, 7209–7219.

30. S. A. Byrnes, T. Huynh, T. C. Chang, C. E. Anderson, J. J. McDermott, C. I. Oncina, B. H. Weigl and K. P. Nichols, *Anal. Chem.*, 2020, 92, 3535–3543.

31. R. Novak, Y. Zeng, J. Shuga, G. Venugopalan, D. A. Fletcher, M. T. Smith and R. A. Mathies, *Angew. Chemie Int. Ed*., 2011, 50, 390–395.

32. M. N. Hatori, S. C. Kim and A. R. Abate, *Anal. Chem*., 2018, 90, 9813–9820.

33. C. Y. Wu, M. Ouyang, B. Wang, J. de Rutte, A. Joo, M. Jacobs, K. Ha, A. L. Bertozzi and D. Di Carlo, *Sci. Adv*., 2020, 6, eabb9023.

34. G. Destgeer, M. Ouyang and D. Di Carlo*, Anal. Chem*., 2021, 93, 2317–2326.

35. J. M. de Rutte, J. Koh and D. Di Carlo, *Adv. Funct. Mater*., 2019, 29, 1900071.

36. Z. Huang, Kinetic Fluorescence Measurement of Fluorescein Di-j3-o-galactoside Hydrolysis by /3-Galactosidase: Intermediate Channeling in Stepwise Catalysis by a Free Single Enzyme1", *Matchett,* 1991, vol. 30.

37. J. Hofmann and M. Sernetz, *Anal. Biochem.*, 1983, 131, 180–186.

38. Z. Guan, Y. Zou, M. Zhang, J. Lv, H. Shen, P. Yang, H. Zhang, Z. Zhu and C. J. Yang, *Biomicrofluidics*, , DOI:10.1063/1.4866766.

39. B. Porstmann, T. Porstmann, E. Nugel and U. Evers, *J. Immunol. Methods*, 1985, 79, 27–37.

40. B. Zhao, F. A. Summers and R. P. Mason, *Free Radic. Biol. Med*., 2012, 53, 1080–1087.

41. Y. Chen, A. Wijaya Gani and S. K. Y. Tang, *Lab Chip*, 2012, 12, 5093–5103.

42. P. Gruner, B. Riechers, L. A. Chacòn Orellana, Q. Brosseau, F. Maes, T. Beneyton, D. Pekin and J. C. Baret, Curr. Opin. *Colloid Interface Sci*., 2015, 20, 183–191.

43. G. Etienne, A. Vian, M. Biočanin, B. Deplancke and E. Amstad, *Lab Chip,* 2018, 18, 3903–3912.

44. P. Gruner, B. Riechers, B. Semin, J. Lim, A. Johnston, K. Short and J.-C. C. Baret, *Nat. Commun.*, 2016, 7, 10392.

45. Y. Skhiri, P. Gruner, B. Semin, Q. Brosseau, D. Pekin, L. Mazutis, V. Goust, F. Kleinschmidt, A. El Harrak, J. B. Hutchison, E. Mayot, J. F. Bartolo, A. D. Griffiths, V. Taly and J. C. Baret, *Soft Matter,* 2012, 8, 10618–10627.

46. L. Chang, D. M. Rissin, D. R. Fournier, T. Piech, P. P. Patel, D. H. Wilson and D. C. Duffy, *J. Immunol. Methods*, 2012, 378, 102–115.

47. H. E. Muñoz, C. T. Riche, J. E. Kong, M. Van Zee, O. B. Garner, A. Ozcan and D. Di Carlo, *ACS Sensors,* 2020, 5, 385–394.

48. K. K. Brower, K. K. Brower, C. Carswell-Crumpton, S. Klemm, B. Cruz, G. Kim, S. G. K. Calhoun, L. Nichols, P. M. Fordyce, P. M. Fordyce, P. M. Fordyce and P. M. Fordyce, *Lab Chip,* 2020, 20, 2062–2074.

49. K. K. Brower, M. Khariton, P. H. Suzuki, C. Still, G. Kim, S. G. K. Calhoun, L. S. Qi, B. Wang and P. M. Fordyce, *Anal. Chem*., 2020, 92, 13262–13270.

50. K. Takeda, Y. Fujimura and F. Jimma, *Cytom. Res.*, 2011, 20, 43–50.

51. G. Destgeer, M. Ouyang, C. Y. Wu and D. Di Carlo, *Lab Chip*, 2020, 20, 3503–3514.

52. M. Li, M. van Zee, C. T. Riche, B. Tofig, S. D. Gallaher, S. S. Merchant, R. Damoiseaux, K. Goda and D. Di Carlo, *Small,* 2018, 14, 1803315.

53. D. M. Rissin, D. R. Fournier, T. Piech, C. W. Kan, T. G. Campbell, L. Song, L. Chang, A. J. Rivnak, P. P. Patel, G. K. Provuncher, E. P. Ferrell, S. C. Howes, B. A. Pink, K. A. Minnehan, D. H. Wilson and D. C. Duffy, *Anal. Chem.*, 2011, 83, 2279–2285.

Chapter 3 . Workflow Automation: A Ferrobotic System for Automated Microfluidic Logistics

3.1 Introduction

The advent of Industry 4.0 is pioneered by automated guided vehicles (AGVs) that are widely used in distribution and supply chain logistics to perform autonomous, accurate, and consistent cargo transportation while reducing transit times and labor costs[1]. The flexibility and scalability of such mobile automated systems, in conjunction with their ability to assign specific tasks to individual vehicles cooperating in a large network, provide new degrees of automation in comparison with physically constrained conveyor belt or forklift-operated systems[2]. The same degrees of automation are poised to revolutionize applications such as medical diagnostics[3,4], -omics[5-7], drug development[8], and chemical/material synthesis[9]. In that regard, the full potential of these applications can be unlocked by adopting solutions centering on microfluidic logistics, herein defined as the detailed coordination of diverse, large-scale, and small-volume fluid handling operations to perform a plethora of sample processing and analysis tasks.

To this end, conventional continuous-flow microfluidic systems have shown high throughput and robust fluid handling capabilities[10-12]. However, their predefined fluid pathways and geometrically constrained operations severely limit their adaptability and automation, imposing the same limitations as conveyor belt systems within larger-scale settings. Aiming to resolve such constraints, digital microfluidic actuation techniques such as electrowetting-on-dielectric (EWOD) have emerged, capable of transporting discrete droplets on an open surface in a programmable fashion[13-15]. However, inherent limitations of EWOD devices, stemming from the reliance on

direct interactions between the solution and the electrified surfaces, can restrict their service life and compatibility with other peripheral components, thus narrowing their application diversity[16,17].

Here, inspired by the transformational impact of automated guided robotic systems on the manufacturing and distribution industries, we devised a robotic system that uses a network of individually addressable robots, each performing designated micro-/nanofluid manipulation-based tasks in cooperation with other robots. As illustrated in Figure 3-1A, analogous to a standard AGV system—which consists of three primary entities, including a navigation floor, an electric motor, and a cargo carrier for package delivery—our robotic system can be described as: (i) an electromagnetic (EM) navigation floor, which can be programmed to establish localized EM fields in an addressable matrix of coils; (ii) a millimeter-scale permanent magnet as a motor, the movement of which is controlled by the activated EM field(s); and (iii) a ferrofluid droplet carrier, encapsulating the bio/chemical sample of interest (i.e., the "package") that is set in motion upon experiencing strong body forces originating from the interaction of the ferrofluid's magnetic nanoparticle constituents with the motor's magnetic actuation field.

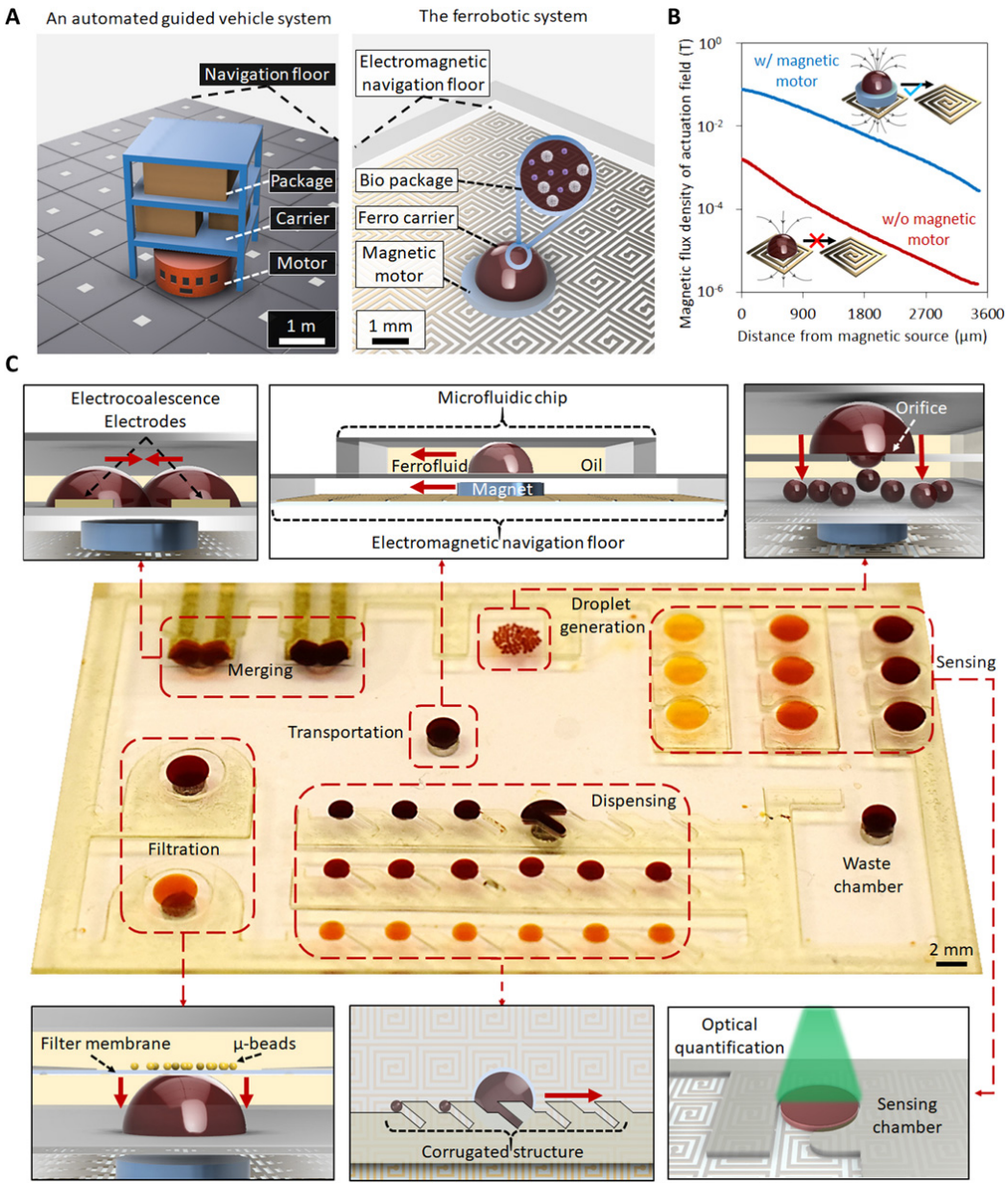

Figure 3-1 Overview of ferrobotic system concept and mechanism. **(A)** An analogy: Mobility and automation in an AGV system and the devised ferrobotic system. **(B)** Simulation results depicting the amplification of the actuation capability with the magnetic motor (the *x* axis is the vertical distance from the center of the magnetic source). **(C)** Optical image of a representative multifunctional ferrobotic system capable of performing diverse operations, including droplet package transportation, merging, generation, filtration, dispensing, and sensing. Rendered images of the droplets are for illustration purposes only (droplets can form hemisphere or disk-like shapes depending on the channel geometry).

Effectively, the devised design leverages EM induction to achieve scalable control, and an intermediary EM-controlled permanent magnet to amplify the actuation field exerted on the ferrofluid (Figure 3-1B). In this way, we overcame the fundamental limitations of previously reported magnetic digital microfluidics, which used complex translational stages and bulky magnets that were not portable[18,19] or EM coils[20,21] that lacked the ample driving forces to execute efficient fluid operations. The addressability and strength of the ferrofluid actuation enable new degrees of mobility and automation central to the devised robotic system, hereafter referred to as "ferrobotic system."

The contactless and high-strength nature of the ferrobotic actuation mechanism inherently renders it rapid, repeatable, and robust. These traits, together with the reconfigurability of the ferrobotic system, can be exploited to integrate passive and active functional components to implement advanced and diverse microfluidic operations (e.g., droplet dispensing, generation, merging, and filtering) besides basic transportation operations (Figure 3-1C). Depending on the objective at hand, a set of these operations can be combined within a disposable microfluidic architecture to deliver versatile system-level microfluidic functionalities.

This high degree of robustness and the individual addressability of ferrobots can be in turn leveraged to deploy a network of ferrobots that carry out generalizable cross-collaborative objectives, centering on microfluidic logistics, such as fluidic package sorting. To illustrate the utility of the ferrobotic system in diverse application spaces, we specifically applied this system to execute a set of cross-collaborative and diverse operations toward the quantification of active matrix metallopeptidases (MMPs; a biomarker for cancer malignancy and inflammation) in human

plasma[22-24], where its reconfigurable functionality and teamwork capability converged to implement a fully automated assay.

3.2 Materials and Methods

3.2.1 Materials for the ferrobotic system

The ferrofluid used in this work refers to ferumoxytol, a U.S. Food and Drug Administration–approved intravenous iron preparation also referred to as Ferraheme (AMAG Pharmaceuticals, MA, USA). Rare earth permanent magnets (D101, 0.8 mm in thickness and 2.54 mm in diameter) were purchased from K&J Magnetics (PA, USA). All microfluidic devices were filled with fluorinated oil (Novec 7500 Engineered Fluid, 3M, MN, USA) containing 0.1% biocompatible surfactant (Pico-Surf 1, Sphere Fluidics, NJ, USA). The design and fabrication of the microfluidic devices and the EM navigation floor are described in detail below.

3.2.2 EM navigation floor circuit design

The EM navigation floor on the PCB comprised an active matrix array of 32 EM coil elements by 32 EM coil elements. Each element had a three-turn coil with a size of 1.5 mm by 1.5 mm stacked on three layers. Adjacent coils were separated by a gap of 0.1 mm, together, giving a total active area of the navigation floor of 51 mm by 51 mm.

Each coil element can be activated when powered by a 0.2-A current, generating a localized magnetic force that attracted the magnetic motor. The specific coil selection was achieved by programming power switch ICs, including MAX14662 (Maxim Integrated, CA, USA) for row

selection and MC33996 (NXP Semiconductors, Netherlands) for column selection in the navigation floor. The target EM coil was selectively actuated when the corresponding row and column lines of its coordinate were activated by switch ICs. Switch ICs were linked by serial peripheral interface (SPI) wires to Arduino Nano, which communicated with a computer through serial communication. Target coordinates preprogrammed or sent from the user interface in the computer were translated to SPI commands by the MCU and then transmitted to switch ICs for addressable activation of the EM coils.

The navigation floor was powered by an external power supply (Keithley 2230-30-1, Tektronix, OR, USA). A DC current source was used for EM coil activation, and the total current I followed the equation: $I = 0.2\ A \times N$ (N is the number of activated coils).

3.2.3 Microfluidic device fabrication

Similar to previous work[50], functional microfluidic devices were created by assembling several layers of double-sided tape (170 μm thick, 9474LE 300LSE, 3M, MN, USA) and transparent polyethylene terephthalate (PET) film sheets (416-T, MG Chemicals, BC, Canada). Microchannels and VIAs (i.e., holes vertically passing through the sheets) were created by laser cutting (VLS 2.30, Universal Laser System, AZ, USA) two-dimensional (2D) patterns within the tape and the PET substrates. Through the alignment of vertical VIAs and microchannels, fluidic connections in both horizontal and vertical directions were achieved, rendering functional 3D microfluidic structures. In some devices, PET sheets were selectively patterned with gold electrodes before assembly. The electrodes were fabricated on PET substrates by photolithography using positive photoresist

(AZ5214E, MicroChemicals, Germany), followed by the evaporation of 20 nm of Cr and 100 nm of Au. After deposition, a lift-off step was performed in acetone.

3.2.4 EM field simulation

To investigate and model the effect of an intermediary permanent magnet on amplification of the actuation magnetic field, we used finite element analysis (COMSOL Multiphysics 5.2, MA, USA) to perform EM simulations. In the simulation setup, magnetic and electric field physics were used in an air environment. The simulation used the same EM coil and permanent magnet dimensions as the experimental setup (fig. S1). The magnetization of the permanent magnet was set according to the product description (278.9 kA/m in axial direction), and the intensity of actuation for the DC current was set as 0.2 A. The magnetic flux density profile was generated on the x-z plane.

3.2.5 Maximum transportation velocity characterization

A microfluidic device with a 40-mm–by 40-mm–by 1.5-mm inner chamber was fabricated, assembled, and filled with oil. The device was placed 2 mm above the navigation floor. A magnetic motor was placed on top of the navigation floor and below the microfluidic device.

Ferrofluid droplets with volume gradients of 0.5 to 10 μl (0.5, 1, 2, 4, 6, 8, and 10 μl) and two different concentrations (100 and 50% ferumoxytol dilution in deionized water) were loaded in the microfluidic chamber. These droplets moved along with the ferrobot, which was sequentially guided by the EM coils actuation in one row from left (y = 1) to right (y = 32). The velocity of the ferrobot was controlled by adjusting the time interval between activating two adjacent coils. If the ferrofluid droplet followed the magnetic motor to the end successfully, then the velocity of the

magnet would increase by shortening the actuation time interval (by 1 ms) in the next round until the droplet failed to follow the magnet.

3.2.6 Characterization of the long-term and oscillatory ferrobotic transportation

A microfluidic device with a 20-mm by 20-mm by 0.7-mm chamber was fabricated and assembled, with a pair of gold electrodes deposited on the substrate as an impedance sensor. A 2-μl ferrofluid droplet was loaded in the oil-filled microfluidic chamber. A magnetic motor was periodically actuated to carry the droplet back and forth between two locations (0.1 Hz). In each cycle, the droplet was first carried away from the sensing electrodes, consequently raising the impedance signal, and then carried back in contact with the electrodes, causing the impedance signal to drop. These actions were repeatedly performed for more than 100,000 s to finish 10,000 cycles. The electrodes were connected to a potentiostat (CH Instrument 660E, TX, USA), and impedance (at 1 kHz) was measured between the two electrodes.

3.2.7 Droplet dispensing setup and procedure

Microfluidic devices (20 mm by 40 mm by 0.7 mm) with corrugated wall structure on one side were fabricated and assembled. Six devices with same corrugated opening length (3 mm) and different opening widths (0.4, 0.6, 1.0, 1.2, 1.4, and 1.8 mm) were tested. A 10-μl parent ferrofluid droplet was loaded in each microfluidic device filled with oil. During the experiment, the parent ferrofluid droplets were transported along the corrugated structures, leaving dispensed droplets in corrugated openings. The sizes of the five dispensed droplets were measured through image analysis.

3.2.8 Droplet generation setup and procedure

Multilayer microfluidic devices with a vertical orifice junction in the middle PET layer (800 μm above the bottom surface) were fabricated and assembled. Different vertical orifices were fabricated by laser cutting and measured under the microscope, resulting in diameters from 80 to 310 μm. A 4-μl parent ferrofluid droplet was loaded in the upper layer of the microfluidic device. During the experiment, the droplet was transported to the vertical orifice junction by a ferrobot and stayed static for 4 s. The diameters of the generated small droplets were measured under a microscope, and volumes were calculated on the basis of the equation of a sphere. The number of droplets was counted for generation rate characterization.

3.2.9 Microfluidic sample filtration setup and procedure

A microfluidic device with a circular polycarbonate membrane incorporated in the top layer (PCTF10047100, Sterlitech, WA, USA) was fabricated and assembled. Monodisperse polystyrene microspheres (25-μm diameter; 24811-2, Polybead, PA, USA) were added in the ferrofluid solution for the experimental characterization of filtration. The sample was diluted from an initial concentration (5.69 × 106 beads/ml) to 8 × 104 beads/ml by ferrofluid. At the start, 1 μl of the bead-containing sample was dropped on the filter membrane. Then, the ferrobot moved to the droplet, located under the membrane region, and remained there for about 10 s until the entire droplet passed through the filter. The number of beads was counted under the microscope before and after filtration.

3.2.10 Droplet merging and mixing setup and procedure

A microfluidic device with patterned electrocoalescence electrodes (area of 2 mm by 2 mm, spaced 1 mm apart, thicknesses of 20 nm of Cr and 100 nm of Au) on the PET substrate was fabricated and assembled. Two 2-μl ferrofluid droplets (10% ferumoxytol solution containing either green or red food dye) were loaded in the oil-filled device. The ferrobot delivered the two droplets at the vicinity of the actuation electrode. DC voltage (2 V) was applied between the two electrodes, causing the droplets to merge. Afterward, the ferrobot either kept the droplet static (shown as "w/o active mixing condition" in Fig. 3L) or induced chaotic motion by the actuated neighboring EM coils within the confines of the coil's coordinates at a frequency of 10 Hz in a cyclic fashion (shown as "w/ active mixing condition" in Fig. 3L). A video recording was taken of the merging process, and the level of mixing was calculated through image processing as discussed below.

3.2.11 Mixing index calculation through image analysis

To quantify mixing efficiency, we characterized the merging of two packages with different colors (red food dye and green food dye in 2 μl of 10% ferrofluid droplet) with or without active mixing. The microfluidic region containing merged droplet was video-recorded, and the corresponding video frames were imported into a MATLAB (Mathworks, MA, USA) in [R, G, B] vector format. Image analysis was performed at droplet region. Similar to previous work[50], a mixing index is defined, as expressed below

$$\text{Mixing index} = 1 - \sqrt{\frac{1}{N-1}\sum_{i=1}^{N}\frac{(\boldsymbol{c}-\boldsymbol{c}_{\text{ave}})^2}{\boldsymbol{c}_{\text{ave}}^2}}$$

where N, ci, and cave are the total number of pixels, the [R, G, B] values at pixel i, and the average [R, G, B] values over N pixels, respectively.

3.2.12 Package-sorting setup and procedure

To implement the sorting of multiple ferrofluidic packages, we fabricated a PCB navigation floor composing of an EM coil array (9 rows and 120 columns) and switch ICs. A microfluidic device with a 20-mm by 120-mm by 0.8-mm inner chamber was fabricated, assembled, and filled with oil. Eight ferrofluid droplets of different volumes (sequentially increasing from 0.5 to 4 μl) were loaded into the chamber and lined in a random order. One ferrobot was placed under each ferrofluid droplets. A top-view image of droplets was acquired and processed by a MATLAB script to identify the droplet sizes and positions, followed by the computation of a navigation plan according to the merge sort algorithm. An on-board microcontroller implemented the navigation plan, which it received through serial communication, by actuating the EM coils according to derived trajectories. The design of the navigation plan took into consideration the maintenance of an interferrobotic distance of 11 mm (seven EM coils apart) to avoid interferrobotic magnetic interference.

3.2.13 Implementation of the pipelined and automated bioassay with the ferrobotic system

A microfluidic device with a source well array, an input well, a dispenser array, a waste chamber, a pair of electrocoalescence electrodes (patterned across all the detection wells), a calibration well array, and an output well was fabricated and assembled as shown in Fig. 5C. Three human plasma samples, 7.2 μl each, spiked with collagenase (0.003, 0.009, and 0.012 U/ml, respectively; Collagenase/Dispase, Sigma-Aldrich, MO, USA), were each mixed with 0.8 μl of ferrofluid and

preloaded in the source well array. Four microliters of 10% (v/v) diluted MMP substrate (MMP Red substrate, AAT Bioquest, CA, USA) in PBS containing 2% (v/v) ferrofluid was preloaded into each of the calibration wells and the output well. The rest of the device was filled with oil. Eight liters of a test sample (a mixture of 0.8 μl of ferrofluid and 7.2 μl of human plasma spiked with collagenase at an arbitrary concentration) was pipetted into the input well. Thereafter, three ferrobots collaboratively performed the sample processing steps of collection, dispensing, delivery, and disposal for each source and test sample. During the sample droplet transportation, on rare occasions, miniscule fractions of the sample break free as satellite droplets, but this artifact could be ignored because the fractions constituted less than 0.5% of the original droplet volume (based on image analysis). Each calibration well or output well ended up receiving two droplets of the samples, respectively, from either the calibration source or the test sample. In situ construction of a calibrator sample was achieved through delivering two different calibration source droplets into one calibration well [e.g., in calibration well no. 2, collagenase with a concentration of 0.006 U/ml would be made by delivering one droplet with a concentration of 0.003 U/ml and another with 0.009 U/ml]. To merge the delivered droplets with the preloaded MMP substrate, we applied a voltage of 2 V across the electrocoalescence electrode pair. After 10 min of incubation, the calibration well array and the output well were imaged using a Nikon Ti-E fluorescence microscope equipped with a Photometrics Prime sCMOS camera (tetramethyl rhodamine isothiocyanate channel, 1-s exposure). Images were processed using ImageJ and MATLAB to quantify the mean fluorescence intensity in the regions of interest.

3.2.14 MMP quantification with a conventional well plate reader

For MMP measurements using a conventional well plate reader, we used 100 μl of calibration and test solutions (a mixture of 50 μl of human plasma spiked with collagenase of various concentrations matching the corresponding ferrobotic experiments and 50 μl of a 1% MMP substrate diluted in PBS). The measurements were performed by a BioTek Cytation 5 Imaging Reader using λ_{ex} = 540/20 nm and λ_{em} = 590/20 nm for 2 hours with lids on.

3.2.15 Human plasma sample

All blood samples were obtained following University of California, Los Angeles, Institutional Review Board (IRB)–approved protocol IRB no. 11-001120 and deidentified. Upon collection, blood was centrifuged using an Eppendorf 5417R Refrigerated Centrifuge, and the supernatant was frozen at -20°C in small aliquots until used.

3.3 Results

3.3.1 Amplified addressable EM actuation

By using the EM coil matrix as the addressable actuator and the millimeter-scale permanent magnet as the magnetic field actuation amplifier, we could realize robust ferrobotic fluid operations within a compact footprint. As seen in the magnetic field simulation results, illustrated in Figure 3-1B and 3-2, the incorporated permanent magnet amplifies the actuation magnetic field by approximately two orders of magnitude (generated from passing a 0.2-A DC current through the EM coil). In this way, high-force actuation of relatively dilute magnetic solutions and/or smaller fluid volumes was achieved, rendering robust fluid transportation. Fluid transportation is

the ferrobotic system's core functionality, where an encapsulated package within the ferrofluidic carrier can be directed by the sequential activation of the EM coils along a desired route on the navigation floor.

The navigation floor was fabricated on a multilayer printed circuit board (PCB), which at its core is composed of a matrix of 32 by 32 EM coils, where each element is realized as a three-layered spiral structure (Figure 3-2). The multilayer implementation allows the proportional increase of the localized EM induction capability of each element for ferrobot attraction. To activate these elements in an addressable manner, we incorporated two integrated circuit (IC) switches in the PCB for row and column selection (Figure 3-3A, B), which are connected to external power sources and controlled by a microcontroller unit (MCU). Depending on the task at hand and by programming at the MCU level, these coils can be sequentially and/or simultaneously activated to engineer the desired paths for a single or multiple ferrobot(s). To illustrate this feature, we programmed the MCU to navigate single ferrobots through U-, C-, L-, and A-like routes (Figure 3-3C), as well as four ferrobots to simultaneously trace the perimeter of a square-like route (Figure 3-4). In all scenarios, the ferrobots successfully carried their designated loads.

As shown in Figure 3-3D and 3-5, with the devised approach, maximum droplet transportation velocities on the order of 10 cm/s could be achieved. The maximum velocity of the droplet initially increased along with its size, showing the dominance of the driving magnetic force on relatively small droplets. The following decrease in maximum velocity illustrates the increased dominance of frictional forces beyond a certain droplet size.

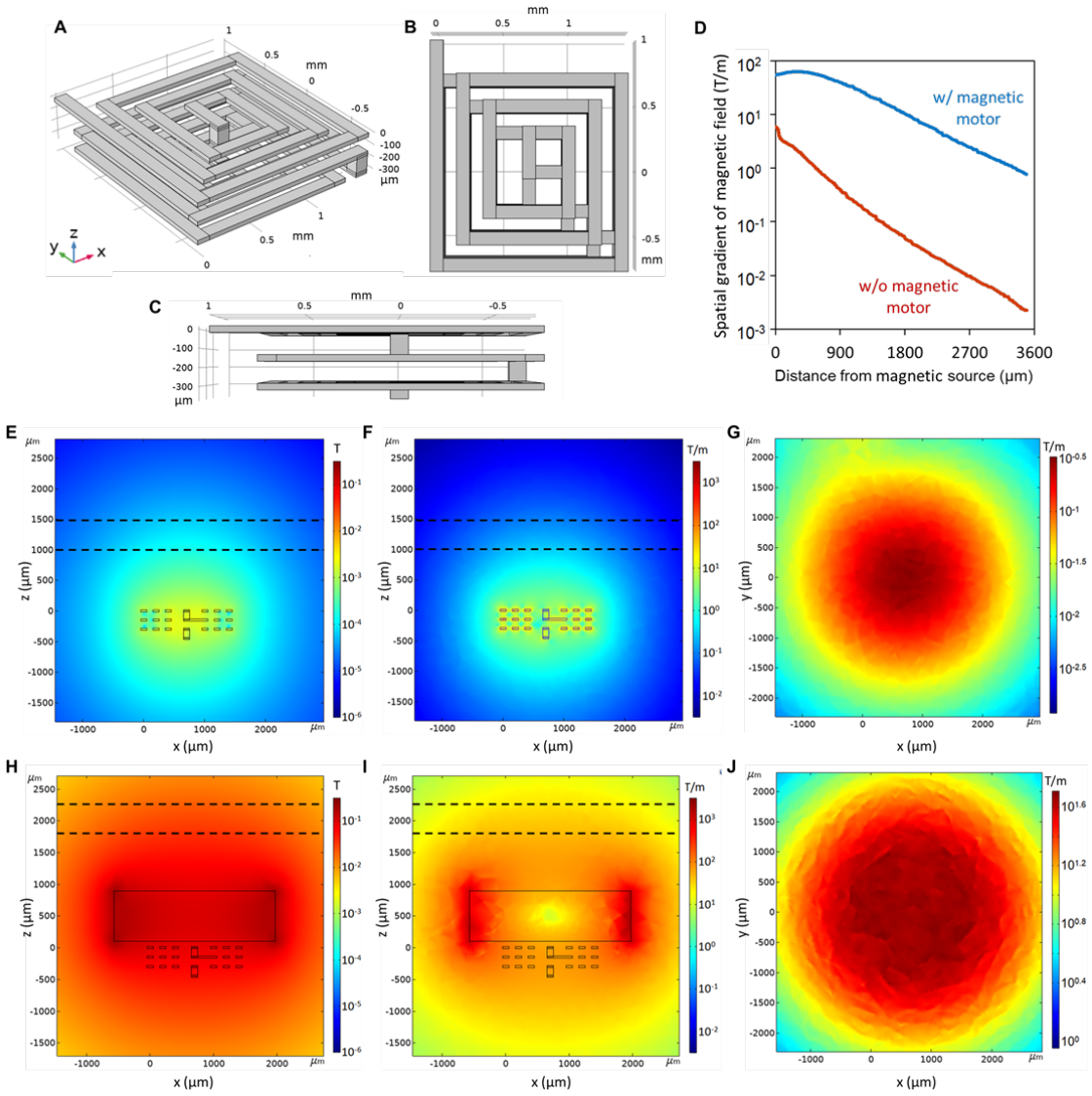

Figure 3-2 EM-coil geometry and magnetic field simulation. Oblique **(A)**, top **(B)** and side **(C)** view of the EM-coil's geometry. **(D)** COMSOL simulation results of the spatial gradient of the magnetic field with and without the magnetic motor (*i.e.*, the ferrobot). The x-axis is the distance from the magnetic source center along the z-axis. **(E,F)** magnetic field intensity (E) and spatial gradient of the magnetic field (F) in x-z plane in the absence of the ferrobot. The dashed lines outline the boundaries of the microfluidic chamber. **(G)** spatial gradient of the magnetic field in x-y plane (1 mm above the coil) in the absence of the ferrobot. **(H,I)** magnetic field intensity (H) and spatial gradient of the magnetic field (I) in x-z plane in the presence of the ferrobot. The dashed lines outline the boundaries of the microfluidic chamber. **(J)** spatial gradient of the magnetic field in the x-y plane (1 mm above the coil) in the presence of the ferrobot.

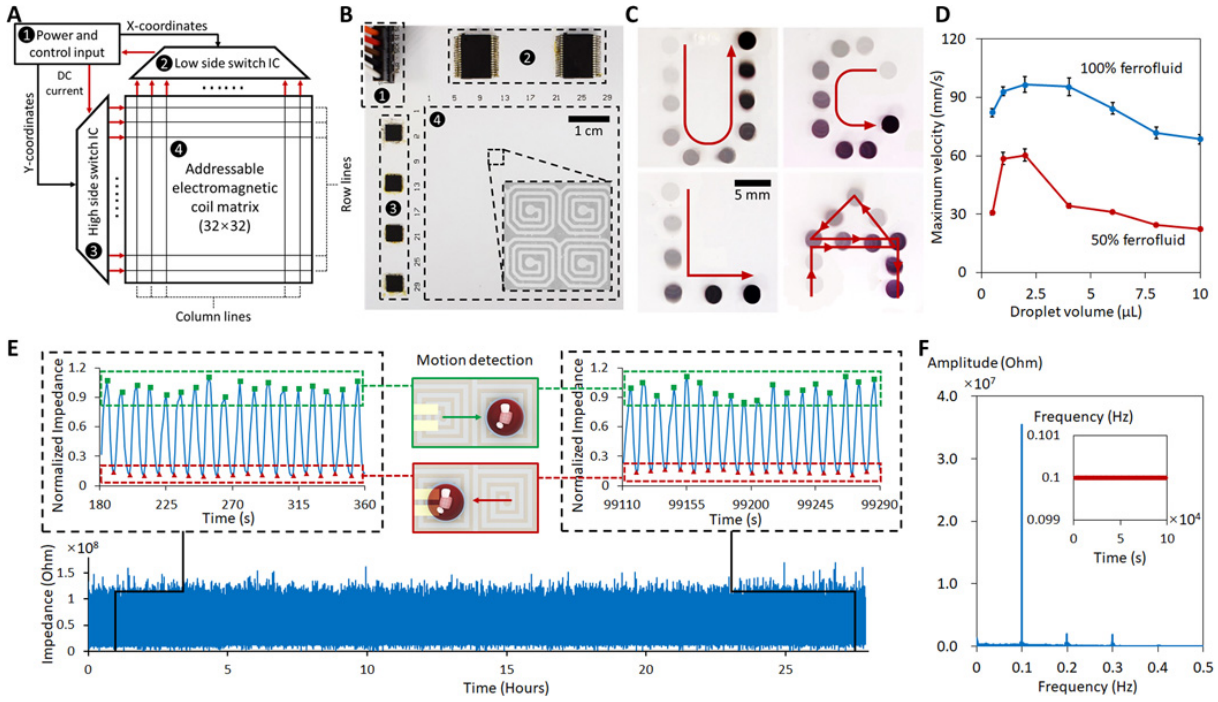

Figure 3-3 Design and characterization of the navigation floor for package transportation. **(A)** Schematic diagram of the control circuitry. **(B)** Optical image of the implemented control circuitry and the navigation floor with the close-up view of four neighboring EM coils. **(C)** Overlaid sequential images (derived from video frames) visualize the commuted path of the ferrobot (programmed with different navigation plans; the durations for commuting "U," "C," "L," and "A" paths were correspondingly 1.4, 1.4, 0.7, and 2.3 s). **(D)** Characterization of the maximum transportation velocity for two different ferrofluid concentrations. Error bars, SE (n = 3). **(E)** Characterization of the oscillatory transportation of a package with a ferrobot (sensed with an impedance sensing electrode pair) to evaluate the robustness of the ferrobotic actuation (performed for >24 hours). **(F)** FFT analysis of the oscillatory profile measured by the impedance sensing electrodes in part (E). Inset shows variation of the fundamental frequency of the 2000-s segmented time windows, depicting near-zero variation.

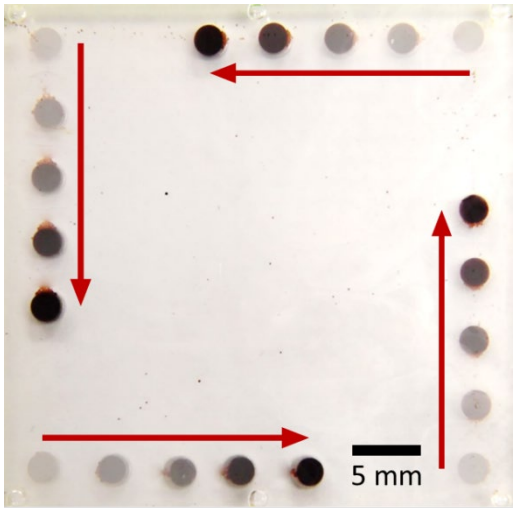

Figure 3-4 Multi-ferrobot transportation. Overlaid sequential images visualize the commuted paths of the four simultaneously commuting ferrobots (duration: 7 s).

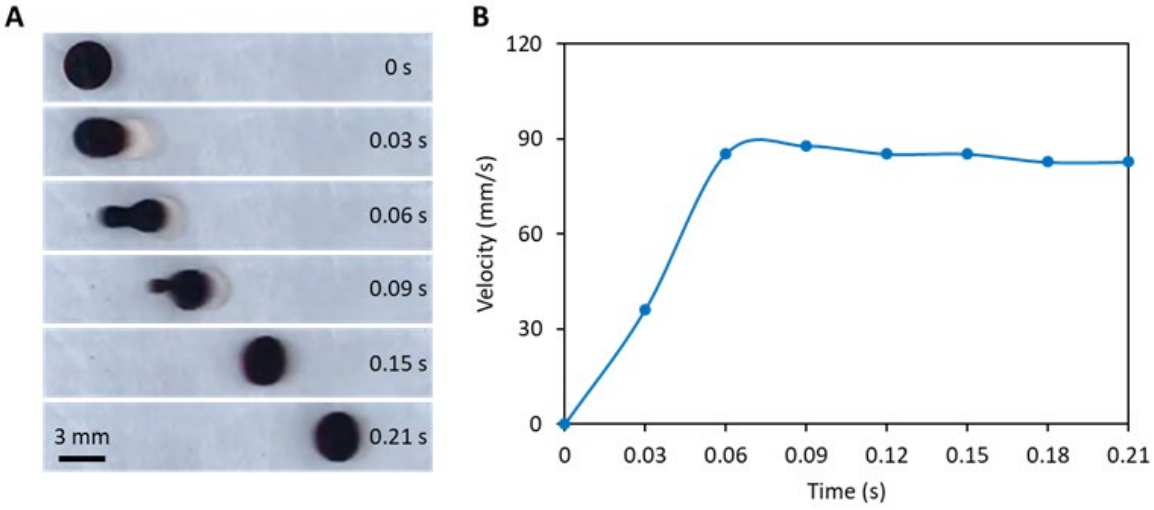

Figure 3-5 Characterization of the average velocity profile of the droplet. **(A)** Sequential imaging of a representative droplet moving along the navigation floor. **(B)** Corresponding measured averaged velocity.

The same trend was observed for a more diluted ferrofluid concentration (50% dilution by volume, also shown in Figure 3-3D). Here, the droplet volume characterization range was chosen on the basis of the envisioned microfluidic droplet applications (e.g., the MMP assay).

The contactless aspect of the actuation mechanism (i.e., no ferrobotic surface interaction with the package or the surrounding fluid) inherently renders it repeatable and durable, in contrast with contact-based EWOD actuation that is susceptible to surface degradation[16,17,25,26]. To demonstrate the durability of our ferrobotic system, we performed an illustrative continuous characterization experiment, which involved a 10,000 cycle automated oscillatory transport (frequency, 0.1 Hz) of a package over a duration of >24 hours (Figure 3-3E). Specifically, the ferrobot was programmed to automatically move in and out of contact with an impedance sensing electrode pair (fig. S4A) patterned on the substrate of a microfluidic chip. The electrodes were used to continuously track the entrance/departure of the package through monitoring the impedance signal change (correspondingly leading to an increased/decreased measured impedance, annotated in green/red, Figure 3-3E). Fast Fourier transform (FFT) analysis of the continuously recorded data (Figure 3-3F) yielded an output fundamental frequency of 0.100 Hz, which matches the input actuation frequency at the MCU level. Furthermore, the detailed FFT analysis of the 2000-s segmented time windows yielded less than 0.01% variation in the motion frequency of the package. We also performed oscillatory droplet transport experiments at 1 Hz with water- and plasma-based droplets (more than 1000 cycles). The FFT analysis, shown in Figure 3-6 (B, C,) indicates that repeatable oscillatory motions were achieved for both droplet samples. Beyond ~10 Hz, the droplet cannot be effectively manipulated because this leads to a velocity that exceeds the maximum velocity threshold.

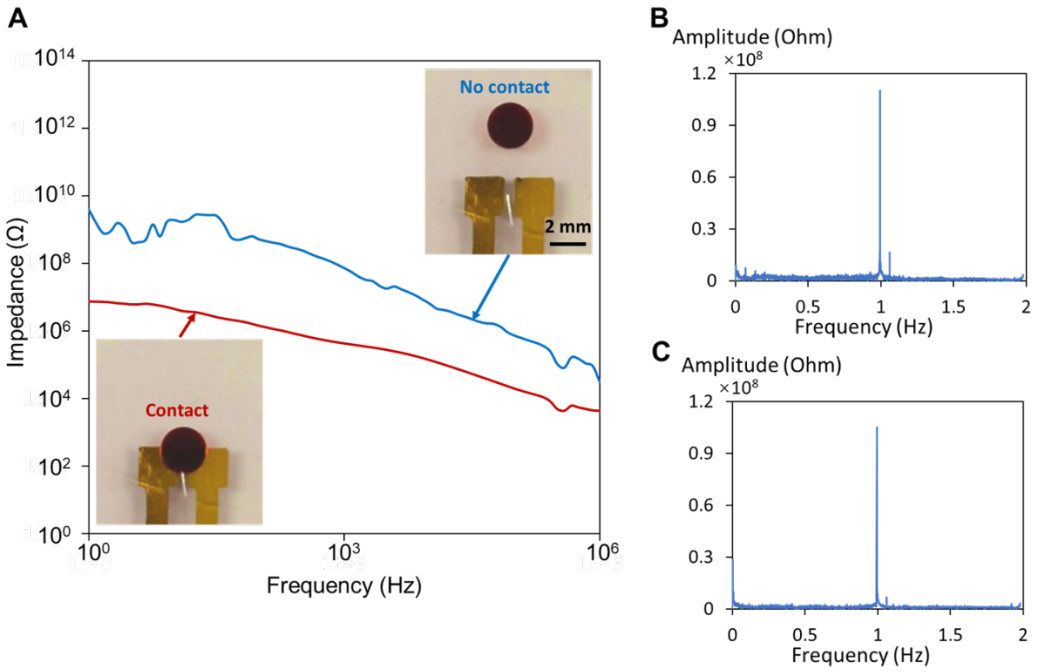

Figure 3-6 Impedance spectrum measured by the impedance sensing electrode pair. **(A)** The impedance spectrum shows distinct impedance differences when the ferrobot is present *vs*. not present (inset shows the droplet position with respect to the sensing electrodes for the corresponding measurements). **(B, C)** Corresponding FFT of the impedance measurements tracking the oscillatory motion (1 Hz, over 1000 cycles) of the droplet with compositions: (B) 50% ferrofluid (diluted in water) and (C) 50% ferrofluid (diluted in plasma).

3.3.2 Functional components for advanced operations: Droplet dispensing, generation, merging, and filtration

The high-strength and contactless aspects of the devised actuation mechanism can be exploited to conveniently interface the loaded package with different passive and active peripheral components and microfluidic structures in all three spatial dimensions, thus enabling operations of interest in a reconfigurable manner. For example, by carrying the package against a corrugated microfluidic structure formed in the x-y plane, droplet dispensing was achieved. Moreover, by delivering the droplet package within a multilayered chamber and through vertical interconnect access (VIA) and membranes along a z axis, droplet generation and filtering can be realized. Furthermore, without causing physical/field interference, droplets can be delivered to active electrofluidic interfaces to render complementary actuation mechanisms such as electrocoalescence for droplet merging.

Droplet dispensing is a precise liquid-handling capability that is useful for applications such as drug discovery, quantitative biology, and chemical analysis[27,28]. To implement the dispensing of uniformly sized droplets with the ferrobotic system, we used a microfluidic architecture with a corrugated wall structure. As demonstrated in Figure 3-7A, a "parent" droplet package was guided by a ferrobot underneath the microfluidic chip. When it was transported along the corrugated structure, smaller "child" droplets were dispensed. As shown in Figure 3-7B, the parent droplet started moving along the corrugated wall at t = 0 s. After the droplet passed the corrugated structure at t = 1 s due to geometric pinching, a small volume of the droplet broke away from the parent and entered the structure. The corrugated structure can be extended into an array format to dispense multiple droplets. As shown in the final step of Figure 3-7B, three homogenous droplets (1.63 ± 0.09 μl) were dispensed.

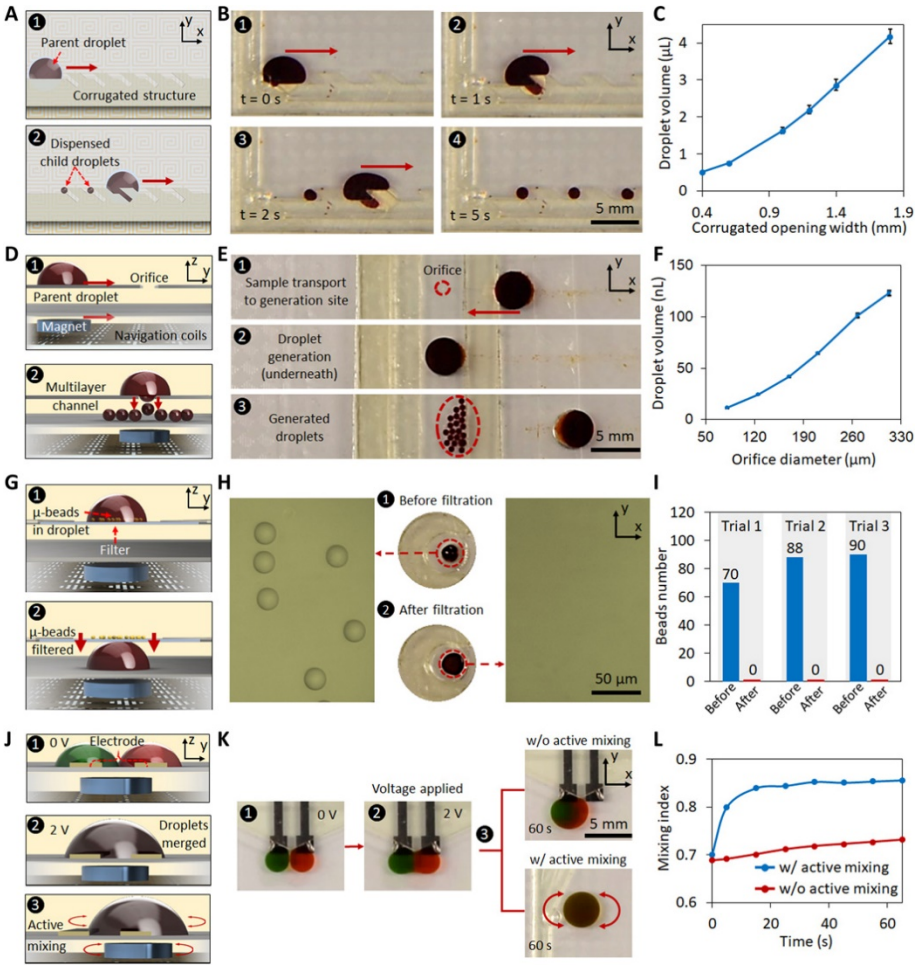

Figure 3-7 Demonstration and characterization of advanced operations achieved with functional components. **(A)** Schematic illustration of the droplet dispensing mechanism involving the transportation of the package against a corrugated microfluidic wall. **(B)** Sequential optical images of the droplet dispensing process. **(C)** Characterization of the dispensed droplets' size for different corrugated opening widths. Error bars, SE (n = 10). **(D)** Schematic illustration of the droplet generation process involving the droplet transportation to a VIA-like orifice. **(E)** Sequential optical images of the droplet generation process. **(F)** Characterization of the generated droplets' volume for different orifice diameters. Error bars, SE (n = 20). **(G)** Schematic illustration of the filtration mechanism. **(H)** Optical image of the solution sample before and after filtration. **(I)** Bead counts before and after filtration (three trials). **(J)** Schematic illustration of droplet merging and mixing mechanisms. **(K)** Optical images to visualize the droplet merging (upon applying 2 V) and mixing process (with and without active mixing). **(L)** Comparison of the progressive mixing index for the two cases of with and without active mixing.

To study the level of control that our system has on the dispensed droplet sizes, we designed and tested various corrugated-opening widths. The results show that by increasing the corrugated-opening width, the dispensed droplet volume could be modulated from 0.5 to 4 μl (Figure 3-7C). The same trend was observed for diluted ferrofluid concentrations (10 and 50% dilutions by volume; Figure 3-8). If larger dispensed droplet volumes are needed, then a larger magnet in addition to an enlarged corrugated-opening width may be required.

Furthermore, higher throughput and smaller volume droplet generation can be realized by incorporating an orifice-like VIA connecting neighboring layers in a multilayer microfluidic architecture. As schematically illustrated in Figure 3-7D, when the parent droplet is guided through the upper layer to the top of the orifice, it is attracted toward the lower layer by the vertically exerted magnetic force from the ferrobot. Every time a critical volume of the droplet passes the orifice, it breaks off into a child droplet. As shown in Figure 3-7E, the following sequential events occur: (i) the transport of the parent droplet (in the upper layer) to an orifice; (ii) the positioning of the parent droplet on the orifice to generate child droplets; and (iii) the departure of the parent droplet, leaving behind the generated child droplets (in the lower layer). By adjusting the width of the junction orifice, the droplet volume (~10 to 125 nl) and the generation rate can be tuned (Figure 3-7F and 3-9). Such nanoliter-generated droplets can also be further manipulated by the ferrobot (Figure 3-10).

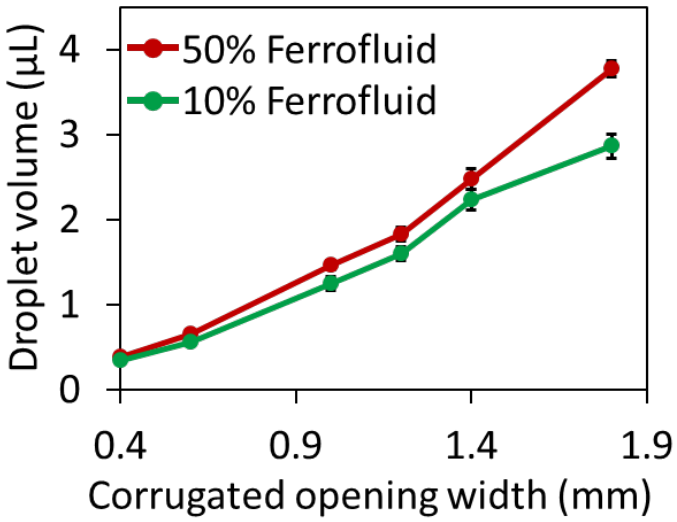

Figure 3-8 Dispensed droplet characterization. Characterization of the dispensed droplets' size for different corrugated opening widths and using two ferrofluid concentrations. Error bars indicate standard error (n = 10).

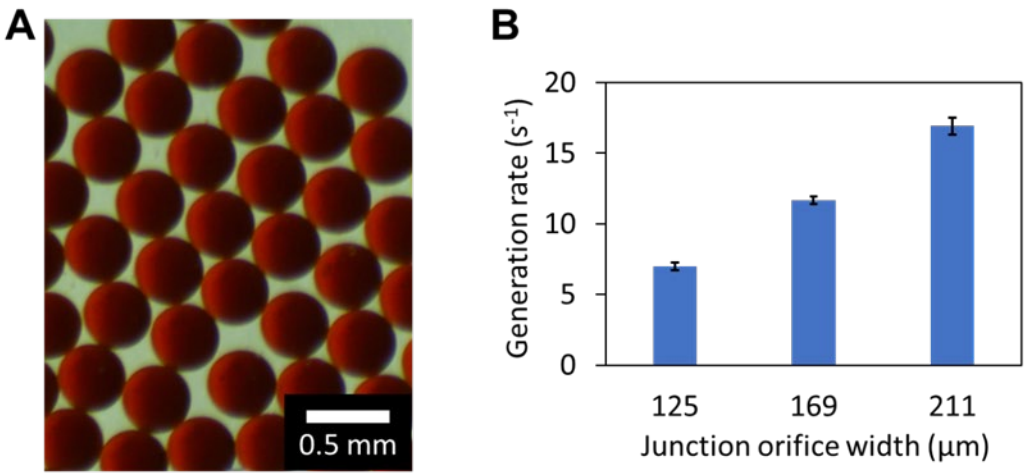

Figure 3-9 Droplet generation characterization. (**A**) Optical microscopic images of generated droplets using 169 µm-diameter orifice (**B**) Characterization of droplet generation rate for varying orifice diameters (based on counting the generated droplets over 4 s).

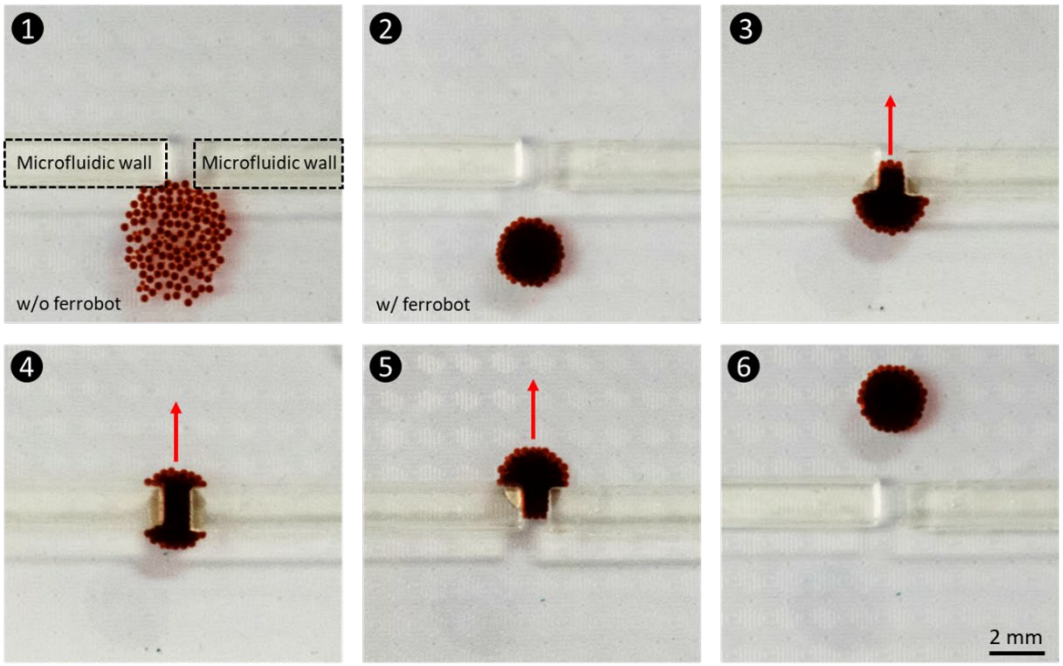

Figure 3-10 Collective transportation of nL-droplets by a ferrobot. Sequential imaging indicates the collection and transportation of generated nL-droplets by a ferrobot through a 2 mm-wide × 1mm-long pore.

Microfluidic filtration is one of the key sample processing procedures required for applications such as cell separation[29,30]. Here, by incorporating a membrane between the two layers of the microfluidic device, size-based filtration was realized. As schematically shown in Figure 3-7G, the contactless magnetic force exerted by the ferrobot causes the droplet to be pulled through the filter to the lower layer, leaving behind particles that are too large to pass through. Specifically, here, a membrane with a size cutoff of 10 μm was used to filter out μ-beads with a diameter of 25 μm. To quantify the filtration capability, we optically imaged the ferrofluid droplet before and after the filtration procedure. As can be seen from Figure 3-7H, 25-μm μ-beads can be observed in the droplet before filtration and are subsequently filtered out, as evident from the postfiltration optical analysis results (three trials; Figure 3-7I).

Droplet merging allows for timed and metered addition of reagents and can play a critical role in performing droplet-based biological assays that aim to measure DNA/RNA, protein, and cell properties in samples[31-35]. Here, to achieve the merging of droplets in the ferrobotic system, we leveraged electrocoalescence as a complementary actuation mechanism, which is noninterfering with the contactless ferrobotic actuation (Figure 3-7J). Accordingly, electrocoalescence is realized by applying 2 V across a pair of gold electrodes (2 mm by 2 mm, spaced 1 mm apart, patterned on the substrate of the microfluidic device). Figure 3-7K show that upon applying 2 V, two droplets delivered in the vicinity of the electrodes coalesce. To achieve homogeneous and evenly distributed droplet contents after merging, chaotic fluid motion within the merged droplet can be induced by actuating neighboring EM coils with a frequency of 10 Hz in a cyclic fashion, resulting in an oscillatory motion of the ferrobot within the confines of the coil's coordinates. This cyclic motion creates folding flows in alternating directions to effectively render mixing. Figure 3-7K

visually demonstrates the substantial effect of the devised active mixing on shortening the time required to achieve homogeneity in a merged droplet. To quantify this effect, we performed optical analysis on the merged red/green droplet by defining a mixing index. The results are illustrated in Figure 3-7L, demonstrating that a near-homogenous profile is achieved within ~15 s using active mixing, which is substantially shorter than without active mixing.

3.3.3 Efficient achievement of objectives with a cross-collaborative network of ferrobots

The robustness and addressability of the ferrobotic system can be leveraged to deploy fleets of ferrobots to dynamically accomplish collaborative tasks in parallel toward the more efficient achievement of a common objective. Here, as an example, a package-sorting mission is assigned to the ferrobotic system, where the objective is to sort randomly sequenced packages into a sorted sequence of increasing droplet volumes. Figure 3-11A illustrates the system-level view of the sorting procedure, which includes (i) loading of multiple packages of various sizes into the ferrobotic system with random relative positions; (ii) top-view image acquisition of the packages on the navigation floor to identify the package sizes and positions; (iii) computationally deriving the navigation plan to formulate the detailed tasks for the ferrobots in accordance to the "merge sort" algorithm[36] and the acquired size and position information; and (iv) communicating the corresponding assigned tasks for each of the ferrobots with the aid of the on-board microcontroller to achieve the overarching sorting objective. To particularly demonstrate the degree of efficiency that can be attained when deploying a cross-collaborative network of ferrobots, we compared the n-package sorting performance achieved by a team of n ferrobots against that achieved by a single ferrobot on the basis of the completion time (as detailed in Figure 3-11B, C, for an illustrative case of n = 8).

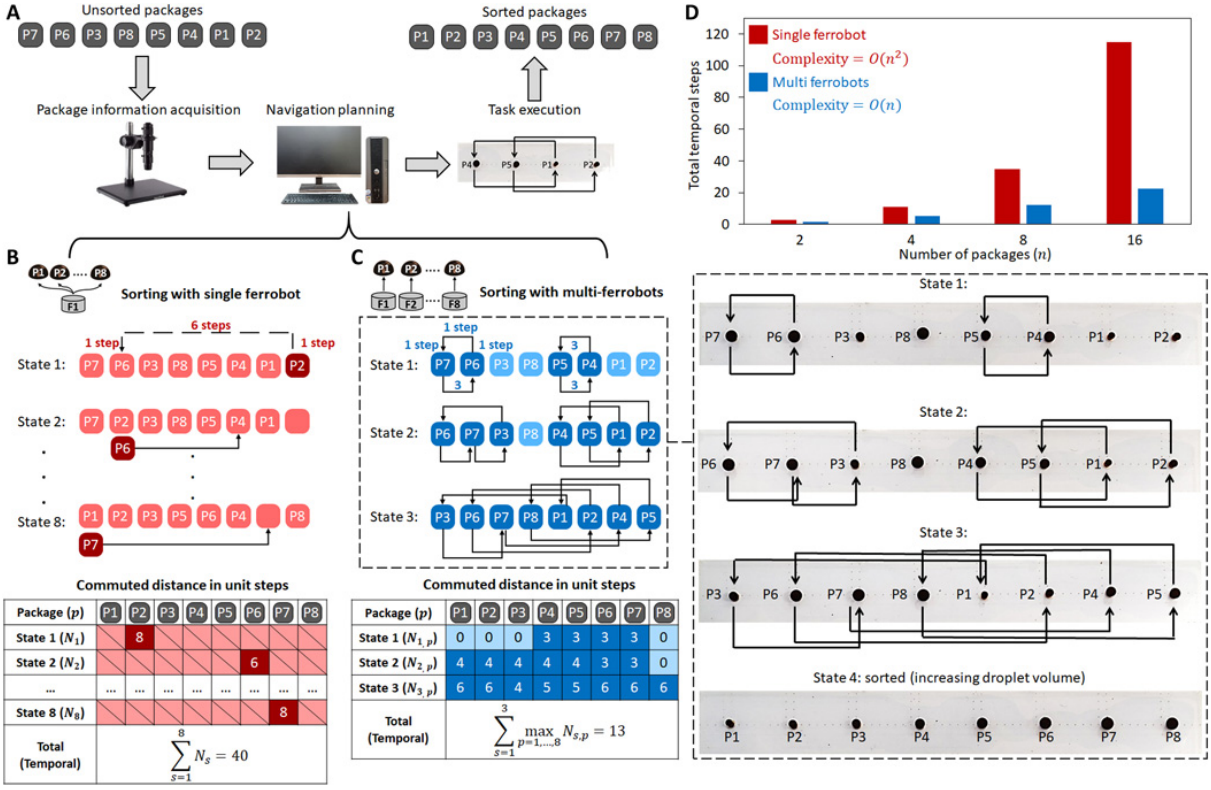

Figure 3-11 Efficient package sorting with a cross-collaborative network of ferrobots. **(A)** System-level view of the sorting procedure. **(B, C)** Comparison of the sorting efficiency achieved by (B) a single ferrobot and (C) eight ferrobots tasked with sorting a random sequence of eight packages. State-by-state transitions for both scenarios are illustrated, and the left table details the commuted distance of each ferrobot. The snapshots from the sorting experiment performed with eight ferrobots are shown on the right (captured at the end of each state). **(D)** The total temporal unit steps required for sorting 2, 4, 8, and 16 packages (based on statistical averaging of all the possible permutations).

When only one ferrobot is used for sorting, it is responsible for the delivery of all the packages by itself. At each state (defined as the period during which the available ferrobot starts and finishes one round of package delivery), only one package can be moved to its target location. To quantitatively characterize the sorting efficiency, we defined a "unit step," which equals to the distance between two navigation coils, to measure the distance that the ferrobots will move. For example, referring to Figure 3-11B, at state 1, the ferrobot moves eight unit steps (two vertical steps and six horizontal steps) to deliver package 2 ("P2") from position 8 to position 2. Because only one ferrobot is performing the task, the "temporal steps" (number of steps, which determine the maximum time elapsed over the course of a state) required to complete sorting are equal to the total unit steps moved by the single ferrobot. In the example shown, it takes the single ferrobot a total of 40 temporal steps to meet the sorting objective.

When multiple ferrobots are deployed (Figuer 3-11C), each ferrobot is charged with moving one package, and they can move in parallel with other ferrobots during the same state (following the computationally derived navigation plan in accordance with the "merge sort" algorithm; Figure 3-12A). The corresponding experiment is visualized in Figure 3-11C (right). In this scenario, the number of temporal steps for each state is determined by the maximum steps taken by a ferrobot within the team because the ferrobots are delivering packages in parallel. For example, referring to Figure 3-11C, in state 2, among eight ferrobots, one ferrobot moves zero steps, two ferrobots move three steps, and five ferrobots move four steps, yielding four temporal steps for that state. The total number of temporal steps to achieve the sorting objective is also equal to the sum of temporal steps for each state, which is 13 for the illustrated example.

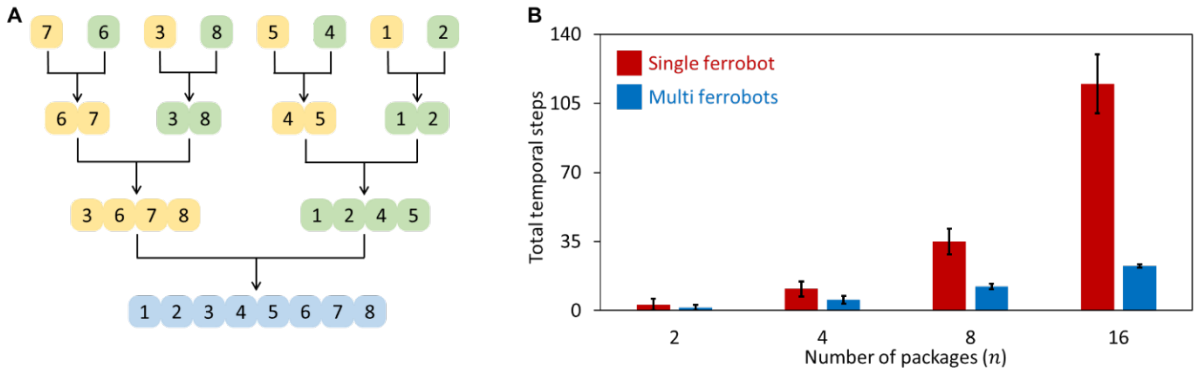

Figure 3-12 Merge sort algorithm and sorting performance for single *vs*. multi ferrobots. **(A)** Representative schematic of the application of recursive merge sort algorithm to sort an array of 8 integers. (**B**) The averaged total temporal unit steps required for sorting $n = 2$, 4, 8, and 16 packages, performed with a single or n ferrobots (simulated based on 10,000 randomly generated sequence of packages for each scenario, error bars indicate standard deviation).

By comparison, for this illustrative example, sorting using multiple ferrobots results in about 300% increased efficiency as compared with the single ferrobot case. This degree of improvement achieved due to the deployment of a cross-collaborative network of ferrobots will be even higher for the cases requiring sorting of a larger number of packages (i.e., larger n). That is because the complexity of the mission at hand for the case of a single ferrobot increases as O(n2), whereas for the case of multiple ferrobots, it increases linearly [i.e., O(n)]. To reinforce this point, as shown in Figure 3-11D, we derived the total temporal unit steps for the cases of n = 2, 4, 8, and 16, based on statistical averaging of all the possible permutations (consistent with the trend observed when simulating 10,000 randomly generated sequences of n packages; Figure 3-12B). Together, the results presented within the framework of this generalizable objective illustrate the utility of the deployment of a network of ferrobots to achieve the objective at hand efficiently and the suitability of the ferrobotic system for microfluidic logistics.

3.3.4 Application of the ferrobotic system to implement a pipelined and automated bioassay

Leveraging the demonstrated capability of the ferrobotic system to deliver advanced and cross-collaborative operations, we implemented a pipelined and automated bioassay equipped with a dynamic self-calibration mechanism as an example utility of the presented technology in diverse application spaces centering on microfluidic logistics. Accordingly, the ferrobotic logistics were adapted to quantify MMP concentrations in human plasma. MMPs are biomarkers extensively studied and reported as immunological indicators, wherein the elevation of plasma MMP concentration is associated with physiological and pathological processes such as cancer metastasis[22,23,37], sepsis onset[38-40], immune activation[24,41], and wound healing[42,43].

Figure 3-13A illustrates the workflow of the MMP assay, which is based on the fluorescent quantification of the enzymatic activity of MMPs from a test sample (introduced into the input well) and the calibrator samples indicated by the intensity of fluorescent signals. To realize an automatic self-calibration mechanism, we used preloaded source samples (introduced at the source well array, with known concentrations of the MMP collagenase) for the construction of calibrator samples in situ, providing optional flexibility to dynamically construct new calibrator concentrations (e.g., [C2] in Figure 3-13A). To facilitate optical readout, we preloaded a fluorescence resonance energy transfer (FRET)-based MMP substrate in the calibration well array and the output well (designated for test sample analysis). The self-calibration capability of the assay establishes a standard curve in situ and concurrently with the testing assay, which is particularly useful for mitigating systematic error typically associated with fluorescence spectrometry and ensuring the accuracy of the measurements[44].

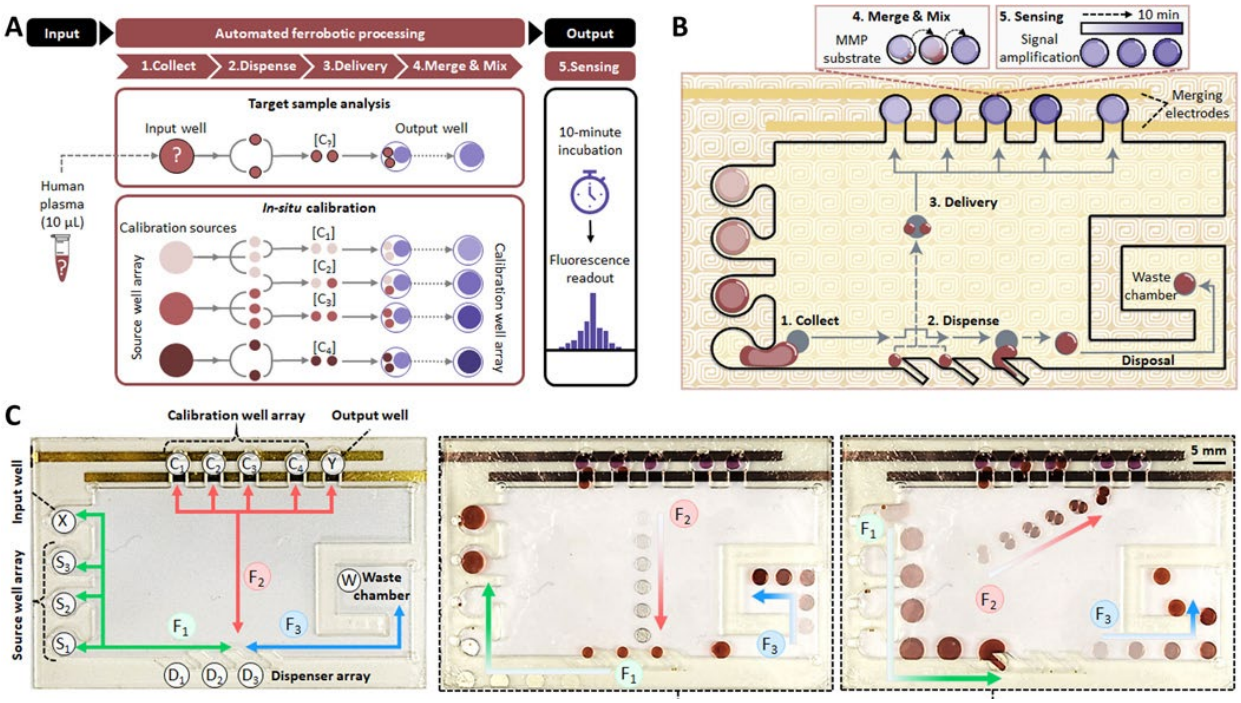

Figure 3-13 Pipelined and automated MMP assay performed by the ferrobotic system. **(A)** General workflow of the MMP assay equipped with a dynamic self-calibration mechanism. **(B)** Illustration of the ferrobotic tasks in relation to the navigation floor over the processing of a representative sample (performed by three ferrobots). **(C)** Overview of the navigation plans of the three deployed ferrobots (F_1, F_2, and F_3) with annotated locations of interest.

The ferrobotic system was programmed to implement the steps of the automated assay within a microfluidic architecture, including (i) sample collection, (ii) dispensing (to ensure uniform sample volume), (iii) delivery, and (iv) merging (with the aid of an electrocoalescence electrode pair) and mixing for sensing (Figure 3-13B). Specifically, three ferrobots (F1, F2, and F3) were used to carry out the required tasks in a pipelined manner. The overview of the navigation plans of the three ferrobots is shown in Fig. 5C. In this regard, ferrobot F1 is in charge of collecting and dispensing the source and test samples into smaller uniform droplets. Ferrobot F2 is responsible for delivering the dispensed droplets to the designated detection wells, and ferrobot F3 is tasked with removing the dispensed droplet residues to the waste chamber. The detailed timeline of the task sequence executed by each ferrobot in coordination with the other two ferrobots, along with representative snapshots of the navigation floor status, are illustrated in Figure 3-13C, 3-14D.

Upon delivering the dispensed calibrator/test sample droplets to the calibration well array/output well, the electrocoalescence electrode pair (a single pair patterned across all the detection wells) is activated, merging the delivered droplets with the preloaded MMP substrate within each well all at once. To achieve a homogenous mixture after merging, ferrobot F2 can induce a chaotic internal flow. Upon merging and mixing of the samples with MMP substrate, enzymatic reactions (Figure 3-14E) effectively commence at the same time, resulting in the generation of fluorescent signal proportional to the respective MMP content in a well. The fluorescent signals are quantitively analyzed by fluorescence microscopy. The linearity of the fluorescent signals with the MMP content of a sample was validated by spiking collagenase in a phosphate-buffered saline (PBS) buffer at different levels and reading out fluorescence after a 10-min incubation (Figure 3-15).

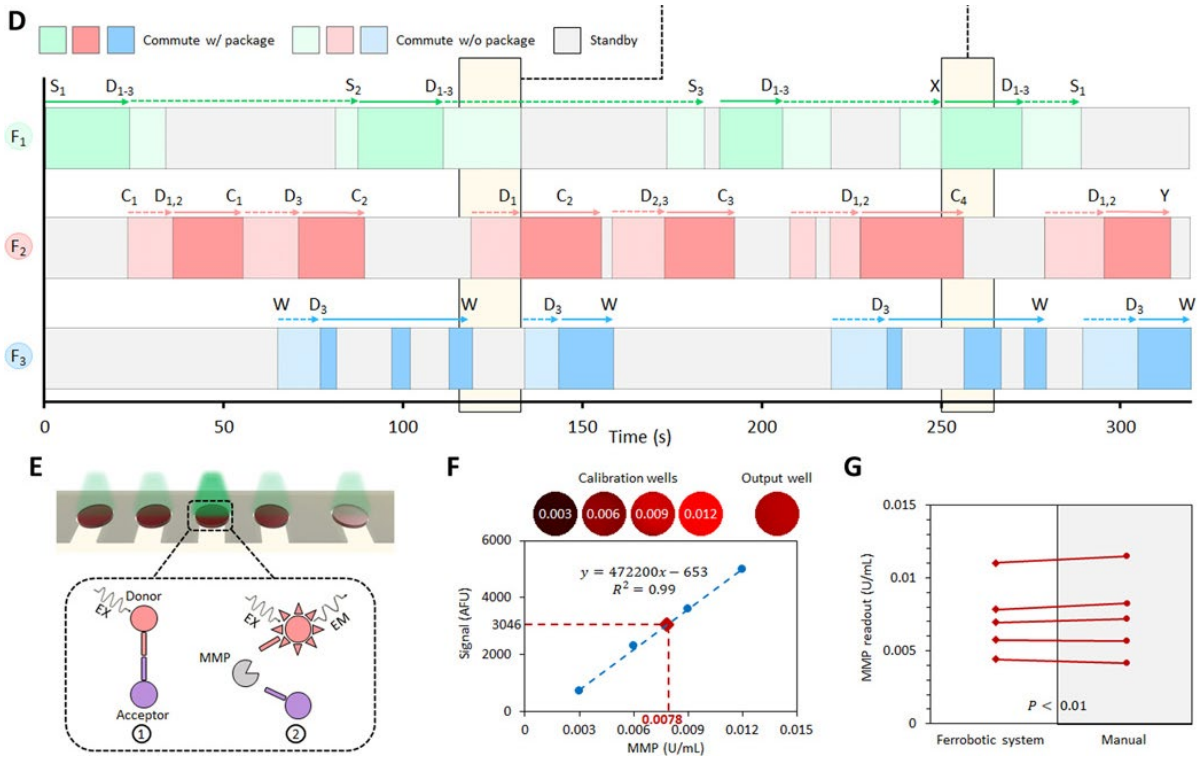

Figure 3-14 Pipelined and automated MMP assay performed by the ferrobotic system (cont'd). **(D)** The detailed timeline of the ferrobots' status (commuting with/without package, standby), with annotated locations of interest. Overlaid sequential video frames illustrating the status at two representative stages. **(E)** Illustration of the FRET pair from the MMP substrate cleaved by the MMPs present in the sample to yield a fluorescent product that is no longer quenched. **(F)** The fluorescent readouts [arbitrary fluorescence unit (AFU)] from the calibration and output wells after automated ferrobotic processing and 10 min of incubation. The concentration of MMP in the test sample is estimated with the aid of a real-time calibration standard curve generated from the four calibrator samples [0.0078 U/ml (estimated) versus 0.008 U/ml (expected)]. **(G)** Estimated MMP concentrations in five tested human plasma samples (performed by the ferrobotic system and manually by a technician; $P < 0.01$).

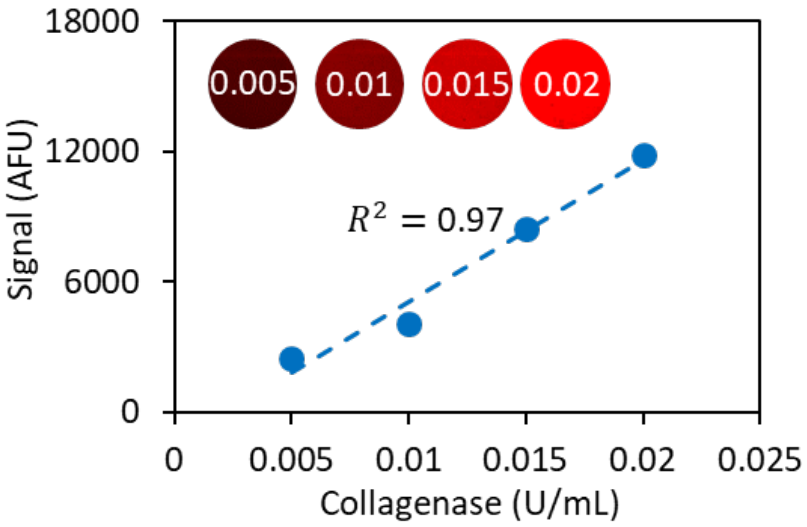

Figure 3-15 Characterization of the MMP assay. The recorded fluorescence signals from the calibration well array, where each well contains PBS dilutions of collagenase at different end concentrations.

To evaluate the analytical accuracy of the ferrobotic assay for measuring the MMP content in human plasma, we used four calibrator samples with collagenase concentrations of 0.003, 0.006, 0.009, or 0.012 Wünsch U/ml to determine the MMP concentration of a test sample (human plasma spiked with MMP at a collagenase concentration of 0.008 U/ml). As illustrated in Figure 3-14F, by referring to the real-time standard curve generated by the calibrator samples, the test sample MMP content was measured to be 0.0078 ± 0.0005 U/ml (based on 95% confidence interval). To further evaluate the analytical performance of the ferrobotic assay, we analyzed four additional test samples by the ferrobotic system and by a technician using manual pipetting steps and a plate reader[45]. As shown in Figure 3-14G, the readouts obtained from the ferrobotic system closely matched those analyzed using standard manual analysis ($P < 0.01$), which, in turn, illustrates the successful execution of all ferrobotic instructions with a high degree of robustness and precision. This pipelined assay exemplifies the capacity of the ferrobotic system to perform highly quantitative biochemical processes with a high level of integration and automation.

3.4 Discussion

Inspired by the degrees of freedom achieved by the emergence of AGV robotic systems in terms of mobility and automation, here we introduced and experimentally demonstrated the concept of a ferrobotic system. Accordingly, an amplified addressable EM actuation mechanism is devised for robotic guidance. The contactless (i.e., no ferrobotic contact with the package or the surrounding fluid) and high-strength actuation mechanism inherently renders it rapid (10 cm/s), repeatable (>10,000 cycles), and robust (>24 hours). These traits, together with the reconfigurability of the system, enabled the implementation of advanced and diverse operations through the integration of passive and active functional components. To this end, we designed and

characterized droplet microfluidic operations—including dispensing, generation, merging, and filtering—where the results indicated minimal undesired operational performance deviation. Furthermore, we demonstrated the significantly elevated efficiency of the ferrobotic system for microfluidic logistics applications by deploying a network of cross-collaborative ferrobots to deliver an illustrative and generalizable package sorting objective. To showcase an application where logistics of sample dosing, merging, and mixing are required, we leveraged the advanced and cross-collaborative ferrobotic operations to achieve a pipelined and automated bioassay for the quantification of MMPs in human plasma.

Collectively, our characterization results demonstrate precise, repeatable, durable, and cross-collaborative ferrobotic operations in versatile settings. Although these operations were realized with a 32-by-32 addressable navigation floor, the scale of the ferrobotic operations can be expanded by simply adopting a larger navigation floor (requiring minimal reconfiguration of the PCB, specifically, increasing the number of EM coils). In that regard, augmentation with image or electrical ferrobot/droplet positioning sensing capabilities within the ferrobotic system will allow for the implementation of a feedback control process as a corrective measure to ensure the robustness of desired large-scale operations. Furthermore, the optical readout of the assay is currently performed using a benchtop fluorescence microscope. Further automation and integrated sample-to-answer solutions, especially in point-of-care settings, would benefit from integrated low-cost readers leveraging consumer electronic devices[46]. Alternatively, other assays could be read using electrochemical sensors, which can be integrated onto the platform in a similar manner as the electrodes used for electrocoalescence. Exploiting the ferrofluid biocompatibility[47,48],

fluorescence and electrochemical assays can be adapted for applications centering on cell and nucleic acid analysis[49].

On a broader level, adaptation of the ferrobotic system for translational applications necessitates future and convergent designated efforts in microscopic and macroscopic domains toward establishing a generalizable design space for the ferrobotic system. Microfluidic physics-focused efforts are required to comprehensively model the underlying ferrobotic actuation mechanism and understand its limitations in relation to relevant forces, scaling of dimensions (including magnet-, droplet-, and microfluidic structure dimensions), fluidic properties, and other design parameters. Furthermore, macroscopically, dynamic navigation planning algorithms are required to optimize the performance of the cross-collaborative ferrobots toward the delivery of the required objective(s) and in the presence of operational constraints (such as a ferrobotic "safety distance"). To this end, readily developed models from the AGV community aiming to address issues such as layout challenges, fleet management, speed/movement limitations, and optimization functions can be adapted and applied within the framework of the ferrobotic system.

The versatility, scalability, and reconfigurability of the devised ferrobotic system allow for its adaptation to perform diverse and massively parallelized and sequential microfluidic operations relevant to diverse application spaces. By capitalizing on the high degree of automation that can be achieved by the presented technology, large datasets can be generated to unravel complex biological and chemical processes, seeding the transformation of the biotechnology industries and mirroring the impact of the AGV robotic systems on their respective industries.

3.5 References

1. How robots change the world. *Economic Outlook*. **43** (2019), pp. 5–8.
2. J.-T. Li, Design Optimization of Amazon Robotics. *Automation, Control and Intelligent Systems*. **4** (2016), p. 48.
3. A. H. C. Ng, R. Fobel, C. Fobel, J. Lamanna, D. G. Rackus, A. Summers, C. Dixon, M. D. M. Dryden, C. Lam, M. Ho, N. S. Mufti, V. Lee, M. A. M. Asri, E. A. Sykes, M. D. Chamberlain, R. Joseph, M. Ope, H. M. Scobie, A. Knipes, P. A. Rota, N. Marano, P. M. Chege, M. Njuguna, R. Nzunza, N. Kisangau, J. Kiogora, M. Karuingi, J. W. Burton, P. Borus, E. Lam, A. R. Wheeler, A digital microfluidic system for serological immunoassays in remote settings. *Sci. Transl. Med*. **10** (2018).
4. V. Srinivasan, V. K. Pamula, R. B. Fair, An integrated digital microfluidic lab-on-a-chip for clinical diagnostics on human physiological fluids. *Lab Chip*. **4**, 310–315 (2004).
5. A. H. C. Ng, M. D. Chamberlain, H. Situ, V. Lee, A. R. Wheeler, Digital microfluidic immunocytochemistry in single cells. *Nat. Commun*. **6**, 7513 (2015).
6. A. R. Wheeler, H. Moon, C. A. Bird, R. R. O. Loo, C.-J. C. J. Kim, J. A. Loo, R. L. Garrell, Digital microfluidics with in-line sample purification for proteomics analyses with MALDI-MS. *Anal. Chem*. **77**, 534–540 (2005).
7. A. Stark, D. J. Shin, T.-H. Wang, A sample-to-answer droplet magnetofluidic assay platform for quantitative methylation-specific PCR. *Biomed. Microdevices*. **20**, 31 (2018).
8. B. Wu, S. von der Ecken, I. Swyer, C. Li, A. Jenne, F. Vincent, D. Schmidig, T. Kuehn, A. Beck, F. Busse, H. Stronks, R. Soong, A. R. Wheeler, A. Simpson, Rapid Chemical Reaction Monitoring by Digital Microfluidics-NMR: Proof of Principle Towards an

Automated Synthetic Discovery Platform. *Angewandte Chemie International Edition*. **58** (2019), pp. 15372–15376.

9. H. Ding, S. Sadeghi, G. J. Shah, S. Chen, P. Y. Keng, C.-J. C. J. Kim, R. M. van Dam, Accurate dispensing of volatile reagents on demand for chemical reactions in EWOD chips. *Lab Chip*. **12**, 3331–3340 (2012).
10. M. Antfolk, T. Laurell, Continuous flow microfluidic separation and processing of rare cells and bioparticles found in blood – A review. *Analytica Chimica Acta*. **965** (2017), pp. 9–35.
11. M. Karle, S. K. Vashist, R. Zengerle, F. von Stetten, Microfluidic solutions enabling continuous processing and monitoring of biological samples: A review. *Anal. Chim. Acta.* **929**, 1–22 (2016).
12. D. Di Carlo, D. Irimia, R. G. Tompkins, M. Toner, Continuous inertial focusing, ordering, and separation of particles in microchannels. *Proc. Natl. Acad. Sci. U. S. A*. **104**, 18892–18897 (2007).
13. M. Abdelgawad, A. R. Wheeler, The Digital Revolution: A New Paradigm for Microfluidics. *Advanced Materials*. **21** (2009), pp. 920–925.
14. M. G. Pollack, R. B. Fair, A. D. Shenderov, Electrowetting-based actuation of liquid droplets for microfluidic applications. Applied Physics Letters. 77 (2000), pp. 1725–1726.
15. K. Choi, A. H. C. Ng, R. Fobel, A. R. Wheeler, Digital Microfluidics. *Annual Review of Analytical Chemistry*. **5** (2012), pp. 413–440.
16. M. Mibus, G. Zangari, Performance and Reliability of Electrowetting-on-Dielectric (EWOD) Systems Based on Tantalum Oxide. *ACS Applied Materials & Interfaces*. **9** (2017), pp. 42278–42286.

17. Y. Zhang, N.-T. Nguyen, Magnetic digital microfluidics - a review. *Lab Chip*. **17**, 994–1008 (2017).

18. J. Pipper, Y. Zhang, P. Neuzil, T.-M. Hsieh, Clockwork PCR including sample preparation. *Angew. Chem. Int. Ed Engl*. **47**, 3900–3904 (2008).

19. W. H. Koh, K. S. Lok, N.-T. Nguyen, A Digital Micro Magnetofluidic Platform For Lab-on-a-Chip Applications. *Journal of Fluids Engineering*. **135** (2013).

20. U. Lehmann, C. Vandevyver, V. K. Parashar, M. A. M. Gijs, Droplet-Based DNA Purification in a Magnetic Lab-on-a-Chip. *Angewandte Chemie International Edition*. **45** (2006), pp. 3062–3067.

21. C.-H. Chiou, D. J. Shin, Y. Zhang, T.-H. Wang, Topography-assisted electromagnetic platform for blood-to-PCR in a droplet. *Biosensors and Bioelectronics*. **50** (2013), pp. 91–99.

22. M. Egeblad, Z. Werb, New functions for the matrix metalloproteinases in cancer progression. *Nature Reviews Cancer*. **2** (2002), pp. 161–174.

23. L. Sevenich, J. A. Joyce, Pericellular proteolysis in cancer. *Genes & Development*. **28** (2014), pp. 2331–2347.

24. W. C. Parks, C. L. Wilson, Y. S. López-Boado, Matrix metalloproteinases as modulators of inflammation and innate immunity. *Nat. Rev. Immunol*. **4**, 617–629 (2004).

25. I. Swyer, R. Fobel, A. R. Wheeler, Velocity Saturation in Digital Microfluidics. *Langmuir*. **35**, 5342–5352 (2019).

26. J. Li, N. S. Ha, T. Liu, R. M. van Dam, C. J. Kim, Ionic-surfactant-mediated electro-dewetting for digital microfluidics. *Nature*. **572**, 507–510 (2019).

27. S. Kahkeshani, J. E. Kong, Q. Wei, D. Tseng, O. B. Garner, A. Ozcan, D. Di Carlo, Ferrodrop Dose-Optimized Digital Quantification of Biomolecules in Low-Volume Samples. *Anal. Chem*. **90**, 8881–8888 (2018).

28. S. Kahkeshani, D. Di Carlo, Drop formation using ferrofluids driven magnetically in a step emulsification device. *Lab Chip*. **16** (2016), pp. 2474–2480.

29. Y. Cheng, X. Ye, Z. Ma, S. Xie, W. Wang, High-throughput and clogging-free microfluidic filtration platform for on-chip cell separation from undiluted whole blood. *Biomicrofluidics*. **10**, 014118 (2016).

30. X. Qiu, J. A. Lombardo, T. M. Westerhof, M. Pennell, A. Ng, H. Alshetaiwi, B. M. Luna, E. L. Nelson, K. Kessenbrock, E. E. Hui, J. B. Haun, Microfluidic filter device with nylon mesh membranes efficiently dissociates cell aggregates and digested tissue into single cells. *Lab Chip*. **18**, 2776–2786 (2018).

31. B. Bhattacharjee, S. A. Vanapalli, Electrocoalescence based serial dilution of microfluidic droplets. *Biomicrofluidics*. **8**, 044111 (2014).

32. R. Tewhey, J. B. Warner, M. Nakano, B. Libby, M. Medkova, P. H. David, S. K. Kotsopoulos, M. L. Samuels, J. B. Hutchison, J. W. Larson, E. J. Topol, M. P. Weiner, O. Harismendy, J. Olson, D. R. Link, K. A. Frazer, Microdroplet-based PCR enrichment for large-scale targeted sequencing. *Nat. Biotechnol*. **27**, 1025–1031 (2009).

33. D. J. Eastburn, A. Sciambi, A. R. Abate, Picoinjection enables digital detection of RNA with droplet rt-PCR. *PLoS One*. **8**, e62961 (2013).

34. A. R. Wheeler, H. Moon, C.-J. Kim, J. A. Loo, R. L. Garrell, Electrowetting-based microfluidics for analysis of peptides and proteins by matrix-assisted laser desorption/ionization mass spectrometry. *Anal. Chem*. **76**, 4833–4838 (2004).

35. A. H. C. Ng, B. B. Li, M. D. Chamberlain, A. R. Wheeler, Digital Microfluidic Cell Culture. Annu. Rev. Biomed. Eng. 17, 91–112 (2015).

36. R. Cole, Parallel Merge Sort. *SIAM Journal on Computing*. **17** (1988), pp. 770–785.

37. M. Dhar, J. N. Lam, T. Walser, S. M. Dubinett, M. B. Rettig, D. Di Carlo, Functional profiling of circulating tumor cells with an integrated vortex capture and single-cell protease activity assay. *Proc. Natl. Acad. Sci. U. S. A*. **115**, 9986–9991 (2018).

38. R. E. Vandenbroucke, L. Dejager, C. Libert, The first MMP in sepsis. *EMBO Mol. Med*. **3** (2011), pp. 367–369.

39. G. Martin, V. Asensi, A. H. Montes, J. Collazos, V. Alvarez, J. A. Carton, F. Taboada, E. Valle-Garay, Role of plasma matrix-metalloproteases (MMPs) and their polymorphisms (SNPs) in sepsis development and outcome in ICU patients. *Sci. Rep*. **4**, 5002 (2014).

40. Vanlaere, C. Libert, Matrix metalloproteinases as drug targets in infections caused by gram-negative bacteria and in septic shock. *Clin. Microbiol. Rev*. **22** (2009), 224–39.

41. L. Nissinen, V.-M. Kähäri, Matrix metalloproteinases in inflammation. *Biochim. Biophys. Acta - Gen. Subj.* **1840**, 2571–2580 (2014).

42. L. Ravanti, V. M. Kähäri, Matrix metalloproteinases in wound repair (review). *International Journal of Molecular Medicine* (2000).

43. A. Gutiérrez-Fernández, M. Inada, M. Balbín, A. Fueyo, A. S. Pitiot, A. Astudillo, K. Hirose, M. Hirata, S. D. Shapiro, A. Noël, Z. Werb, S. M. Krane, C. López-Otín, X. S. Puente, Increased inflammation delays wound healing in mice deficient in collagenase-2 (MMP-8). *FASEB J*. **21**, 2580–2591 (2007).

44. E. M. Miller, A. R. Wheeler, A Digital Microfluidic Approach to Homogeneous Enzyme Assays. *Analytical Chemistry*. **80** (2008), pp. 1614–1619.

45. D. H. Nam, X. Ge, Development of a periplasmic FRET screening method for protease inhibitory antibodies. *Biotechnol. Bioeng*. **110**, 2856–2864 (2013).

46. I. I. Bogoch, H. C. Koydemir, D. Tseng, R. K. D. Ephraim, E. Duah, J. Tee, J. R. Andrews, A. Ozcan, Evaluation of a mobile phone-based microscope for screening of Schistosoma haematobium infection in rural Ghana. *Am. J. Trop. Med. Hyg*. **96**, 1468–1471 (2017).

47. M. R. Bashir, L. Bhatti, D. Marin, R. C. Nelson, Emerging applications for ferumoxytol as a contrast agent in MRI. *J. Magn. Reson. Imaging*. **41**, 884–898 (2015).

48. M. Lu, M. H. Cohen, D. Rieves, R. Pazdur, FDA report: Ferumoxytol for intravenous iron therapy in adult patients with chronic kidney disease. *Am. J. Hematol*. **85**, 315–319 (2010).

49. S. Kahkeshani, J. E. Kong, Q. Wei, D. Tseng, O. B. Garner, A. Ozcan, D. Di Carlo, Ferrodrop Dose-Optimized Digital Quantification of Biomolecules in Low-Volume Samples. *Anal. Chem*. 90, 8881–8888 (2018).

50. H. Lin, Y. Zhao, S. Lin, B. Wang, C. Yeung, X. Cheng, Z. Wang, T. Cai, W. Yu, K. King, J. Tan, K. Salahi, H. Hojaiji, S. Emaminejad, A rapid and low-cost fabrication and integration scheme to render 3D microfluidic architectures for wearable biofluid sampling, manipulation, and sensing. *Lab Chip*. **19**, 2844–2853 (2019).

51. H. Lin, H. Hojaiji, S. Lin, C. Yeung, Y. Zhao, B. Wang, M. Malige, Y. Wang, K. King, W. Yu, J. Tan, Z. Wang, X. Cheng, S. Emaminejad, A wearable electrofluidic actuation system. *Lab Chip*. **19**, 2966–2972 (2019).

Chapter 4 . Single Cell Profiling: Single-Domain Multiferroic Array-Addressable Terfenol-D (SMArT) Micromagnets for Programmable Single-Cell Capture and Release

4.1 Introduction

Programmable multiferroic materials can enable a technological transformation in magnetic cell separation, from bulk cell separation via coarsely applied external magnetic fields[1-3] to single-cell separation via localized and programmable magnetoelastic micromagnets.[4-9] Over the past decades, magnetic cell separation has been widely used to separate cells in bulk by binding superparamagnetic beads to specific cell membrane proteins (Figure 4-1b).[10,11] Once the cell surface is functionalized with magnetic beads, an external magnetic field (H) can direct the bulk migration of targeted cells in complex fluids (e.g., blood).[12,13] However, new advances in cell engineering for personalized therapies[14-17] can benefit from selection of individual cells based on their complex behaviors or time-dependent functions (e.g., cell-killing, secretion, motility),[18-22] which may not be directly correlated to cell surface protein expression. Therefore, a new generation of single-cell magnetic separation techniques is needed with precise and programmable cell capture/release that is scalable across massive arrays.[23,24]

The current landscape for magnetic cell separation consists of soft and hard magnetic materials.[27] Soft magnetic materials with a low coercive field (Hc) lack sufficient fields to capture cells independently without an external inhomogeneous magnetic field (H).[28] On the other hand, hard magnetic materials with high H_c lack programmability to release target cells for downstream analysis.[29] The inability of prior techniques to change the intrinsic magnetic state nor modulate the magnetic amplitude locally prevents arrayed programmability at the microscale.

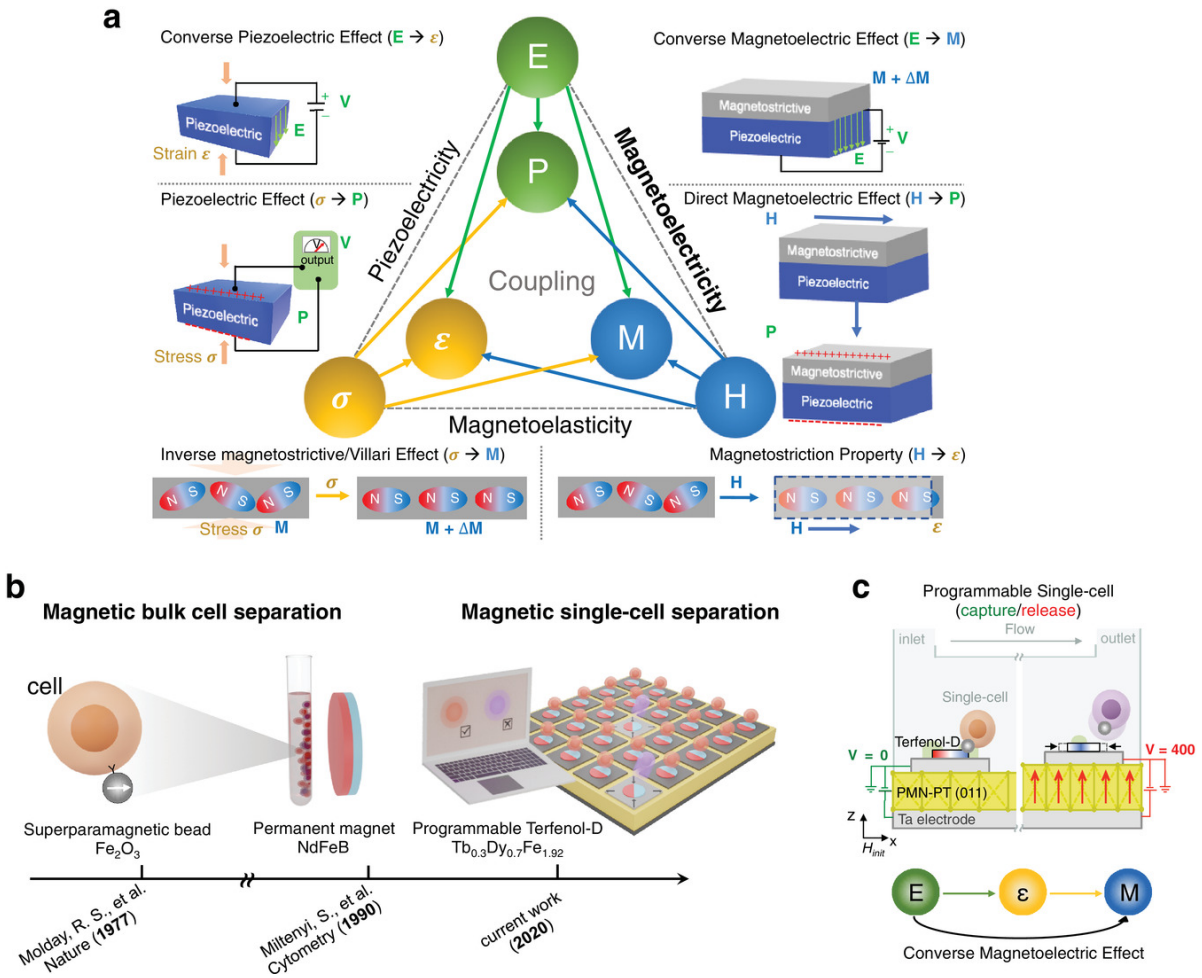

Figure 4-1 SMArT cell separation device concept and operation. **(a)** Schematics of coupling multiferroic and magnetoelectric materials. Composite multiferroic heterostructure Terfenol-D/PMN-PT combines ferromagnetic and ferroelectric materials to collectively achieve a robust magnetoelectric effect. The underlying working principle is the converse magnetoelectric effect which controls the magnetization in Terfenol-D via the induced strain from the ferroelectric PMN-PT. The induced strain causes a magnetization change in the magnetic material as a result of the inverse magnetostrictive effect, a.k.a. Villari effect.[25,26] The phase control diagram in the center has been adapted from.[5] **(b)** Technological development of magnetic cell separation over the past decades. **(c)** Cross-sectional schematic of SMArT micromagnet for single-cell separation via strain-mediated multiferroics to turn on and off the capture and release of cells via voltage application to the device.

We propose the usage of a composite multiferroic platform that utilizes the converse magnetoelectric effect (see Figure 4-1a) to control magnetoelastic materials with programmable and strain-tunable magnetization at the microscale. This approach presents an opportunity to increase magnetic separation resolution to the single-cell level.[30-32]

While magnetoelastic materials have been extensively studied in a range of energy efficient applications, including non-volatile memory,[33-37] actuators,[38-40] and transducers,[41,42] attempts toward cell manipulation have yet to be explored. Applying an initialization field (H_{init}) to sufficiently small (<1 μm) magnetoelastic nanostructures produces single magnetic domains with local stray fields (H_s) that can replace inhomogeneous external magnetic fields (H) for cell capture.[43-45] However, highly localized magnetic stray fields associated with typical single magnetic domain nanostructures (<1 μm) are insufficient for cell capture alone. Scaling up the physical size of magnetoelastic nanostructures to the size of a single cell ≈10 μm is required, but the larger soft magnetoelastic structures produce multi-domain magnetic states rather than single magnetic domains due to the energy competition between exchange energy and demagnetization energy.[46] These multi-domain states produce non-uniform magnetic stray fields, which is less effective for single cell capture/localization (Figure S3, Supporting Information). Furthermore, the complexity of multi-domain structures poses a challenge in reliably controlling the magnetic state for targeted cell release (Figure 4d). Larger single-domain structures are needed for effective magnetic cell trapping and manipulation due to the single-domain strong stray fields (Figure 2). However, larger single domain structures have not been previously achievable with the current magnetoelastic materials.

In this study, we were able to achieve large single-domain states (20 μm) that are capable of single-cell capture with single-domain multiferroic array-addressable Terfenol-D (SMArT) micromagnets, an intermetallic compound with the highest magnetostrictive strain of any known room temperature soft magnetoelastic material.[47] By coupling stress into these single-domain Terfenol-D structures, we were able to alter their magnetic state and achieve single-cell release (Figure 4-1c).

4.2 Materials and Methods

4.2.1 Terfenol-D film deposition, micropatterning, and characterization

Terfenol-D thin films (60 nm) were produced by DC magnetron sputtering using a $Tb_{0.3}Dy_{0.7}Fe_{1.92}$ alloy target obtained from TdVib LLC. USA. Different types of substrates were used for depositing the Terfenol-D films. Silicon wafers were used for determining the optimum properties of the Terfenol-D film, transparent Sapphire wafers were used for XAS/XMCD studies in transmission mode, and PMN-PT substrates with top and bottom electrodes were used for inducing strain to the film through the application of voltage. The major sputtering process parameters used to produce the Terfenol-D thin films were 250 Watts of sputtering power, substrate-to-target distance of 5.5 cm, an Ar gas pressure of 5 mTorr and substrate temperature of 250 °C. Following this deposition, the film was post-annealed in-situ at 450 °C for 4 hours at a chamber pressure below 5×10^{-6} Torr to create polycrystalline films. For XMCD-PEEM imaging, we used finely polished PMN-PT [011] cut of 20 mm x 10 mm x 0.5 mm, with e-beam deposited 80 nm thickness of Al_2O_3 on the top surface and Ti (5 nm)/Pt (50 nm) on bottom surface as a substrate to sputter deposit Ta/Terfenol-D (60 nm)/Ta multilayers.

Terfenol-D micropatterns were fabricated using a conventional photolithographic method followed by Ar etching. The process consisted of spin coating of negative photoresist AZ nLOF 2020 onto the film surface followed by UV exposure using a Karl Suss mask aligner to transfer the pattern from the mask by hardening the photoresist. The film with transferred pattern was developed with AZ MIF 300 developer by dissolving the unexposed soft photoresist. After the photolithographic process the film with hardened photoresist was loaded into STS-AOE etcher to etch away the uncovered photoresist film region with Ar ions. The etched films were ultrasonicated in acetone to remove the photoresist. Finally, the microstructures were characterized and used for fabricating the single-cell separation devices.

The structural and magnetic characterization of the films and their microstructures were carried out using several techniques. X-ray diffraction identified the film structure as face-centered cubic based on its diffraction pattern (Figure 4-2a). Terfenol-D films on 4" diameter silicon substrates were chosen to determine the residual stresses in the film using a wafer curvature method. Crystallized Terfenol-D films showed a residual tensile stress of 70 MPa. A SQUID magnetometer was used to determine the saturation magnetization M_s, coercivity H_c and remanence, M_r of the film as well as the microstructures. All the in-plane magnetization versus applied magnetic field plots obtained for films on Si, sapphire and PMN-PT substrates demonstrated squareness (M_r/M_s) greater than 0.85 and M_s around 700 kA/m. The coercive field value of the films on Si and sapphire was H_c ~2300 Oe, whereas the film on PMN-PT H_c ~3000 Oe. The large coercivity and remanence values are largely attributed to the intrinsic residual stresses that arise during the deposition process. The residual stresses produce a large magnetoelastic induced in-plane easy axis producing both high coercivity and high remanence.

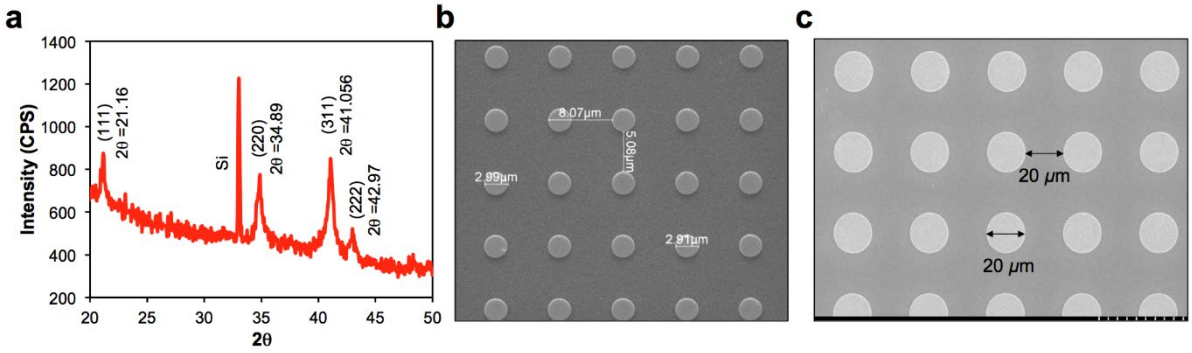

Figure 4-2 Micropatterning and characterization of Terfenol-D microstructures**. (a)** X-ray diffraction (XRD) pattern of the Terfenol-D film deposited on a Si substrate. **(b)** Scanning electron microscope (SEM) micrograph of (b) 3 μm diameter and **(c)** 20 μm diameter microdisks.

Scanning Electron Microscopy (SEM) imaging and Magnetic Force Microscopy (MFM) were used to characterize the morphology and magnetic states of the microstructures respectively. The spacing between 3 and 20 μm diameter microdisks reduced strong dipole-dipole interactions between neighboring disks to enable the magnetic capture of single-cells to a single Terfenol-D microstructure. The disk geometric variations were less than 5% based on optical inspection and measurement. The magnetic states of the 3 μm diameter and 20 μm diameter microdisks were imaged using MFM and XMCD-PEEM respectively.

4.2.2 XMCD-PEEM imaging of single-domain and multi-domain magnetoelastic microstructures

We used XMCD-PEEM to image the magnetic domains at the absorption edges of individual elements in Terfenol-D microstructures. The experiment was conducted with PEEM-3 photoemission electron microscope at beamline 11.0.1.1. of the Advanced Light Source. Prior to imaging, the sample was loaded into the high vacuum etching chamber for Ar ion sputter cleaning to remove the 4 nm thick Ta capping layer and the top few nm of Terfenol-D. After sample preparation, the sample was transferred into the PEEM chamber at a pressure of 3E-8 Torr. The X-ray absorption spectrum (XAS) of Fe was examined to check if the sample surface was oxidized. In Figure 4-3b, the XAS taken with a photon energy between 695 and 730 eV did not show a multiplet signature which could indicate the presence of an oxidation state. The measured XAS matched that of unoxidized Fe, implying that the Ta capping layer protected well the reactive Terfenol-D microstructures.

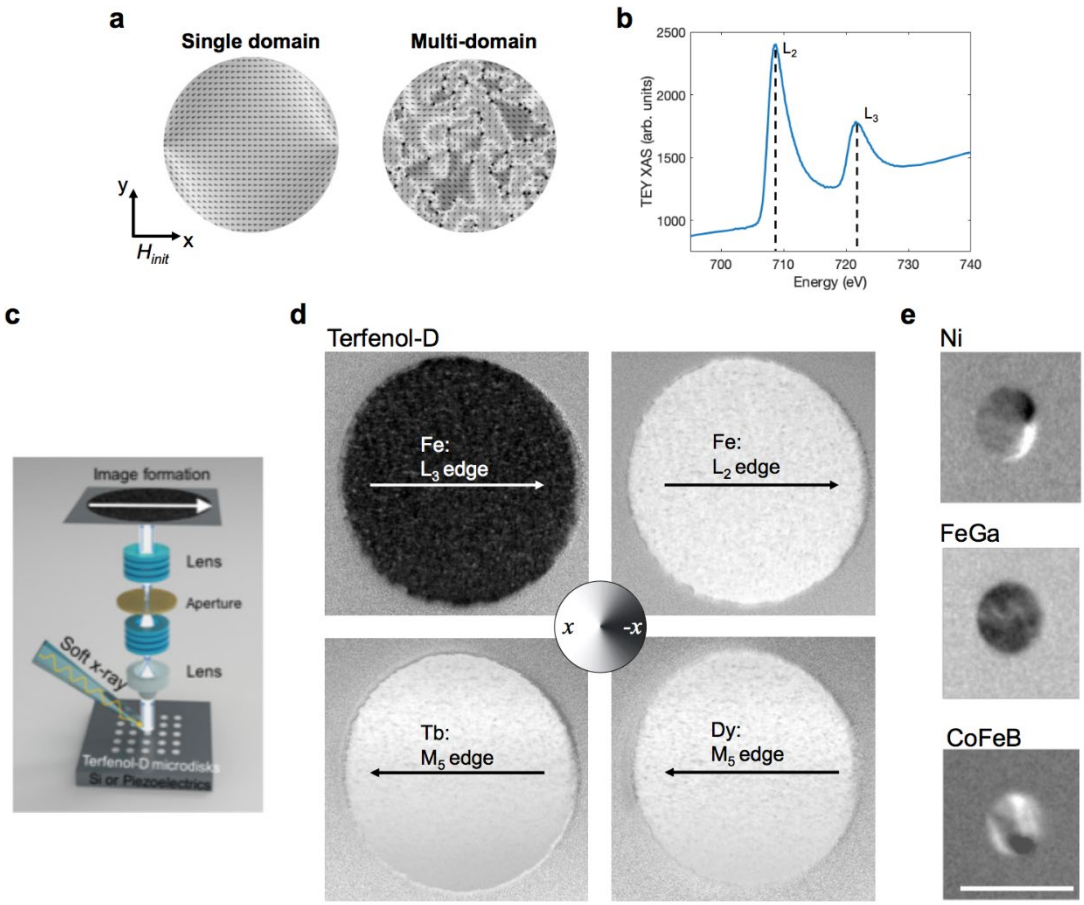

Figure 4-3 XMCD-PEEM imaging of single domain and multi-domain magnetoelastic microstructures**. (a)** An example of single domain and multi-domain states in disks at relaxation, simulated by mumax3 micromagnetics modeling, a 2D plane on the surface of microstructure. **(b)** X-ray absorption spectrum (XAS) image of the magnetic domain at Fe absorption edges. The X-ray energies were then tuned to the energies of Fe L_3 (706.9 eV) and L_2 (719.9 eV) absorption edges, respectively to excite the electron 2p→3d transition with circularly polarized x-ray demonstrated in the **(c)** Schematics of XMCD-PEEM experimental setup. **(d)** XMCD-PEEM images of the magnetic contrast at the elemental absorption edges of all three elements (Tb, Dy, Fe) in the Terfenol-D confirm the single domain configuration in the 20 μm Terfenol-D microstructures. The black contrast indicates the magnetization is pointing along the $+x$ direction; the white indicates the magnetization is pointing in the $-x$ direction. The entire disk functions nearly as a magnet with a single domain. **(e)** XMCD-PEEM images of Ni, FeGa, and CoFeB disks with 2 μm in diameter grown on PMN-PT reveal multi-domain configurations at remanence. Scale bar, 4 μm.

To image the magnetic domain at the Fe absorption edges, the X-ray energies were then tuned to the energies of Fe L_3 (706.9 eV) and L_2 (719.9 eV) absorption edges, respectively to excite the electron 2p→3d transition with circularly polarized x-ray. The secondary electrons emitted from the magnetic sample were then accelerated from the sample to the objective lens via a strong electric field. After passing through a series of lens, the images taken at two x-ray polarities were recorded (Figure 4-3c).

The difference between the two XAS images is the XMCD-PEEM image showing the magnetic contrast. Due to the opposite sign of the spin-orbit coupling in $2p_{3/2}$ and $2p_{1/2}$ states, the XMCD effects at the two absorption energies will have opposite sign. It is thus expected that the magnetic contrasts be opposite to each other when taken at the two edges. Two images were taken for the same microstructure at each absorption edge energy by left and right circularly polarized x-rays. Pixel-by-pixel difference of the two images yielded the XMCD-PEEM image with magnetic contrast, revealing the ferromagnetic domain in the microstructure. XMCD images from Fe L_3 and L_2 edges with opposite contrast confirming the presence of an effective single magnetic domain up to 20 μm in diameter. In addition, the XMCD-PEEM images were also taken at the energy of Tb and Dy M_5 edge to confirm the coupling behavior between the elements and ferrimagnetic behavior of Terfenol-D. Figure S3e shows the experimental results from PEEM with some of the most studied magnetoelastic microdisks patterned on PMN-PT. The microdisks of Ni, FeGa, and CoFeB reveled a multi-domain state at remanence with 15 nm in thickness and 2 μm in diameter as a result of the energy competition between exchange energy and demagnetization energy. However, Terfenol-D showed an effective single domain at remanence state an order of magnitude

larger than the rest. Thus, enabling Terfenol-D micromagnet programmability at the scale of a single-cells with 10-20 μm in diameter.

4.2.3 Mapping the magnetic domain capture regions via fluorescently-labeled magnetic beads (FMBs)

To characterize the magnetic capture performance of Terfenol-D microstructures, we developed a high-throughput method to image the magnetic bead binding regions in a large array. PDMS microfluidic channels were fabricated with standard soft photolithography. A mixture of PDMS (Sylgard 184, Dow Corning, Midland, MI, USA) base and curing agent with 10:1 weight ratio was poured over the master wafer and degassed for one hour to remove air bubbles before cured at 65 °C overnight. The microchannels sizing (L) 1 cm x (W) 6 mm x (H) 500 μm were aligned to overarch the Terfenol-D micropatterns. Permanent bonding was formed by applying a thin layer of uncured PDMS on the interface followed by a 2-hour incubation at 65 °C. All surfaces were passivated with surfactant Pluronic F127 (Sigma-Aldrich, St. Louis, MO) to prevent non-magnetic binding or adhesion. We used small fluoresenctly-labeled magnetic beads (FMB) (Spherotech, Libertyville, IL) of 0.5-1 μm in diameter to increase the spatial resolution of the mapped magnetic capture regions. To visualize FMB capture locations on Terfenol-D microstructures, we used an inverted microscope Nikon Ti-U (Nikon, Melville, NY) illuminated by a mercury arc lamp with 4×-100× objectives and recorded via a CCD Coolsnap HQ2 camera (Roper Scientific, Evry, France) (Figure 4-4a). Terfenol-D microstructures are detected and converted to grayscale where white pixels represent FMBs. An in-house Matlab code was developed to overlay images and normalize pixel intensity to generate a heat map of the bead distribution from a number (n) of Terfenol-D microdisks in a large array (Figure 4-4b). Single-domain Terfenol-D microstructures consistently

demonstrated uniform magnetic binding regions on the magnetized poles. However, larger Terfenol-D microstructures demonstrated scattered magnetic bead binding regions between the magnetized poles (Figure 4-4c). Based on the heat map of the magnetic capture regions we were able to identify single-domain and multi-domain states in magnetoelastic microstructures.

4.2.4 In-situ high-throughput measurement of the magnetoelastic stray field (H_s) magnetic binding force in a viscous medium

To program magnetic capture and release of single-domain magnetoelastic microstructures in a large array in viscous medium, we need to have a measurable magnetic binding force for suspended magnetic beads in microchannels. Other conventional magnetic force measurement methods like fluxgate-MFM, scanning hall probe microscope (SHPM) and scanning SQUID microscope achieve measurements at high spatial resolution (10 nm), but they are not scalable for a large array of thousands of magnetoelastic microstructures. In addition, these methods do not factor other non-magnetic external forces in viscous medium in a microfluidic set-up that compete with the magnetic binding force (F_m) and influence magnetic bead capture/release. Therefore, we have developed an in-situ high-throughput method to achieve multiple measurements of the magnetic binding force of magnetically initialized Terfenol-D microstructures in large numbers using fluorescence imaging and image analysis methods described in 4.2.3.

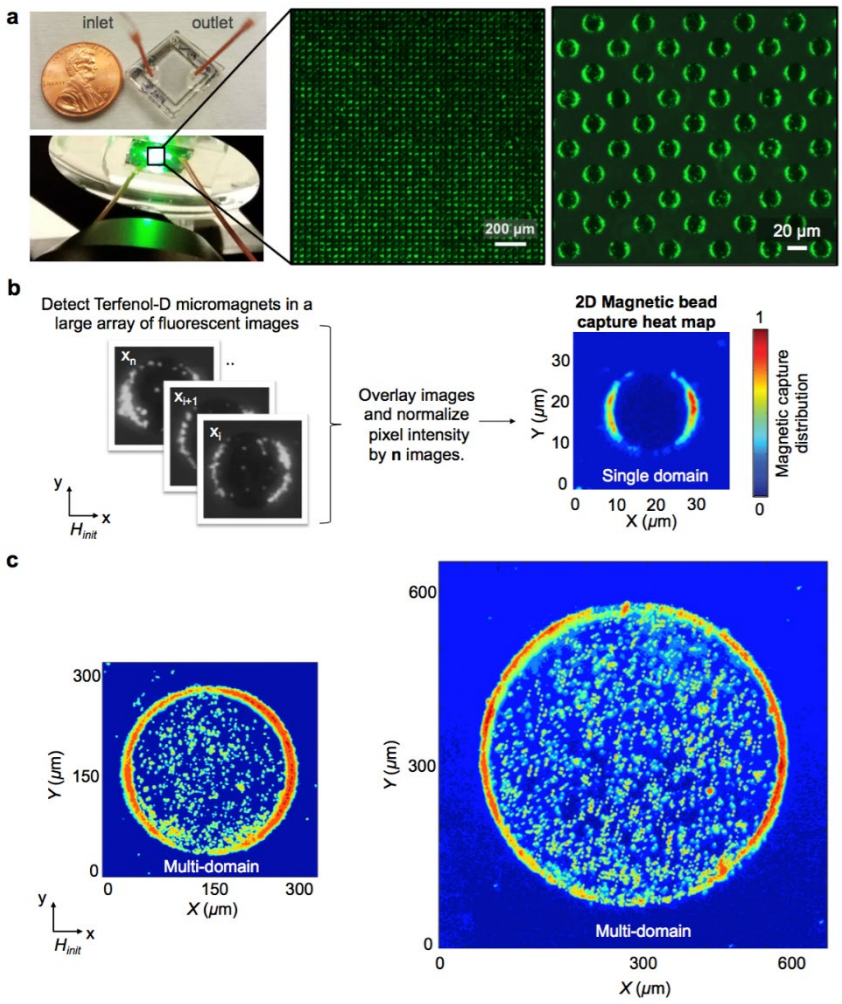

Figure 4-4 High-throughput imaging of magnetic bead capture regions on magnetoelastic microstructures in a large array**. (a)** Microfluidic device integration on top of Terfenol-D micropatterns fabricated on sapphire (top) and silicon (bottom). Fluorescence microscopy images of the large array were acquired after introducing fluorescently labeled magnetic beads (FMB) to a number of n magnetoelastic microstructures. Uniform magnetic bead capture was observed across a massive array of magnetically initialized Terfenol-D single-domain microstructures. **(b)** Image analysis software was used to quantify measurements and generate heatmaps of the magnetic bead capturing regions, where pixels with higher intensity correspond to the magnetic bead locations. Single-domain Terfenol-D microstructures demonstrated uniform magnetic bead capture locations on the magnetized poles. **(c)** Heat maps of multi-domain microstructures 250 μm and 500 µm in diameter demonstrated scattered bead capture locations between the magnetized poles.

Magnetic beads of different sizes were introduced to magnetically initialized Terfenol-D microstructures at different flow rates. Each flow rate exerts an external competing hydrodynamic drag force (F_d) that counteracts the local magnetic binding force (F_m) of the Terfenol-D stray field (H_s) across a large microstructure array. The magnetic bead interactions are tracked on many microstructures at the same time and same flow condition to get multiple measurements of the magnetic field landscape of each Terfenol-D microstructure. We observed three magnetic bead interactions with magnetized Terfenol-D microstructures, bead capture, tumbling and release. (i) magnetic beads are captured or maintained on Terfenol-D microdisks when the magnetic binding force dominates over the hydrodynamic drag force ($F_m > F_d$). (ii) At higher flow rates, magnetic beads are released but then tumble or jump between Terfenol-D trapping regions. Given the temporary binding or release of the magnetic beads from the micromagnet, we assume the magnetic binding force and hydrodynamic drag are similar ($F_m \sim F_d$) in this condition. (iii) Lastly, when the hydrodynamic drag dominates over the magnetic binding force ($F_m < F_d$), magnetic beads are released instantly with limited stray field (H_s) influence from the downstream neighboring disks in the Terfenol-D micropattern array.

To calculate the counteracting hydrodynamic drag force in each condition, we first considered Faxén's correction to Stoke's drag force, since the captured bead is located near the Terfenol-D surface under a Stokes flow regime with limited inertia. The hydrodynamic drag (F_d) was defined as

$$F_d = 6\pi\eta U D \xi$$

where D is the bead diameter, η is the viscosity of the suspending liquid, U is the average fluid velocity at the center of the bead, and ζ is the near surface correction factor defined by the power series expansion of the ratio of the bead radius (a) to the distance from the wall surface (l). In this study we used the three term power series of Faxén correction to the translational drag force parallel to the wall, defined as

$$F_d = \frac{6\pi\eta UD}{1 - \left(\frac{9}{16}\right)\left(\frac{a}{l}\right) + \left(\frac{1}{8}\right)\left(\frac{a}{l}\right)^3}$$

We then matched the theoretical drag force calculation with Finite Element Method (FEM) COMSOL Multiphysics software to simulate 3D fluid-particle interaction in the experimental conditions. The channel geometry was modeled using dimensions of the experimental channel (L=10000 μm, W=1000 μm, H= 200 μm), as illustrated in Figure 4-5a. A thin disk represents the Terfenol-D microdisk geometry in which the bead is trapped on its surface and 60 nm away from the substrate wall. A no-slip boundary condition is applied to the channel walls, microdisk, and bead. The inlet flow rate (5-2000 μL/min) and the particle diameter (2.8-9.1 μm) were set using a parametric sweep. The drag force on the particle was calculated by integrating the total stress over the surface of the particle in the x-axis parallel to the flow. Figure 4-5b shows the resulting total drag force (F_d) parallel to the flow direction and opposite to the magnetic force (F_m) at different flow velocities. To estimate the magnetic binding force (F_m), we compared the calculation of (F_d) of different size beads (D = 2.8, 4.5, 7.4 and 9.1 μm) in the tumbling stage where ($F_m \sim F_d$). The magnetically coated beads of different sizes were released at similar hydrodynamic drag force ~ 36 pN, which validates the numerical drag force calculation method (Figure 4-5c).

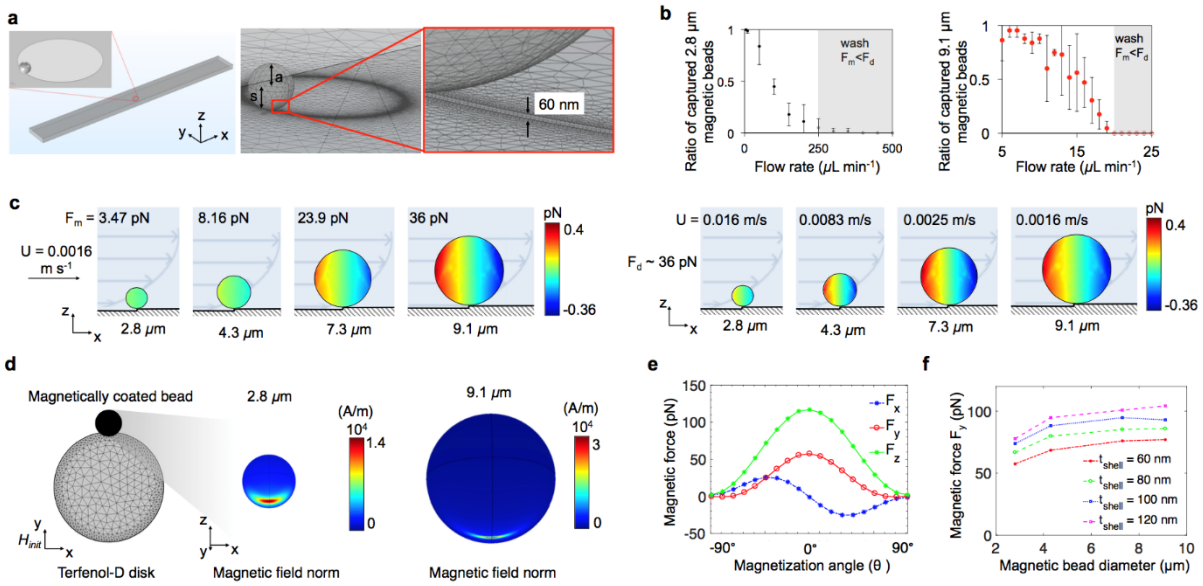

Figure 4-5 High-throughput in-situ measurement of the magnetic binding force for Terfenol-D microstructures in a large array**. (a)** Hydrodynamic drag force for different bead diameters were computed numerically using experimental flow rates, microfluidic channel dimensions and the Terfenol-D microstructure geometry. **(b)** The fraction of magnetic beads released increases at higher flow rates. **(c)** Under the same flow rates, 2.8, 4.3, 7.3 and 9.1 μm beads experience different hydrodynamic drag forces. At the magnetic bead release flow condition, the hydrodynamic drag force measurement is estimated to equal the magnetic binding force ~ 36 pN for different bead diameters. **(d)** Surface distribution of magnetic field norm of both 2.8 μm and 9.1 μm beads with a magnetic shell thickness of 60 nm. The magnetic field norm decays toward zero a few μm away from the beads. **(e)** Angle dependence of magnetic force components on the 2.8 μm bead with shell thickness of 60 nm. The magnitude of total magnetic force reaches the highest when the bead is located along the magnetization y-axis ($\theta = 0°$). Here F_y and F_z are pointing in the *-y* and *-z* directions. **(f)** Finite Element simulation result of magnetic force F_y on the magnetically coated beads with different combinations of bead diameter and magnetic coat thickness. The beads are located at the magnetization axis, as shown in the schematics, corresponding to the experimental observation.

To verify that similar magnetic forces (F_m) are experienced by magnetically coated beads of different sizes, we used COMSOL Multiphysics software to simulate the magnetic force of captured beads on effective single domain Terfenol-D disk of 20 μm in diameter initialized along the y-axis. The magnetic beads used in the experiments consist of a polystyrene core and a thin magnetic iron oxide coating with thickness ranging from 60 to 120 nm, according to the vendor. We thus simulated magnetic beads of different sizes (D = 2.8, 4.5, 7.4 and 9.1 μm) with four different iron oxide shell thicknesses (t_{shell} = 60, 80, 100, 120 nm). The magnetic field norm distribution (A/m) on the surface of the magnetic beads decays toward zero several micrometers away from the disk (Figure 4-5d). This observation helps explain why the magnetic forces experienced by the magnetic beads do not scale proportionally to the bead size, but are in a close range instead. As observed in the experiment, the total magnetic force experienced by the bead is at its largest when the bead is located at the magnetization angle ($\theta = 0°$) along the y-direction (Figure 4-5e). Thus we examine the magnetic forces along y-direction of the beads of different size and shell thickness combinations when they are positioned at the magnetization angle (Figure 4-5f). The in-plane magnetic force F_y of different magnetic bead sizes with the same magnetic shell thickness shows similar magnetic force from the magnetic disk. Since the exact magnetic shell thickness of the same type of beads may vary according to the vendor, the forces from the simulation are a proof-of-concept rather than an accurate reflection of the exact magnetic forces experience by individual beads. Therefore, the in-situ high-throughput experimental measurement method uses one type of magnetically coated beads to average the magnetic binding force from thousands of Terfenol-D microstructures.

4.2.5 Strain mediated single-cell release

To study the effect of strain on Terfenol-D single-domain and multi-domain microstructures, we tracked the magnetic bead capture regions before and after applying strain on the PMN-PT substrate. Figure 4-6 demonstrates the experimental steps of using magnetic beads to locate the newly induced magnetic easy axis angle after applying strain. In addition, we noticed beads attached near the Terfenol-D microdisks dislocate to a new magnetization angle after applying strain.

To track in real-time the release of captured magnetically labeled cells associated with strain, we tracked the movement of the PMN-PT surface that is near a Terfenol-D microstructure (labeled with *) while applying voltage. We used stationary beads on the PMN-PT surface that are not attached to the Terfenol-D microstructures for the image analysis tracking code. The maximum strain value from Figure 3b was used to correspond to the PMN-PT maximum surface displacement. Then the PMN-PT displacement values in between were assigned proportionally to the strain values. The bead translated an average distance of 6.5 μm with the PMN-PT surface from 0 ppm (blue) to maximum strain of 2150 ppm (yellow). Measuring the PMN-PT surface displacement while recording magnetically labeled cells capture and release events enabled synchronization of the strain with shift in magnetization and resulting cell release.

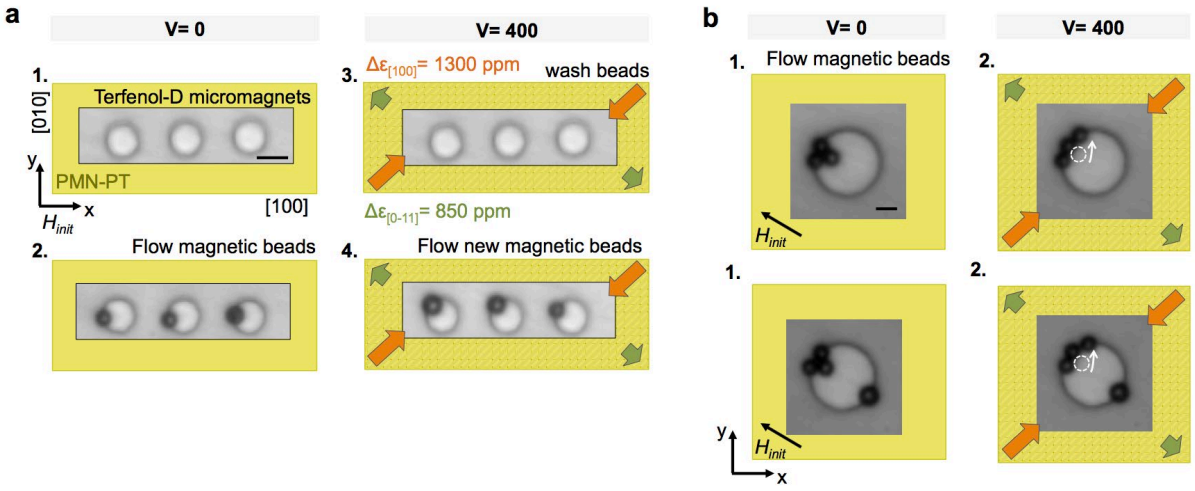

Figure 4-6 Experimental procedure for tracking the change in magnetization pole reorientation of Terfenol-D microstructures after applying strain on PMN-PT substrate (yellow). **(a)** First, we image the Terfenol-D microstructures before introducing beads or applying beads or strain. Second, we flow beads in a microfluidic channel on the PMN-PT substrate and image the Terfenol-D microstructures. Third, we wash away the beads then apply voltage-induced strain on the PMN-PT substrate. Fourth, we flow new magnetic beads and image their locations after strain. We noticed the beads settle on a newly induced magnetic easy axis in the Terfenol-D microstructure. **(b)** We repeat the same procedure but without the washing step (3) on larger microstructures that capture more than one bead on their magnetized pole. We noticed beads that are not directly attached to the magnetized pole dislocate to the new magnetization angle after applying strain. Scale bar, 5 µm.

Jurkat cells (average diameter ~15 μm) were cultured in RPMI 1640 medium supplemented with 10% (v/v) fetal bovine serum and 1% penicillin-streptomycin and maintained ~106cells/mL density. To magnetically label Jurkat cells, streptavidin-coated magnetic beads (Spherotech, Libertyville, IL) were washed with PBS and conjugated with 5 μg/mL biotin anti-human CD45 Antibody (clone HI130: #304003; BioLegend) before added to a suspension of Jurkat cells at a 1:10 cell to bead ratio in culture medium for labeling. The labeling was performed at room temperature with gentle mixing for 1 hour. Magnetically labeled Jurkat cells were captured on the Terfenol-D single-domain microstructures under a low flow velocity condition of 5 μL/min where $F_d < 36$ pN. Single magnetically labeled cells remained captured on the Terfenol-D microdisk until strain was applied with an electric field of 0.8 MV/m as discussed elsewhere. To test Terfenol-D cytocompatibility for adherent cells, we incubated MCF-7 cells on Terfenol-D microstructures at 37°C in a humidified atmosphere with 5% CO2 for a week. Cells grew and expanded on the surface of the Terfenol-D micropatterns (Figure 4-7).

4.2.6 Time-dependent measurement of single-cell secretion

For a proof-of-concept demonstration of dynamic cell profiling on Terfenol-D micromagnet arrays, we performed an adapted IL-2 Secretion Assay (Miltenyi Biotec, 130-090-487) on a trapped array of human primary T cells (average diameter ~8 μm). The human primary T cells were isolated from whole blood using EasySep™ Human T Cell Isolation Kit (STEMCELL Technologies, 17951)and stimulated with ImmunoCult™ Human CD3/CD28 T Cell Activator (STEMCELL Technologies, 10971) when needed. The cell culture was maintained at ~10^6/mL in RPMI 1640 medium supplemented with 10% (v/v) fetal bovine serum, 1% penicillin-streptomycin, and 50 U/mL IL-2.

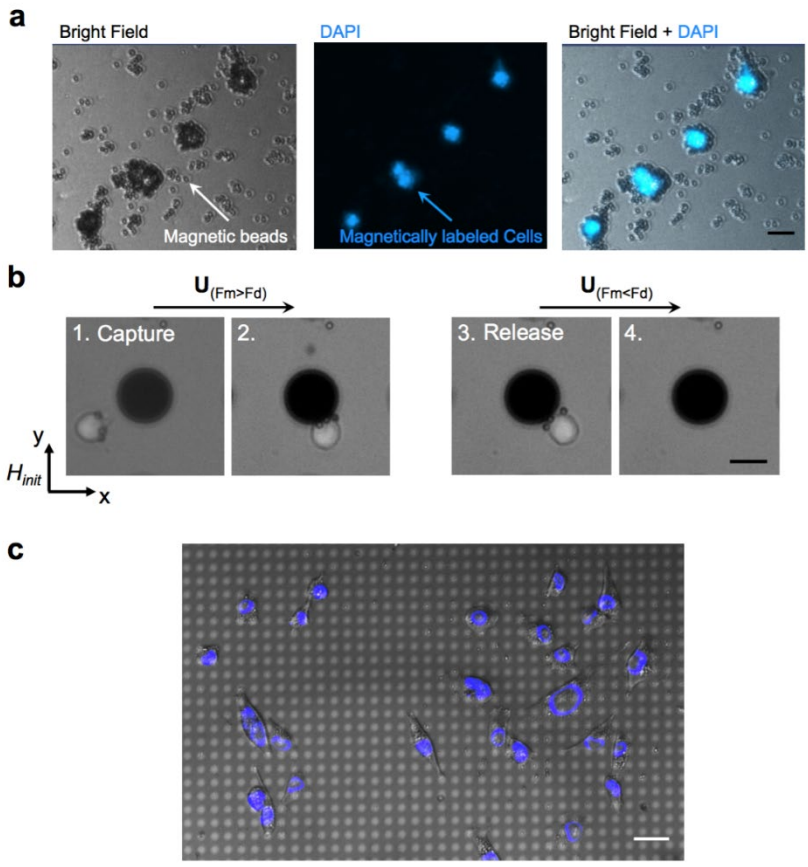

Figure 4-7 Magnetically labeled cell preparation for capture and release via voltage induced strain. **(a)** Fluorescently stained cells coated with magnetic beads are imaged with bright field and fluorescence microscopy. **(b)** Microchannel flow conditions were optimized for cell capture at a flow velocity $U_{(Fm>Fd)}$ and release at $U_{(Fm<Fd)}$ on Terfenol-D microstructures. **(c)** Terfenol-D microstructures were cytocompatible for cell growth and expansion for downstream applications. Scale bar, 20 µm.

Prior to experiment, the human primary T cells were activated for cytokine production by 25 ng/mL PMA (Sigma-Aldrich, P1585) and 1 μg/mL Ionomycin (Sigma-Aldrich, 407951) for 6 hours at 10^7 cells/mL. The activated cells were thoroughly washed, stained with Hoechst to locate nuclei, labeled with magnetic beads as described in 4.2.5 and IL-2 Catch Reagent following vendor's protocol. The labeled cells were resuspended at ~106/mL in RPMI 1640 containing 0.1% (v/v) phycoerythrin (PE) labeled IL-2 Detection Antibody, and immediately injected into the microfluidic channel of a SMArT device staged on a Nikon Ti-E fluorescence microscope. A set of DAPI (100 ms exposure) and TRITC (1 second exposure) images were taken every 10 minutes for 2 hours and analyzed using Image J. Magnetically trapped cells were located by matching the nuclei staining in DAPI with the Terfenol-D microdisk patterns, and their secretion signals were quantified by the maximum TRITC fluorescence intensity within each area of interest.

4.3 Results and discussion

4.3.1 Characterization of single-domain Terfenol-D microstructures

We investigate the magnetoelastic properties of Terfenol-D microstructures for strain induced cell capture/release on sputter-deposited Ta(23 nm)/Terfenol-D (68 nm)/Ta(32 nm) multilayer thin films on PMN-PT $[Pb(Mg_{1/3}Nb_{2/3})O_3]_{1-x}[PbTiO_3]_x$ (PMN-PT) [011]-cut piezoelectric substrate. Electron-beam evaporated Al_2O_3 (80 nm) was deposited between the PMN-PT and Terfenol-D to prevent oxygen diffusion into the Terfenol-D. The Terfenol-D is patterned by optical lithography followed by Ar etching (Figure 4-8a-d).

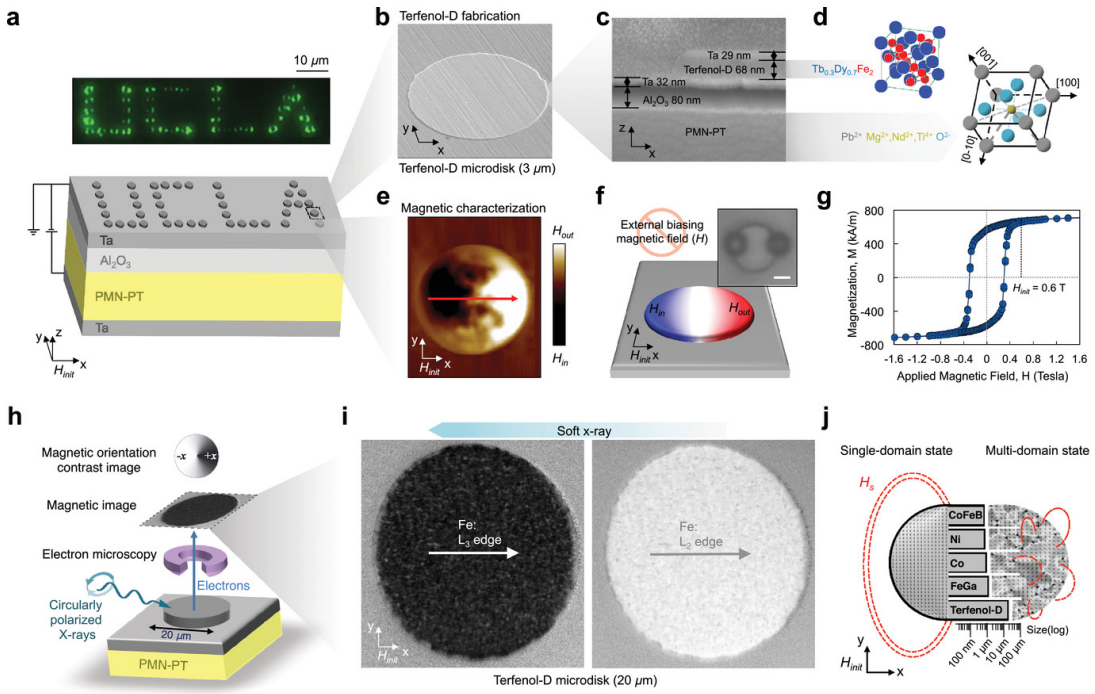

Figure 4-8 Fabrication and characterization of single-domain Terfenol-D microstructures. **(a)** Schematic of the SMArT device and microscopy image showing magnetic bead capture (green) on Terfenol-D single-domain micropatterns on a PMN-PT substrate without the use of an external magnet. **(b,c)** Scanning electron microscopy (SEM) images of a 3 μm Terfenol-D disk (b) and cross-sectional cut by focused ion beam (FIB) (c), showing **(d)** Terfenol-D microstructure on PMN-PT. **(e,f)** Magnetic force microscopy image of the 3 μm disk (e) reveals a single domain configuration (f) that enables strong and precise magnetic trapping of magnetic beads on the magnetized poles (scale bar: 1 μm). **(g)** Magnetic hysteresis loop of the Terfenol-D disks shows a large saturation magnetization of 780 kA m^{-1} and a coercivity of 0.3 T, as measured by SQUID. A large fraction of the magnetization is retained upon the removal of the saturation magnetic field. **(h)** XMCD-PEEM imaging is used to image the magnetic domain state of **(i)** magnetic contrast in a 20 μm disk at the elemental absorption edges of Fe, where white contrast indicates the magnetization pointing in the *-x* direction and the black the *+x* direction. The opposite contrasts taken at two absorption edges of Fe confirms the effective single-domain magnetic configuration without an external magnetic field. **(j)** Single-domain states in magnetoelastic Terfenol-D at remanence are observed at 20 μm diameters, while other magnetoelastic micromagnets (CoFeB, Ni, FeGa) switch to a multi-domain state around 1-2 μm in diameter as observed in XMCD-PEEM after magnetic-field removal.

Terfenol-D thin films have a relatively large coercive field (H_c) of 0.3 T, saturation (M_s), and remanent (M_r) magnetization of 710 and 600 kA m^{-1}, respectively, measured by a superconducting quantum interference device (SQUID) (Figure 4-8g). A strong dipolar contrast is observed in 3 μm Terfenol-D disks indicating single-domain states imaged by magnetic force microscopy (MFM) following the application of an in-plane magnetic field (H_{init}) of 0.5 T (Figure 4-8e).

A single domain state in these large disks (3 μm) is possible due to the large residual tensile stress of 70 MPa[48] developed during the Terfenol-D annealing process, which also produces large in-plane anisotropies and coercive fields. This large residual stress coupled with the material's large saturation magnetostriction $\lambda_s \approx$ 880 ppm produces an effective magnetoelastic anisotropy sufficient to produce a pseudo-single domain state in these micropatterned disks.[49] Following initialization, and in the absence of an external magnetic field, magnetic beads were uniformly captured at the magnetized poles as illustrated in (Figure 4-8a,f).

Surprisingly, we found that effective single magnetic domain states persist in substantially larger microstructures up to 20 μm in diameter and beyond, imaged by X-ray magnetic circular dichroism-photoemission electron microscopy (XMCD-PEEM) (Figure 4-8h). According to the PEEM images taken at the Fe L_2 and L_3 absorption edges, a majority of the magnetic moments point in a single horizontal direction, thus the entire disk functions collectively as a single domain (Figure 4-8i). The black contrast indicates the local magnetization is pointing along the +x direction; the white indicates the magnetization is pointing in the -x direction. At Fe L_2 and L_3 absorption edges, the XMCD has opposite signs of magnetic dichroism (Figure 4-3a–d). The PEEM images acquired at these two absorption edges show opposite magnetic contrast, confirming

that the observed image contrast is magnetic-related, and the structure exhibits a net single domain configuration. In contrast to other soft magnetoelastic materials, this fabrication process produces Terfenol-D with anomalously large single-domain structures an order of magnitude larger in dimension than previously thought possible. More importantly for this application, the domain sizes are on par with single human cell sizes, which have diameter ≈ 10 μm (Figure 4-8j, 4-3e). This large single domain magnetoelastic structure discovery promises a new scale of micromagnetic capture that is sufficiently large to localize and capture a single cell without an externally applied magnetic field. In addition, the magnetoelastic properties of the single domain structures enable strain mediated multiferroic programmability for single-cell release following magnetic capture.

4.3.2 Magnetic capture on single-domain Terfenol-D microstructure arrays

While MFM and XMCD-PEEM are useful for characterizing magnetic domain configurations, they are limited in characterizing the magnetic capture performance of the initialized magnetic stray field (H_s) in a viscous medium. Here, we developed an in situ high-throughput approach to map and measure magnetic capture and release of magnetic materials using Terfenol-D multiferroic microstructures in a microfluidic channel in real-time.

After Terfenol-D micropatterns were magnetically initialized with a saturating field of $H_{init} = 0.5$ T, a microchannel was bonded to the surface of PMN-PT substrate to introduce fluorescently labeled magnetic beads (FMBs) at a low flow rate (Figure 4-9a, 4-4a). With no external magnetic field applied, all of the initialized Terfenol-D microstructures captured suspended FMBs on the magnetized poles (Figure 4-9b).

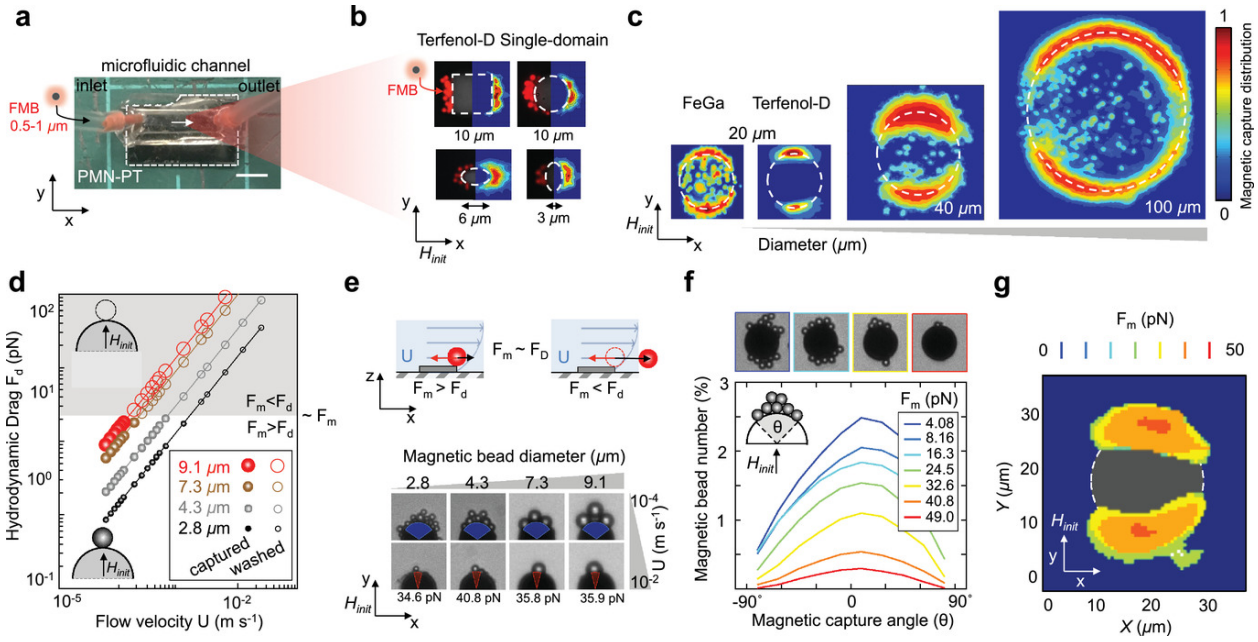

Figure 4-9 Magnetic capture performance of single-domain Terfenol-D microstructure arrays. **(a)** Optical photograph of the microfluidic/multiferroic device (scale bar, 5 mm). **(b)** Mapping the magnetic capture distribution of fluorescently labeled magnetic beads on single-domain Terfenol-D microstructures. **(c)** FeGa structures of the same size transition into a multi-domain state, while Terfenol-D structures of less than 40 μm in diameter remain single-domain. **(d)** Optimized magnetic capture ($F_m > F_d$) and release ($F_m < F_d$) flow conditions to map the magnetic capture behavior of Terfenol-D micromagnets in situ with different magnetic beads sizes (2.8-9.1 μm) illustrated in bright-field images in **(e)** with the governing forces: magnetic binding force F_m and hydrodynamic drag F_d. The solid lines are the theoretical Faxén drag correction force given by Equation[1]. **(f)** The magnetic binding force (F_m) is measured as a function of magnetization angle (θ) on single-domain Terfenol-D 20 μm microdisks via a range of flow velocities to increase the spatial resolution of the 2D magnetic force map illustrated in **(g)**.

Micromagnetic trapping regions were mapped with high-resolution fluorescence imaging (0.16 μm pixel^{-1}) (Figure 4-4b). In addition to PMN-PT substrates, FMB capture was reproducible on Terfenol-D microstructures that were patterned on silicon and sapphire substrates (Figure 4-4a). Terfenol-D structures that range from 3 to 20 μm in size exhibit precise FMB capture based on highly localized fields in the magnetically initialized single-domain poles regardless of their shape anisotropy. Interestingly, 20 μm structures composed of FeGa, with the second largest magnetostriction among soft magnetic materials, result in multi-domain states (Figure 4-9c). Terfenol-D microdisks larger than 40 μm begin to transition into multi-domain state where FMBs were captured in a scattered pattern associated with the smaller domains' stray fields in between the magnetized poles (Figure 4-9c, 4-4b,c). Although this method of FMB capture in fluid does not identify local magnetic spin orientation, it enables magnetic state characterization and magnetic bead capture evaluation for single-domain and multi-domain microstructures in a general microfluidic set-up.

To further investigate the magnetic force (F_m) landscape of the mapped micromagnetic bead binding regions, we incrementally increased the counteracting hydrodynamic drag force defined by the Faxén's correction to the Stokes drag force.

$$F_d = 6\pi\eta UD\xi$$

We explored a range of flow velocities (U = 0.001-0.1 m s^{-1}) and magnetic bead diameters (D = 2.8 - 9.1 μm), where we kept the following two properties constant: fluid viscosity (η), the near-surface correction factor (ξ), which modifies Stokes drag for magnetic beads in close proximity to the surface of the Terfenol-D microstructures.[50, 51] The drag force was then recalculated by 3D

numerical simulation to include the Terfenol-D microdisk under the bead, which was in good agreement with the theoretical drag force (marked in solid lines) (Figure 4-9d ,4-5). Under continuous flow, we estimated the magnetic binding force by increasing the flow rate (and corresponding hydrodynamic drag force, F_d) to the point where the drag force overcomes the magnetic capture force, F_m, causing release of the particle (Figure 4-9e). Since the captured beads of different sizes are magnetically coated with similar thicknesses, larger magnetic beads were released at lower flow rates due to drag force linearly increasing with bead diameter (Figure 4-5b,c). However, all of the magnetically coated beads with different sizes were released at similar $F_d \approx 36$ pN, which serves to validate the average magnetic binding force measurements across different micropatterns (Figure 4-9e). Locally on the Terfenol-D microdisk, we mapped the magnetic force gradient as a function of the magnetization-easy axis angle (θ) where $F_m(\theta = 0) = 49$ pN (Figure 4-9f). As expected for single-domain Terfenol-D magnets, the stray field (H_s) gradient decays away from the magnetization angle ($\theta = 0°$) in the 2D magnetic binding force map (Figure 4-9g. 4-5d–f). Also, a single bead can be captured and arrayed in each micromagnet to probe the strain-induced change in the easy axis angle, as discussed in the next section.

4.3.3 Electrically programmable single-cell capture and release

We further investigated magnetoelastic coupling with voltage-induced microstructural strain to reprogram the micromagnetic Terfenol-D state for magnetic release. We imaged in real-time the microfluidic/multiferroic device to investigate the magnetic bead capture and release behavior before and after applying a voltage induced strain to PMN-PT [011]-cut piezoelectric substrates in the optimized stable flow capture condition (Figure 4-10a).

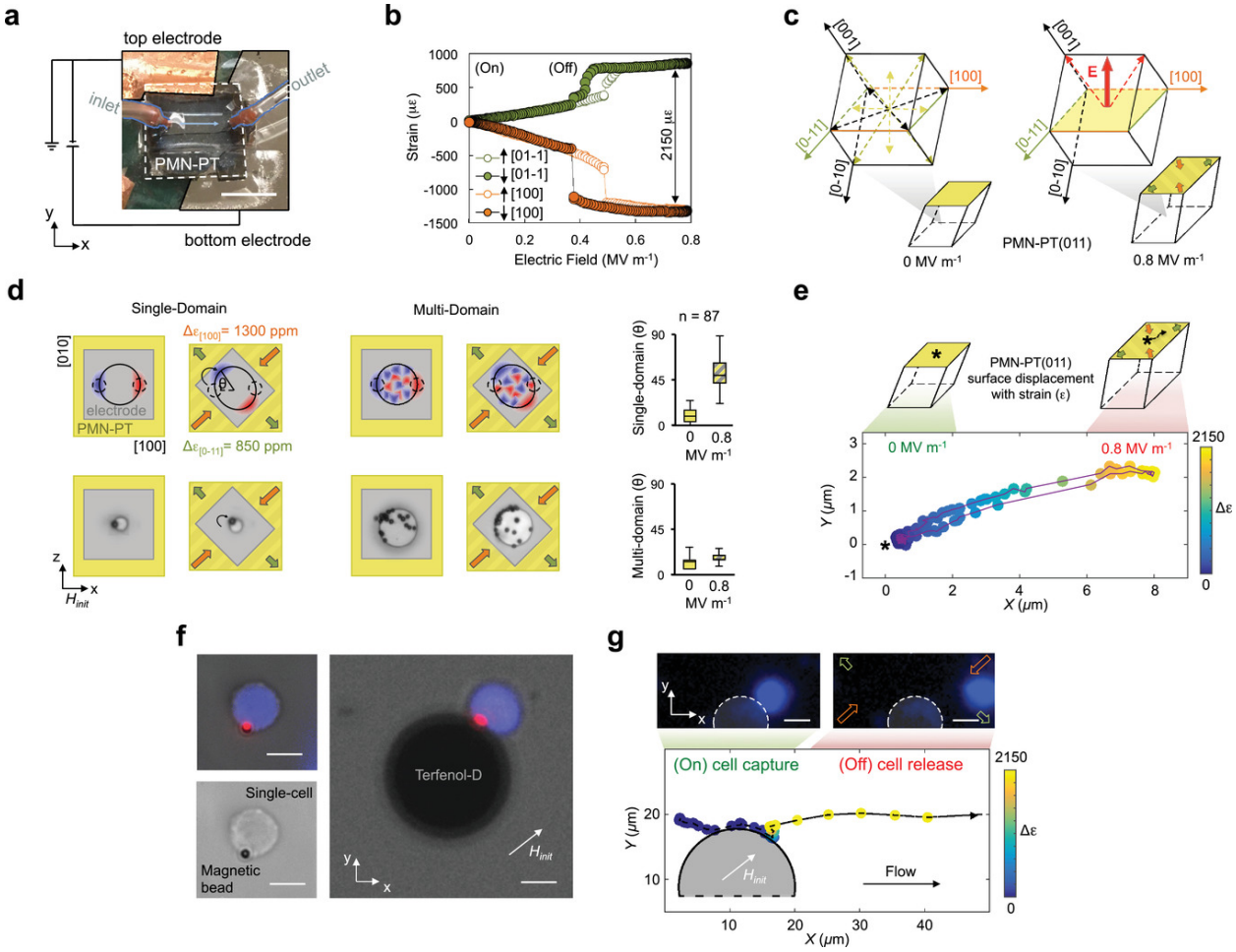

Figure 4-10 Electrically programmable single-cell capture and release via SMArT micromagnets. **(a)** Microfluidic SMArT device set up (scale bar: 5 mm). **(b)** Applying a 0.8 MV m^{-1} electric field induces compressive strain of 1300 ppm along the [100] direction and tensile strain of 850 ppm along [011], illustrated in the PMN-PT crystal structure in **(c)**. **(d)** The resulting total strain of 2150 ppm perturbs the single domain state due to magnetoelastic coupling, reorienting the magnetic domain ≈40° to the easy axis while multi-domains rearrange in a manner that has little impact on the net direction of magnetization. **(e)** Real-time tracking of the displacement on the surface due to strain in the PMN-PT substrate (reference location labeled with *). **(f)** Bight-field and fluorescence images of a magnetically labeled and fluorescently labeled single cell. **(g)** With applied strain, individual magnetically labeled single cells were released from the TerfenolD micromagnets to the outlet of the microchannel.

An electric field of 0.8 MV m^{-1} induces a compressive strain of 1300 ppm along the [100] direction and a tensile strain of 850 ppm along [01-1] direction (Figure 4-10b). The resulting differential strain of 2150 ppm creates a new minimum in the energy landscape, rotating the direction of magnetization in the Terfenol-D disk (Figure 4-10c, 4-6). Consequently, the trapping angle for the magnetic bead shifts by $\Delta\theta = 40°$ after applying the electric field (Figure 4-10d). Originally, the bead is trapped in a direction at an angle 45° relative to both [01-1] and [100] strain axis, as indicated in Figure 4-10d. The electric-field induced easy-axis along [01-1] direction (marked in green, Figure 4-10c) results in this shift in bead capture location. However, in multi-domain microstructures, no substantial change in the magnetic reorientation was observed after applying stain due to the heterogeneous magnetic capture regions (Figure 4-10d).

Leveraging this magnetization reorientation shift, magnetic beads and magnetically labeled single cells were captured on single-domain Terfenol-D microdisks then subsequently released after applying a voltage induced strain (Figure 4-10f,g). We tracked the displacement of the PMN-PT surface as a function of the voltage-induced strain to proportionally assign the strain value while recording the capture/release of magnetically labeled cells (Figure 4-10e). As the magnetic domain stray field reorients toward the newly strain-induced easy axis ([01-1] direction of PMN-PT) at $\Delta\varepsilon = 2150$ ppm (marked in yellow), the cells were released due to the decline of the stray magnetic field x-component counteracting the drag force, which is parallel to the flow direction (Figure 4-10h). Trapped cells in the device were viable for cell culture and expansion for downstream applications (Figure 4-7).

4.3.4 Time-dependent single-cell profiling

We further applied the Terfenol-D micromagnet arrays to evaluate time-dependent properties of a population of cells, specifically the heterogeneous secretion of interleukin-2 (IL-2), a critical cytokine signaling molecule that regulates T cell proliferation and differentiation,[52] A sandwich immunoaffinity assay (Figure 4-11a) was performed to capture secreted IL-2 from immobilized cells back on the surface of the secreting cell via a bi-functional capture antibody targeting CD45, a cell surface protein on T cells, and IL-2. The captured IL-2 subsequently forms a sandwich with a fluorescently labeled anti-IL-2 detection antibody.

As IL-2 molecules were continuously secreted over a 2-h incubation, we observed an increase in fluorescence signal accumulate on the cell membrane of a fraction of cells (Figure 4-11b,c); presumably those with higher rates of secretion of IL-2. By tracking the intensity across an array of magnetically trapped single T cells we observed two distinct sub-populations of T cells (Figure 4-11d), which could be differentiated based on their final accumulated fluorescence signal ($p < 0.001$). The high-secreting cluster of cells reached a 29.1 ± 7.0% increase in signal intensity at the end of 2 h ($n_1 = 4$), while the low-secreting cells averaged a 3.3 ± 4.5% signal increase ($n_2 = 17$). The ability of delicate primary cells to remain viable and secreting over the 2 h period suggests the compatibility of the SMArT platform to separate cells based on time-dependent assays of cell function.

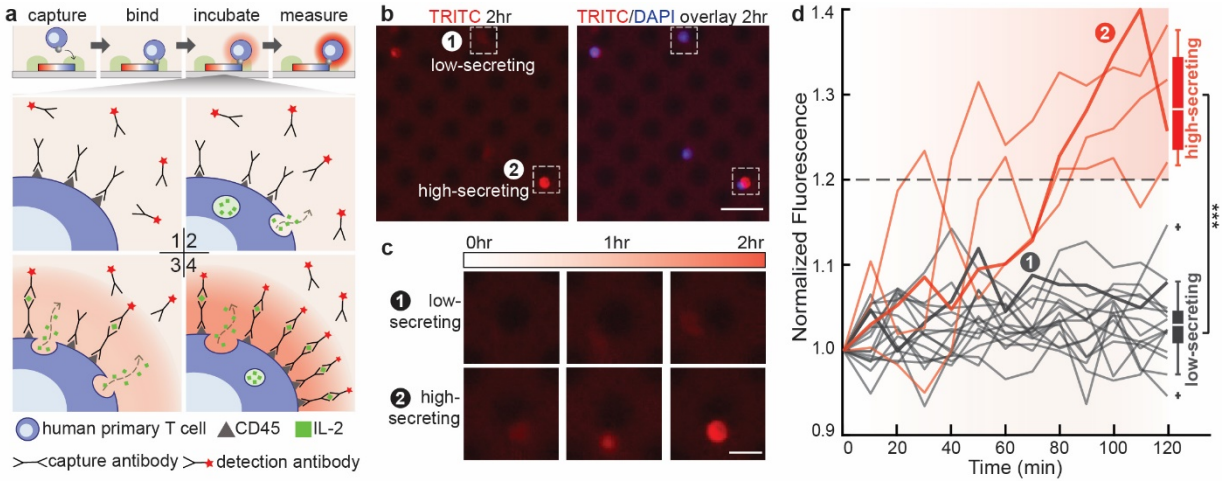

Figure 4-11 Time-dependent secretion measurement of magnetically captured single cells. **(a)** Schematics of the adapted immunoaffinity assay to measure IL-2 secretion from single primary human T cells. **(b)** Fluorescence images of IL-2 secretion signals (TRITC) from human primary T cells (DAPI) at the end of a 2-h incubation (scale bar: 50 μm). One representative low-secreting cell (cell ①) and one high-secreting cell (cell ②) are identified, and their secretion signals at 0, 1, and 2 h are magnified in **(c)** (scale bar: 20 μm). **(d)** Single-cell IL-2 secretion signals tracked every 10 min for 2 h. Sub-populations of high-secreting cells ($n_1 = 4$) are characterized from low-secreting cells ($n_2 = 17$) by a threshold of normalized fluorescence >1.20 at the end of 2 h. The highlighted lines ① and ② signify the time-dependent IL-2 secretion signals from the two identified cells in (b) and (c). ***P < 0.001 using two-tailed Student's *t*-test.

4.4. Conclusions

Smart programmable single-domain magnetoelastic materials provide an autonomous and tunable micromagnetic platform for single-cell manipulation. Coupling strain mediated multiferroic control into these platforms via voltage-induced strain enables high-throughput single-cell separation and enrichment of specific magnetically labeled cells across an electronically addressable array. Therefore, multiferroics present an opportunity to automate single-cell selection based on functional and time-dependent properties, which remains a fundamental challenge for biotechnology and the development of optimal cell therapies.[53] Furthermore, such array-addressable control of magnetic components could be used in practical applications such as magnetoelectric storage devices,[54] magnetic sensors,[55] and voltage-tunable RF/microwave devices.[56,57]

4.5 References

1. P. Tseng, J. W. Judy, D. Di Carlo, *Nat. Methods* 2012, 9, 1113.
2. B. Lim, V. Reddy, X. Hu, K. Kim, M. Jadhav, R. Abedini-Nassab, Y.-W. Noh, Y. T. Lim, B. B. Yellen, C. Kim, *Nat. Commun.* 2014, 5, 3846.
3. G. Vieira, T. Henighan, A. Chen, A. J. Hauser, F. Y. Yang, J. J. Chalmers, R. Sooryakumar, *Phys. Rev. Lett.* 2009, 103, 128101.
4. N. A. Spaldin, M. Fiebig, *Science* 2005.
5. W. Eerenstein, N. D. Mathur, J. F. Scott, *Nature* 2006, 442, 759.
6. R. Ramesh, N. A. Spaldin, *Nat. Mater.* 2007, 6, 21.
7. M. Fiebig, T. Lottermoser, D. Meier, M. Trassin, *Nature Reviews Materials* 2016, 1, 16046.
8. N. A. Spaldin, R. Ramesh, *Nat. Mater.* 2019, 18, 203.
9. J.-M. Hu, L.-Q. Chen, C.-W. Nan, *Adv. Mater.* 2016, 28, 15.
10. S. Miltenyi, W. Müller, W. Weichel, A. Radbruch, *Cytometry* 1990, 11, 231.
11. C. Batich, Annals of Biomedical Engineering 1998, 26, 904.
12. R. S. Molday, S. P. Yen, A. Rembaum, *Nature* 1977, 268, 437.
13. H. Talasaz, A. A. Powell, D. E. Huber, J. G. Berbee, K.-H. Roh, W. Yu, W. Xiao, M. M. Davis, R. F. Pease, M. N. Mindrinos, S. S. Jeffrey, R. W. Davis, *Proc. Natl. Acad. Sci. U. S. A.* 2009, 106, 3970.
14. M. A. Fischbach, J. A. Bluestone, W. A. Lim, *Sci. Transl. Med*. 2013, 5, 179ps7.
15. F. Berthiaume, T. J. Maguire, M. L. Yarmush, *Annu. Rev. Chem. Biomol. Eng.* 2011, 2, 403.
16. S. Rafiq, C. S. Hackett, R. J. Brentjens, *Nat. Rev. Clin. Oncol.* 2020, 17, 147.

17. Aijaz, M. Li, D. Smith, D. Khong, C. LeBlon, O. S. Fenton, R. M. Olabisi, S. Libutti, J. Tischfield, M. V. Maus, R. Deans, R. N. Barcia, D. G. Anderson, J. Ritz, R. Preti, B. Parekkadan, *Nat Biomed Eng* 2018, 2, 362.
18. Z. L. Chang, P. A. Silver, Y. Y. Chen, *J. Transl. Med.* 2015, 13, 161.
19. T. R. Mosmann, R. L. Coffman, *Adv. Immunol.* 1989, 46, 111.
20. M. Hölzel, A. Bovier, T. Tüting, *Nat. Rev. Cancer* 2013, 13, 365.
21. G. G. Nair, E. S. Tzanakakis, M. Hebrok, *Nat. Rev. Endocrinol.* 2020, 16, 506.
22. E. R. Jerison, S. R. Quake, *Elife* 2020, 9, DOI 10.7554/eLife.53933.
23. D. Fesnak, C. H. June, B. L. Levine, *Nat. Rev. Cance*r 2016, 16, 566.
24. N. M. Mount, S. J. Ward, P. Kefalas, J. Hyllner, Philos. *Trans. R. Soc. Lond. B Biol. Sci.* 2015, 370, 20150017.
25. B. D. Cullity, C. D. Graham, *Introduction to Magnetic Materials,* John Wiley & Sons, 2011.
26. M. Poudineh, P. M. Aldridge, S. Ahmed, B. J. Green, L. Kermanshah, V. Nguyen, C. Tu, R. M. Mohamadi, R. K. Nam, A. Hansen, S. S. Sridhar, A. Finelli, N. E. Fleshner, A. M. Joshua, E. H. Sargent, S. O. Kelley, *Nat. Nanotechnol.* 2017, 12, 274.
27. P. Chen, Y.-Y. Huang, K. Hoshino, J. X. J. Zhang, *Sci. Rep.* 2015, 5, 8745.
28. M. Buzzi, R. V. Chopdekar, J. L. Hockel, A. Bur, T. Wu, N. Pilet, P. Warnicke, G. P. Carman, L. J. Heyderman, F. Nolting, *Phys. Rev. Lett*. 2013, 111, 027204.
29. Y.-H. Chu, L. W. Martin, M. B. Holcomb, M. Gajek, S.-J. Han, Q. He, N. Balke, C.-H. Yang, D. Lee, W. Hu, Q. Zhan, P.-L. Yang, A. Fraile-Rodríguez, A. Scholl, S. X. Wang, R. Ramesh, *Nat. Mater.* 2008, 7, 478.

30. S. Manipatruni, D. E. Nikonov, C.-C. Lin, B. Prasad, Y.-L. Huang, A. R. Damodaran, Z. Chen, R. Ramesh, I. A. Young, *Sci Adv* 2018, 4, eaat4229.

31. A. Ney, C. Pampuch, R. Koch, K. H. Ploog, *Nature* 2003, 425, 485.

32. Z. Luo, A. Hrabec, T. P. Dao, G. Sala, S. Finizio, J. Feng, S. Mayr, J. Raabe, P. Gambardella, L. J. Heyderman, *Nature* 2020, 579, 214.

33. A. K. Biswas, S. Bandyopadhyay, J. Atulasimha, *Applied Physics Letters* 2014, 105, 072408.

34. M. Bibes, A. Barthélémy, *Nat. Mater.* 2008, 7, 425.

35. S. Manipatruni, D. E. Nikonov, C.-C. Lin, T. A. Gosavi, H. Liu, B. Prasad, Y.-L. Huang, E. Bonturim, R. Ramesh, I. A. Young, *Nature* 2018, 565, 35.

36. C. Israel, N. D. Mathur, J. F. Scott, *Nat. Mater.* 2008, 7, 93.

37. J. F. Scott, J. Mater. *Chem*. 2012, 22, 4567.

38. G. Youssef, S. Newacheck, M. Lopez, *Appl. Phys. Lett*. 2017, 110, 192408.

39. C.-W. Nan, M. I. Bichurin, S. Dong, D. Viehland, G. Srinivasan, *J. Appl. Phys.* 2008, 103, 031101.

40. M. B. Moffett, A. E. Clark, M. Wun-Fogle, J. Linberg, J. P. Teter, E. A. McLaughlin, J. Acoust. *Soc. Am.* 1991, 89, 1448.

41. A. Hubert, R. Schäfer, *Magnetic Domains: The Analysis of Magnetic Microstructures*, Springer Science & Business Media, 2008.

42. W. Gong, H. Li, Z. Zhao, J. Chen, *J. Appl. Phys*. 1991, 69, 5119.

43. Y. Wang, J. Hu, Y. Lin, C.-W. Nan, *NPG Asia Materials* 2010, 2, 61.

44. P. Fischer, G. Denbeaux, T. Ono, T. Okuno, T. Eimüller, D. Goll, G. Schütz, J. Phys. D *Appl. Phys.* 2002, 35, 2391.

45. T. A. Duenas, G. P. Carman, *J. Appl. Phys.* 2000, 87, 4696.

46. K. P. Mohanchandra, S. V. Prikhodko, K. P. Wetzlar, W. Y. Sun, P. Nordeen, G. P. Carman, *AIP Adv.* 2015, 5, 097119.

47. J. Ye, R. T. Merrill, J. Geophys. *Res.* 1995, 100, 9995.

48. J. Happel, H. Brenner, Low Reynolds Number Hydrodynamics: With Special Applications to Particulate Media, Springer Science & Business Media, 2012.

49. J. Leach, H. Mushfique, S. Keen, R. Di Leonardo, G. Ruocco, J. M. Cooper, M. J. Padgett, Phys. Rev. E Stat. Nonlin. *Soft Matter Phys*. 2009, 79, 026301.

50. N. Nitta, T. Sugimura, A. Isozaki, H. Mikami, K. Hiraki, S. Sakuma, T. Iino, F. Arai, T. Endo, Y. Fujiwaki, H. Fukuzawa, M. Hase, T. Hayakawa, K. Hiramatsu, Y. Hoshino, M. Inaba, T. Ito, H. Karakawa, Y. Kasai, K. Koizumi, S. Lee, C. Lei, M. Li, T. Maeno, S. Matsusaka, D. Murakami, A. Nakagawa, Y. Oguchi, M. Oikawa, T. Ota, K. Shiba, H. Shintaku, Y. Shirasaki, K. Suga, Y. Suzuki, N. Suzuki, Y. Tanaka, H. Tezuka, C. Toyokawa, Y. Yalikun, M. Yamada, M. Yamagishi, T. Yamano, A. Yasumoto, Y. Yatomi, M. Yazawa, D. Di Carlo, Y. Hosokawa, S. Uemura, Y. Ozeki, K. Goda, *Cell* 2018, 175, 266.

51. M. Etier, V. V. Shvartsman, S. Salamon, Y. Gao, H. Wende, D. C. Lupascu, *Journal of the American Ceramic Society* 2016, 99, 3623.

52. J. Ma, J. Hu, Z. Li, C.-W. Nan, *Adv. Mater*. 2011, 23, 1062.

53. S. R. Burns, O. Paull, J. Juraszek, V. Nagarajan, D. Sando, *Advanced Materials* 2020, 32, 2003711.

54. G. Sreenivasulu, P. Qu, V. Petrov, H. Qu, G. Srinivasan, *Sensors* 2016.

55. Z. Yao, Y. E. Wang, S. Keller, *IEEE Transactions* on 2015.

56. W. Peng, B. Howe, X. Yang, *Integrated Multiferroic* 2019.

57. S. Ross, D Cantrell, *Annual Review of Immunology* 2018, 36, 411.

Chapter 5 . Concluding Remarks

This work explores microfluidic solutions to improving sample processing procedures, especially by means of process automation; and enhancing the sensitivity metrics of assay performances, targeting the analysis of single entities. The first two chapters covers the development of digitalized affinity assays for single molecule detection, where we achieved counting of single enzyme reactions using a novel lab-on-a-particle assay mechanism. We demonstrated digital counting of β-galactosidase enzyme at a femtomolar detection limit with a dynamic range of 3 orders of magnitude using standard benchtop equipment and experiment techniques. The third chapter presents an innovative ferrobot platform to address process automation for sample processing. This electromagnetic platform is capable of performing massively parallelized and sequential fluidic operations cross-collaboratively to complete pipelined bioassays with high efficiency and flexibility. In the fourth and final chapter we established a multiferroic system deployed for time-lapse single-cell functional profiling, featuring both single entity analysis capacity and an automation potential.

-

Digital ELISA allow measurement of biomarkers down to individual molecules, leveraging sub-nanoliter compartmentalization and signal amplification. However, these technologies require tailored and often expensive microwell devices or microfluidic droplet generators for compartmentalization, and custom optical analysis systems to characterize low levels of fluorescence. The need for specialized and relatively costly equipment (e.g. Quanterix Simoa

system) has impeded the adoption of digital ELISA technologies for biomarker discovery or clinical diagnosis.

Discussions on the utility of digital ELISA often encounters a “chicken and egg” dilemma. For a new and high-sensitivity technology such as digital ELISA to be widely adopted and acknowledged in clinical research and practice, the clinical value of the low-abundance biomarkers to be measure to digital ELISA needs to be established. However, studies of low-abundance biomarkers have not been established precisely due to the lack of reliable measurement methods. The best way out of this dilemma is for digital ELISA to be widely adopted, so that the clinical value of the low-abundance biomarker can be studied and discussed by the general research community.

We envision the hydrogel microparticles we described in our work can be fabricated at a central site and widely distributed to speed the adoption of highly sensitive immunoassays. The entire workflow upon receiving the pre-made particles will be performed using basic mixing operations and standard benchtop laboratory equipment without microfluidic chips or pumps, and the results of reactions can be analyzed with widely available flow cytometers or sorters at high throughput. This platform has great potential for democratizing ultra-sensitive immunoassays, advancing the discovery of extremely rare biomarkers, as well as redefining disease diagnosis.

-

The ferrobot platform was a bottom-up engineering design that overcame two fundamental limitations in digital microfluidics, dominated by EWOD techniques. EWOD approaches require

complex device fabrication, high excitation voltage (~20-200 V), and can suffer from electrode contamination and limited durability, which altogether restrict EWOD from achieving the envisioned applications. Alternative methods such as magnetic droplet actuation techniques were either not scalable, or inherently rendering too weak of an actuation forces to control meaningful bio-packages.

Although we were successful in designing various liquid handling components to achieve complicated manipulations including liquid transport dispensing, merging, droplet generation, filtration, and was able to program a team of ferrobot to collaboratively perform a pipelined in-situ calibrated MMP measurement assay, the scope of this work was limited to a proof-of-concept MMP measurement from spiked human plasma samples and a small portion of high-reading patients body fluid samples. The full potential of the ferrobot platform awaits continuous development to address several physical and biochemical limitations that as of now restrict the platform from providing a full spectrum of clinically meaningful diagnostic readings.

-

The SMArT platform featuring single-domain multiferroic array-addressable Terfenol-D micromagnets was an exciting teaming of the frontiers in electrical, mechanical and biomedical engineering. An interesting aspect of the technology is that the magnetism of the micromagnets could self-sustain for prolonged periods of time without constant support of external magnetic field. Translating to the profiling and selectin of single cells, this means the cells can remain captured to a magnetic feature until the release was commended by applying voltage. Therefore, time-lapse properties such as secretion could be observed and measured continuously on captured

cells without consuming external energy, as opposed to many other single cell technics where the localized fixation of single cells needs continuous application of external forces to maintain.

Beyond the successful demonstration of capture and release on the SMArT platform, continuous development is needed to fulfill the entirety of the blueprints, such as the addressability of individual magnetic units and the reliable of voltage-induced particle and cell release. As with any explorative mission, the nature of a system becomes more revealed and comprehensible only after relentless interrogations and unceasing repairs. Such is the life of science.